SCUOLA DI DOTTORATO
UNIVERSITÀ DEGLI STUDI DI MILANO-BICOCCA

Department of
Materials science

PhD program Materials Science and Nanotechnology Cycle XXXII

Ga-RICH OXIDE-IN-OXIDE GLASS-CERAMICS: FROM BULK TO THIN FILM DEVICES

Surname: Remondina Name: Jacopo

Registration number: 738899

Tutor: Prof. Paleari Alberto

Co-tutor: Dott. Lorenzi Roberto

Foreign tutor: Prof. Ressel Roland

Coordinator: Prof. Bernasconi Marco

ACADEMIC YEAR 2018/2019

Abstract

In this thesis I'm presenting the work I have carried out during my PhD on Ga-oxide containing nanostructured glass-ceramic films as a potential breakthrough for the implementation of this class of material in planar geometry for applications in the field of optoelectronics. In the last three years, my investigations have been aimed at understanding the relationship between the occurrence of nanostructuring – analysed through a detailed structural studies by means of different microscopy and diffractometric techniques as a function of deposition conditions and post-deposition treatments – and the physical mechanisms of charge transport and polarization taking place in oxide-in-oxide films.

The studied material was produced by RF sputtering deposition starting from a glass target of Li, Na, Si, Ga and Ge mixed oxides. As a consequence of the deposition process we have obtained partially crystallized material with Ga-rich nanocrystals incorporated in the remaining amorphous matrix. Through atomic force microscopy, x-ray reflectivity, 2D-x-ray diffraction, 2D-small angle x-ray scattering - also employing synchrotron radiation facilities - we have fully characterized the nanostructured films at different length scales, from few nm to few microns. The detailed analysis of the results shows the formation of multiple anisotropic spinel Ga-oxide nanocrystals with size of about 3 nm, forming larger lenticular aggregates with significant differences between the in-plane and the out-of-plane dimensions. As a result of the investigation of differently treated samples, the study also shows that size distribution and morphology of the nanostructures can be controlled by deposition conditions, duration and temperature of post-deposition thermal treatments.

Starting from the knowledge of the structural features, the research activity has been directed to the deep understanding of the charge transport properties resulting from the nanostructured nature of the material, including the γ-Ga_2O_3 semiconductor nanophase and the dielectric host matrix. The electrical response – analysed with the aid of complex impedance

spectroscopy – turns out to be the results of multiple contributions to transport and charging mechanisms by the matrix and the nanophase, including the effects of the internal interfaces. The data suggest that the charge transport is sustained by a combination of thermally activated hopping and tunnelling mechanisms mediated by the percolation path built up by the nanostructured features of the material. Interestingly, the overall response gives preliminary evidences of electrical plasticity, making nanoglassceramic thin films potential candidates as key systems in advanced devices for brain-inspired oxide-in-oxide fully inorganic memories.

Contents

Chapter 1

Introduction

1.1 Applications

In the world there are different groups active in the study of the oxide-in-oxide glass-ceramics. Almost all the studied systems in literature are based on SnO_x as inner oxide [1, 2, 3] or ZnO[4]. An alternative interesting system, which I have studied during my research activity, is a material in which nanocrystals of gallium oxide, a wide band-gap semiconductor, are embedded in a germanium-silicate matrix. The interest for this class of materials comes from the promising properties of such oxide[5] that could be used in different fields of applications, such as photo-electronic devices (both as sensor or in solar cells), catalysis (especially in the water splitting for the production of hydrogen) and power devices (thanks to the very high Baliga Figure-of-Merit estimated to be over 3400, to be compared with 340 and 870 of SiC and GaN respecitvely[6]), while maintaining the processability and stability typical of glasses.

In particular, Ga-oxide containing glassceramics are promising for optical applications, and in particular as UV-solar blind detectors [7] and IR emitters [8].

For these reasons I tackled the task of obtaining and controlling Ga-oxide-in-oxide material in planar geometry, as thin films. This can really constitute a breakthrough for different applications, whose feasibility have been investigated to some extent in my present work. These applications range from flame detectors to astronomy and environmental science[9] also including catalytic devices[10]. Finally we have also considered the use of Ga-oxide-in-oxide nanostructured films as artificial synapses that could be implemented in the expanding sector of neural networks for machine/deep learning[11], in the form of resistive switching devices.

1.2 Similar works

The idea of combining oxides made by elements of different groups (i.e. IA, IIIA and IVA in my case) is very old. In fact, historical windows had different properties according to when and where they have been fabricated, and these differences actually depends on the different percentages of the different oxides present in them [12, 13]. During the XX century, researchers started to use glasses also as functional material (i.e. all the works on rare-earth doped glasses). Among adding metals or RE ions, one of the way to obtain these functional glasses was to mix structural oxides (i.e. SiO_2, GeO_2, Al_2O_3, ...) with other oxides that could give the glass itself some interesting properties. One of the first example in this direction is the 1969 work of Nakagawa and Izumitani [14] where they investigated the miscibility of the silicon and titan oxides. Studies performed on mixed glass with composition similar to mine (with elements from group IA, IIIA and IVA) were also realised starting from the middle of the past century[15]. However, despite the investigation on aluminium-silicate glasses had been quite intense (3948 documents according to scopus on December the 12th, 2019), when moving to other oxides mix, the number of corresponding documents drop significantly (71 documents for Ga_2O_3/SiO_2 oxides and 105 for Al_2O_3/GeO_2). In particular, the Ga_2O_3/GeO_2 combination (like in my case) resulted in 109 entries; however only less than half of these works involved also electric/onic properties.
On the other hand, when looking at how thin film glasses can be produced, the literature compaatible with my work is richer: many times films are obtained trough chemical routes (i.e. sol-gel, chemical vapour deposition, atomic/molecular layer depositions, ...), but also physical techniques are widely used. Of these, the two most common ones are the sputtering itself and, especially most recently, the pulsed laser deposition. When comparing the quality of the samples obtained trough the two techniques [16], it appears that the sputtering could lead to a more ordered system. When high crystallinity is not a strong requirement, as when working with glasses, PLD remains a valid alternative, especially when sputtering yield poor results.

1.3 Bulk studies

My research began from the previous knowledge of the structure, chemistry, and photo-physics of the bulk version of the investigated material maturated inside the research group. The first works, starting from the 2012, were about the synthesis of the material itself. In these, they proved trough XRD, TEM imaging (i.e. [17]),

Differential Scanning Calorimetry (DSC, i.e. [18]), Small Angle Neutron Scattering (SANS, [19]) Nuclear Magnetic Resonance (NMR, [20]) and different luminescent methods that the as prepared, fully amorphous, glass can undergo a phase change that allows the formation of crystalline nanoparticles. Moreover, these nanoparticles have been identified as gallium oxide in the γ phase, one of the most exotic (the stable one is the β; the α is also quite stable and studied, while the γ, δ and ε are so highly metastable at normal conditions that it is hard to find any information other than the crystal parameters). Previous investigations also regarded the effects that doping (i.e. [21, 22]) and TT conditions (i.e. [23]) can have on the NPs density and size.
Once the basics of the material were known, other studies were aimed at investigating possible applications using laser selective treatments[8], for the design of optical devices. The research presented in this thesis started from the finding that these glass-ceramics show a response to UV-C photons resulting in blue light emission[7].
In this work, I investigated the local charge effects in a small dimensional geometry, with special regards to the transportation and recombination mechanisms. To do so, thin films were prepared through RF-sputtering deposition. These films were then structural analysed using many techniques investigating many aspects (surface morphology, composition, cristallinity, homogeneity). Finally, these films were incorporated into Metal-Oxide-Semiconductor devices to be electrically characterized using complex impedance spectroscopy interpreted with different models.

Chapter 2

Film preparation

Investigation made in collaboration with **Prof. M. Acciarri** group.

2.0 Bulk preparation

Investigation made in collaboration with **Prof. V. Sigaev** group from **D. Mendeleev University of Chemical Technology of Russia, Dept. of Chemical Technology of Glass and Glassceramics**.

We prepared our films trough a Physical Vapour Deposition (PVD) method starting from a custom-made bulk sample (target). The target has been prepared by Prof. V. Sigaev and his group at D. Mendeleev University of Chemical Technology of Russia, Dept. of Chemical Technology of Glass and Glassceramics.
This sample has been prepared through the melt-quenching method. For this, the first step is to weight Si, Ge and Ga oxides and Li and Na carbonates so to achieve a final composition (oxide molar %) of $7.5Li_2O$-$2.5Na_2O$-$20Ga_2O_3$-$45SiO_2$-$25GeO_2$.
The starting materials have been pulverized and mixed together in an agate mortar and transferred in a Pt crucible to be heated at 1480°C for 40 minutes in air atmosphere. Once the melt was ready, it was poured onto a stainless steel plate and quenched by pressing another stainless steel plate on it. The sputtering instrument involved in this work use targets of 2.5x0.5 inches (diameter x thickness, 63.5x12.7 mm) so a final sample with this geometry was prepared. The target was used as-quenched, so to be glassy (fully amorphous).

2.1 Sputtering apparatus and deposition conditions

The instrument I used is an home made one and it's main components are:

- a rotative pump
- a turbo molecular pump
- different pressure sensors
- a mass flow glass controller with 4 separate channels (Ar and O lines connected)
- a steel deposition chamber pneumatically operated
- open circuit, water coolers for both the turbomolecular pump and the target holders
- RF generator
- a separate RF matching network

To achieve the best possible growth yield, different parameters including the operating pressure, the carried gas used, the voltages involved (for both the RF and the DC fields), the substrate-target distance and the temperature of the substrate must be optimized for each sputtering material and system. In my case, we obtain an acceptable yield (around 2.2 nm/min) using around $6 \cdot 10^{-3}$ mbar as working pressure and an RF field at 250W that give rise to a DC field of about 1.1 keV. In our system, the target-substrate distance is fixed (roughly 10 cm) and the expected temperature of the substrate is of the order of 70-80°C.
A typical deposition procedure is as follow:

1. on the day preceding the deposition, the substrates have been cleaned with proper reagents/solvents depending on the nature of the substrate itself (for example, for bare silicon, the cleaning are performed in acetone and then in HF);
2. after been dried out with laboratory paper, the substrates are transferred in the deposition chamber and secured with polyimide tape to the substrates support. Up to 4 samples can be prepared with the same sputtering time and up to 2 different sets of substrate to be sputtered for a different amount of time can be present in the chamber at the same time;
3. the chamber is then evacuated to low vacuum (around a mbar) for the night using a rotative pump. The pump is then turned off;

4. on the following day, the rotative pump is turned on again for about 15 minutes, after which also the turbomolecular pump is turned on. The system remain in this status for a couple of hour, so that the vacuum can reach an high level (about 5E-5 mbar);

5. the plasma is then started by:

    - properly setting the valves that control the input of the carrier gas and the output (to the pumps) so that the chamber has the desired pressure;
    - slowly turning on the RF antenna while checking the light emission of the plasma and the measured bias value (both are feedback about the effective presence of the plasma inside the chamber);

6. the plasma is stabilized for about 10 minutes;

7. after that time, the selected substrates are placed under the target and the deposition can start;

8. after the desired amount of time (max 60 minutes for safety reason), the substrates can be moved out of the deposition area and the plasma turned off (by first turning off the RF antenna and then, rapidly, closing the gas valve);

9. if other depositions are planned, a cool down period not shorter than 15 minutes must be taken;

10. when all the planned depositions are done, the turbomolecular pump is turned off. It's water cooling circuit however remain on till the opening of the chamber;

11. after such pump completely stop rotating, usually about 15 minutes, the water circuit is closed, the chamber is vented with nitrogen and opened for sample removal/substitution.

The previous procedure gives an yield that can be considered constant through a quite large time windows, starting from 1 minute up to 1 hour, as it can be seen in Figure 2.1. For deposition longer then 60 minutes (about more than 150nm of thickness), multiple cycles must be performed, and this leads to some issue (see section 2.3).

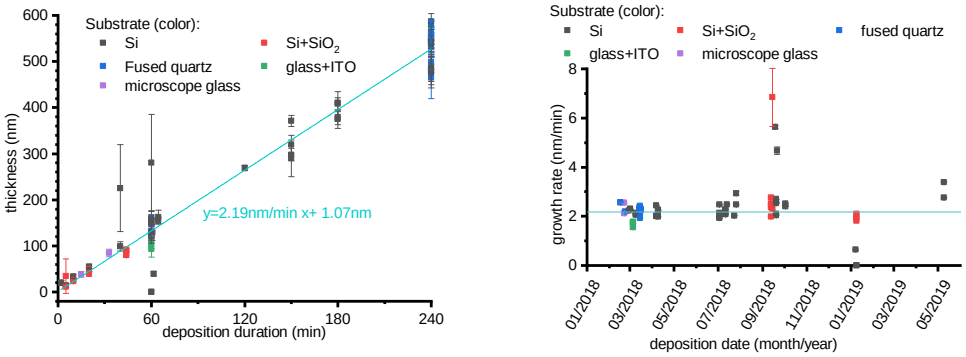

(a) (b)

Figure 2.1: (a) sample thickness versus the duration of deposition. (b) growth yield versus the date of the deposition; till October 2018 the yield remained constant.

2.2 Thermal treatment

One of the most important feature of the bulks was their ability to form crystalline nanoparticles when Thermally Treated (TT) at the correct temperature [20], so some of the films underwent the same process (the other, called As Deposited (AD), have been used as control/reference). Normally this Thermal Treatment (TT) has been carried out in air inside a muffle with temperature feedback by introducing the film(s) when the temperature inside was already stabilized around the set point (usually 700°C) and removed after 30 minutes. There is a noticeable exception to this procedure: for practical reason, the samples studied in Figure 3.27, has been TT using an Anton Par DHS 1100 ([24]) with fluxed nitrogen.

2.3 Film quality

In general, AD film homogeneity is quite high. Unfortunately, the TT worsen the quality, especially when temperatures higher than 650°C are used on film deposited with multiple cycles (see Figure 2.2 for some examples), resulting in very rough films. The origin of this roughness has been found to be related to the formation of bubbles (Figure 5.13) which probably originated from the evolution during the TT of gaseous species from the lithium atoms that are part of the films.

This effect, together with the impossibility to perform deposition longer than 60 minutes, prevented us to obtain homogeneous TT films thicker then 130 nm, well below the minimum for many optical measurements, including Raman spectroscopy and refractive index estimation, preventing a comparison with the bulk. For this reason, attempts has been taken in place to overcome this issue.

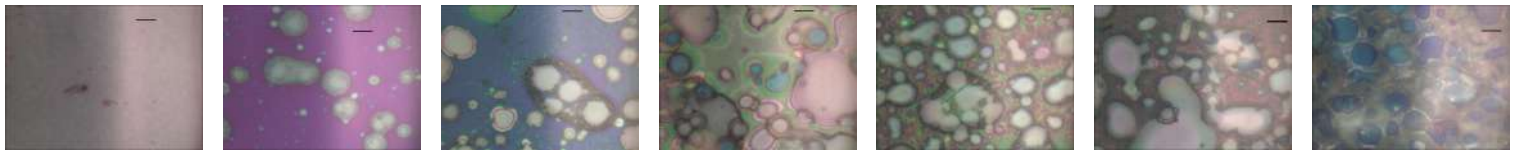

(a) AD (b) 600 (c) 620 (d) 640 (e) 660 (f) 680 (g) 700

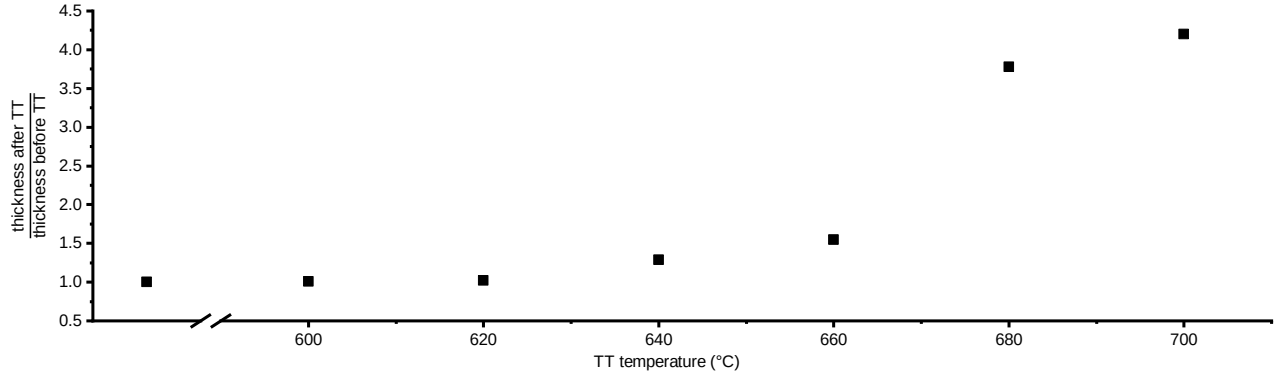

(h)

Figure 2.2: Top line: images taken with optical microscope of samples TT at different temperatures (expressed as °C) for 30 minutes (scale bar: 5µm). (h) The thickness ratio measured on the same samples before and after they were TT.

First, we tried by performing annealing after the full run. Then we performed pre-treatment annealing at temperatures in the range 200-600°C. Higher temperatures yield quite better results in terms of swelling, but these samples still present an increase in the thickness when TT at 700°C. We also try a mild annealing at 200°C in vacuum for a night, but with the same results.
Finally, the best results were obtained by alternating each deposition run (up to 1 hour) with a night in the oven at 600°C. In this way the optical quality of the sample remains very high. The drawbacks of this solution however are two: the effective deposition yield drop drastically (from about 130nm per hour to the same thickness per day) and also the "AD" sample is at least partially annealed.

Chapter 3

X-Ray characterization

Investigation made in collaboration with **Prof. R. Resel** group from **Technische Universität Graz**.

3.1 XRD

3.1.1 XRD theory

X-Ray Diffraction (XRD) is a technique discovered in the 1910s years and that consist in the determination of the crystal structure of a substance by illuminating it with an x-ray monochromated light.
Due to their charge, electron clouds of atoms can diffract an incident photon all around them, so a single atom would lead to some halo without any useful information. Things start to become more interesting when adding other diffracting atoms equally spaced each other: the halos of each center combine with the others resulting in a interference patterns with constructive and destructive area. The intensity of this effect is proportional to the number of the diffracting centres squared.
The effect is mainly limited to crystals[1] since in them the atoms are ordered according to some periodicity along three independent directions ($\overrightarrow{a_1}$, $\overrightarrow{a_2}$ and $\overrightarrow{a_3}$). The volume defined by such three directions is called repeating unit. At this repeating unit correspond an equivalent unit cell in the reciprocal space defined by the three vectors:

$$\overrightarrow{b}_i = \frac{\overrightarrow{a}_j \times \overrightarrow{a}_k}{\overrightarrow{a}_i \cdot (\overrightarrow{a}_j \times \overrightarrow{a}_k)} \tag{3.1}$$

[1]Actually, there are some studies also on amorphous materials like [25, fig. 7-8]. However, on them, the obtainable informations are limited to the mean distances between adjacent atoms, and usually only to first or second neighbourhoods due to the rapidly decreasing signal to noise ratio for this kind of measurements.

with i, j and k indexes indicating an ordered permutation of 1, 2 and 3, $\overrightarrow{b}$ being an axis in the reciprocal space and $\overrightarrow{a}$ the corresponding axis in real space.
Since during diffraction we are dealing with elastic scattering, we can use von Laue equation:

$$\overrightarrow{d} \cdot \Delta\overrightarrow{K} = 2\pi m \rightarrow e^{\imath \overrightarrow{d} \cdot \Delta\overrightarrow{K}} = 1 \tag{3.2}$$

with $\overrightarrow{d}$ representing the vector between two diffracting unit cells (real space) and $\Delta\overrightarrow{K} = \overrightarrow{G}_{hkl} = \overrightarrow{K}_d - \overrightarrow{K}_i$ being the difference between the incident and the diffracted beam. The main consequence of this equation is the fact that we can measure only distances between planes perpendicular to the bisector of the angle defined by the incident and the diffracted beam.
A second consequence is the Ewald sphere construction [26], a sphere in the reciprocal space with radius:

$$R_{Ewald} = |\overrightarrow{K}_i| = |\overrightarrow{K}_d| = \frac{2\pi}{\lambda_{X-ray}} \tag{3.3}$$

It is constructed by positioning the sphere with its surface on a unit cell origin and extending it in the direction opposite to the incident beam. The unit cells that participate in the diffraction must have their origins on this sphere surface.
To find the position of such peaks in real space one can instead use the Bragg law[27]:

$$2d\sin(\theta) = n\lambda \tag{3.4}$$

stating that the main peak corresponding to planes away from each other of a length d (real space), when measured with a light with wavelength λ should produce peaks in a direction from the horizon of θ. Additional peaks appear at the corresponding harmonics of λ.
Finally, to estimate the intensity and the width of the peak, the multiple slit interference function could be used:

$$I = I_0 \left[\frac{\sin\left(\frac{1}{2}N\theta\right)}{\sin\left(\frac{1}{2}\theta\right)} \right]^2 \Rightarrow \lim_{\theta \to 0} I = N^2 \tag{3.5}$$

With I being the diffracted intensity, I_0 the incident beam intensity, N the number of diffracting centres (usually tens or hundreds of thousands) and θ a direction compatible with Equation 3.4.
The samples analysed in this work are expected to have crystals oriented with completely random directions. This condition is not so out-of ordinary: it is very similar to the one called "powder diffraction" in which the sample is pulverized in lots of small crystals and that, hypothetically, each of them should have an orientation slightly

different from all the others and that together they should cover the whole possible orientations. This procedure is very often used, especially when single crystals with a well defined orientation cannot be produced and for this reason all the treatments behind it are standardized.
In this view, the Bragg formula Equation 3.4 remain valid, but with some extension/-modification: when the sample orientation can cover the whole possible orientation in a 3D space, the orientation of the sample itself doesn't play a major role, allowing to measure all the inter-planar distances with a single 2θ scan keeping the incident angle fixed. This type of measure is called "powder diffractogram" and there are many available tools that can calculate such result starting from crystal informations.
When acquiring diffraction data usually a specular scan is used. When doing so, the incident beam and the measured one are tilted from the sample surface by the same angle θ; in this way only planes with a specific orientation are probed (Equation 3.2), and in particular they must be parallel to the film surface. There exist two set-up configuration to obtain these data: the θ-θ (both the x-ray tube and the detector move of an angle θ each step, so that they look symmetrically the sample) and the θ-2θ (where the tube is fixed, the sample rotate at a speed and the detector at twice such speed, so that, again, the tube and the detector look symmetrically the sample). In my case however, all the directions are equal, so I preferred to optimize the irradiated area. To do so, I set the difractometer (the instrument that is used for acquiring XRD data) to operate in a not so common configuration: I fixed the x-ray tube and the sample position, so that the incident beam always illuminate completely the second, and set the detector to move for the 2θ range selected. In this way, every point of the scan was probing a different direction in the reciprocal space (and not just a different distance), but all of them are probing always the whole film.
Finally, I can introduce the Scherrer law [28], which is used to determine the crystal domains size:

$$s = \frac{K\,\lambda}{\Delta(2\theta)\,\cos(\theta)} \tag{3.6}$$

with s representing the crystal domain size, K is a (dimensionless) shape factor close to unity, λ is the used x-ray wavelength, $\Delta(2\theta)$ is the integral peak width[2] and θ is half 2θ (the sum of the angles between the incident beam and the sample and the

[2]Actually, to be accurate, one should deconvolve the measured FWHM in the instrumental and the sample parts, but for this work I considered the $\mathrm{FHWM}_{\mathrm{sample}} \gg \mathrm{FHWM}_{\mathrm{instrument}}$, so that $\mathrm{FHWM}_{\mathrm{measured}} \approx \mathrm{FHWM}_{\mathrm{sample}}$. Additionally I also considered the broadening from the strain as negligible.

diffracted beam and the sample).

3.1.2 XRD/XRR apparatus

The laboratory instrument used is a Panalytical Empyrean diffractometer [29] equipped with a Cu X-ray emitting tube. The detector used is a PIXCel3D [30] used in 0D mode for XRR measurement (central 3 lines enabled) or in 1D mode for XRD. A picture of this machine is presented in Figure 3.1a.

(a)

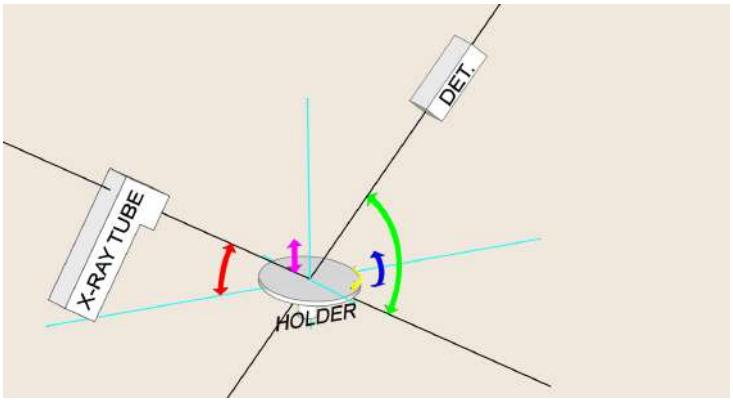

(b)

Figure 3.1: Top: a picture of the laboratory XRD/XRR instrument, a Panalytical Empyrean. Bottom: schematic of the available axis: red=ω (incident angle), green=2θ (diffracted angle), blu=χ (sample tilt), yellow=φ (sample direction) and magenta=Z (sample height); as reference, in cyan there are the 3 orthogonal axis and in black the beams.

The goniometer has 4 circles and the Z axis remotely controlled (see scheme in

Figure 3.1b). In the incident beam path, between the tube and the sample, there are, in order:

divergence slit used to limit the divergent angle of the incident beam;

mask used to limit the lateral width of the beam;

parabolic mirror/monochromator to transform the divergent beam into a pseudo-parallel one and to partially cut out unwanted wavelengths;

attenuator with a reducing factor of approximately 127x and software controlled, used to avoid direct (or too intense) exposure of the detector.

While on the diffracted beam there is an anti-scatter slit (used to avoid collecting radiation that come outside the illuminated sample).
The set-up commonly used involve a divergence slit with a fixed incidence of 1/8° that correspond to about 0.3 mm after the parabolic mirror, a mask of 1 cm and the attenuator disabled except when performing XRR measurement with high intensity (many kcps) and an anti scatter slit with an aperture of 8 mm for XRD or 0.1 mm for XRR.
XRD measurements have been performed doing a 2θ-scan with a fixed ω calculated to have the incident beam completely illuminating the sample, while XRR have been performed in specular mode (ω=θ).
In order to optimize the signal and minimizing systematic errors (i.e. shifts in peaks positions), the goniometer must be correctly aligned every time the sample is changed or moved. The alignment procedure consist in:

1. **2θ-scan** with the stage moved down, so that the detector can be aligned to completely see the direct beam at 0° (this step must be performed only once in a while, i.e. at system warm up);

2. **Z-scan** to adjust the stage height so that the direct beam is half covered by the sample itself;

3. **direct ω-scan** performed by measuring a maxima while looking at the primary beam, so to have the sample surface parallel to the direct beam;

4. **reflected ω-scan** performed by achieving a maxima in the reflected beam (this method allow a finer tuning then the point 3);

5. **χ-scan** so to optimize also the perpendicular direction (this alignment step is also performed by measuring the reflected beam).

Since the second and the third step depend on each other, they must be repeated by alternating them till a scan confirms the optimal position. It has been found that the films here presented are too rough to be influenced from a χ optimization, so this step has been skipped most of the times.

3.1.3 Grazing Incidence-XRD

Grazing Incidence XRD (GIXRD) consist in an XRD experiment performed using very small ω and with data collected as a 2D image instead of a simple 1D line. Using this configuration one can probe surface layers, so it's used for thin films, and access also crystallographic direction not completely out-of-plane (Figure 3.2a).

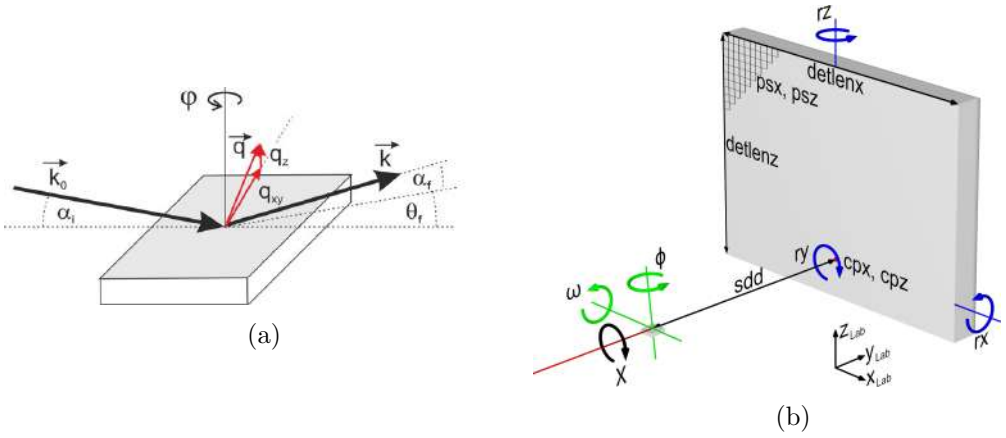

Figure 3.2: (a) a schematic representation of what happen during a GIXRD experiment. Figure 3.2b a schematization of the experimental set-up in use at the XRD1 Elettra beamline. Courtesy of Benedikt Schrode.

To collect such images one can use either a 0D detector that moves on two orthogonal axes, a 1D detector (movement on one axis) or a 2D detector.
Measurements were performed at the beamline XRD1, Elettra Synchrotron in Trieste (IT). This beamline mounts a 2D detector along a rail oriented as the primary beam, so that the geometry resembles the one in Figure 3.2b.
The primary beam is generated by extraction from the storage ring operating at 2.0 GeV. Before arriving to the experimental hutch, the beam is "prepared" for the experiment by some optics and slits, which selects the wavelength (usually 1.54 $\dot{A}^{-1}$, with an energy resolution of about 10^{-4}), to reduce the divergence and to shape the beam so to obtain a square of 0.2 x 0.2 mm.

The sample stage used for film samples use a rotative pump connected via a rubber tube to keep the sample in position during the experiment. The stage regulations is a combination of manual and software controls. For checking that the sample surface is perpendicular to the χaxes (Figure 3.2b), a laser is used, and the sample alignment is performed manually adjusting two orthogonal circles (which can be described by the angles ω and χ in picture Figure 3.1). This is necessary to avoid the vobling of the sample during the φ rotation.
Z alignment is performed via software instead: different very fast pictures are collected without using the beam stopper (some attenuators are instead used to reduce the overall radiation) with the stage positioned at sligltly different heights. The collected images usually appear as completely black except for few pixels where the primary beam hit the detector. While the sample is in between the primary beam, also these few pixels appear as dark. As the correct z position, one should use the middle position between the point where the integrated intensity over such pixels start to fall and where it reach a plateau.
The detector used is a Dectris Pilatus 2M [31], a 2D detector with a sensing area of about 253.7×288.8 mm^2 divided into $1475 \times 1679 = 2,476,525$ pixel. The degree of freedom of the set-up used were (see Figure 3.2b for a scheme):

ω: the incident beam angle (on the opposite of the lab-scale equipment, in this case the regulation is on the sample itself for obvious reason);

Sample-Detector Distance (SDD): this distance influence both the resolution of the acquired imagine and the sampled diffracted angles; in this work we set a SDD of 150mm (first beam time) or 200mm (second beam time), so to have data up to a Cu-K_α equivalent of about 60/40°;

detector X and Z: the detector position in the directions perpendicular to the primary beam could be slightly modified (best would be to have the primary beam hit the detector near a corner, so to optimize the acquisition to a single quadrant of the reciprocal space);

φ: the sample direction can be changed for two reasons: probing different directions [32] or hide some features from the substrate, preventing an optimal exposure;

exposure time: it's important to have an exposure time as long as possible (better intensity and signal to noise ratio) without saturating the detector (about 1M of counts); this was set from 1 s up to few minutes, depending on the results and according to the previous criteria.

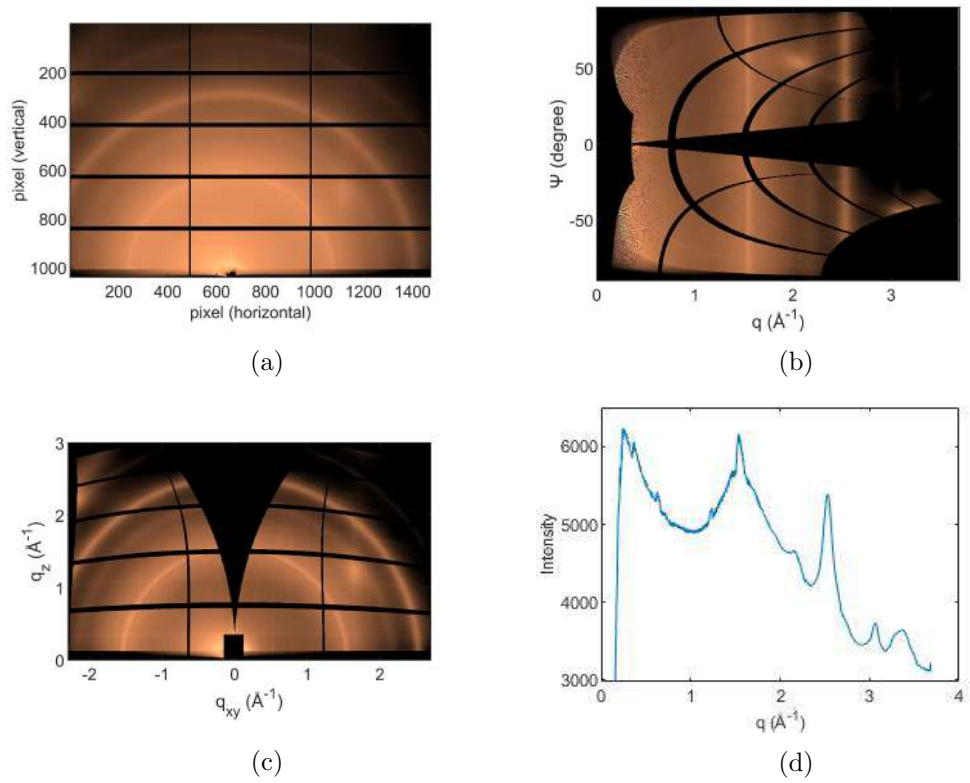

Figure 3.3: Some of the possible ways to represent GIXRD data: Figure 3.3a real (laboratory) space representation, Figure 3.3b polar coordinates, Figure 3.3c q (sample) space and Figure 3.3d line scans (polar space integration). All this representation refer to the same measurement (collected at ω=1.5°), performed on a sample growth for 60 minutes and TT for 30 minutes at 700°.

The result of a GIXRD experiment is basically an image such as the one in Figure 3.3a. A reference measurement is used to precisely get the experimental conditions by measuring a standard and fitting the measured data to the known ones. Data were elaborated using GIDVis[33].

As first step, a reference measurement is used to precisely get the experimental conditions by measuring a standard and fitting the measured data to the known ones. Once the original figure has been converted in reciprocal coordinates (q_z vs. q_{xy}) as in Figure 3.3c some qualitative analysis can already be made, such as the comparison with the expected peaks or measuring the position of the present ones (eventually as part of a ring, symptom of poor plane orientation).

Finally, we obtained a powder-like diffractograph (like in Figure 3.3d) from the acquired image, by converting it to polar coordinates (Figure 3.3b) and then integrating over the whole arc for each given |q|. A comparison between the results taken with the laboratory equipment and at the synchrotron is given in Figure 3.4.

The collection of data at different incident angle leads to slightly different results, as

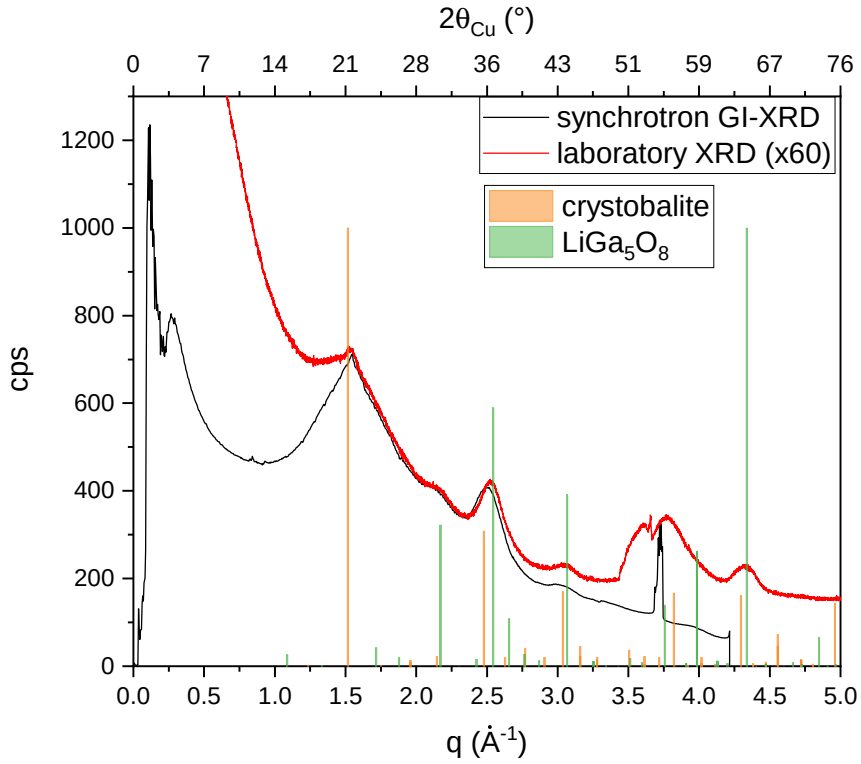

Figure 3.4: Comparison of the diffraction pattern collected with in-house instrument and at the synchrotron. The two pattern are comparable after a proper rescaling. Sample: growth for 60 minutes and TT for 30 minutes at 700°.

reported in Figure 3.5. The most evident difference is the fact that, when measuring at very small angles (0.2°), when the only film should be probed, the informations (rings) are almost completely lost (due to the fact that the primary beam is mainly reflected on the surface instead of entering the film), so data were collected at a slight higher angle, ω=0.5° (Figure 3.5b).

3.1.4 Film thickness results

3.1.4.1 In-house experiments

To investigate the effect of the thickness on XRD diffractograms, 7 couples of films have been prepared with estimated thickness ranging from 1 to 130 nm. For films with thickness less than 50 nm, a Si substrate with a layer (150nm) of SiO_2 was used, while for thicker films, a normal Si substrate was used. For every thickness 2 films were prepared, and one of them was TT at 700°C for 30 minutes. To have an acceptable signal-to-noise ratio, an hight time per step (about 40 minutes, resulting

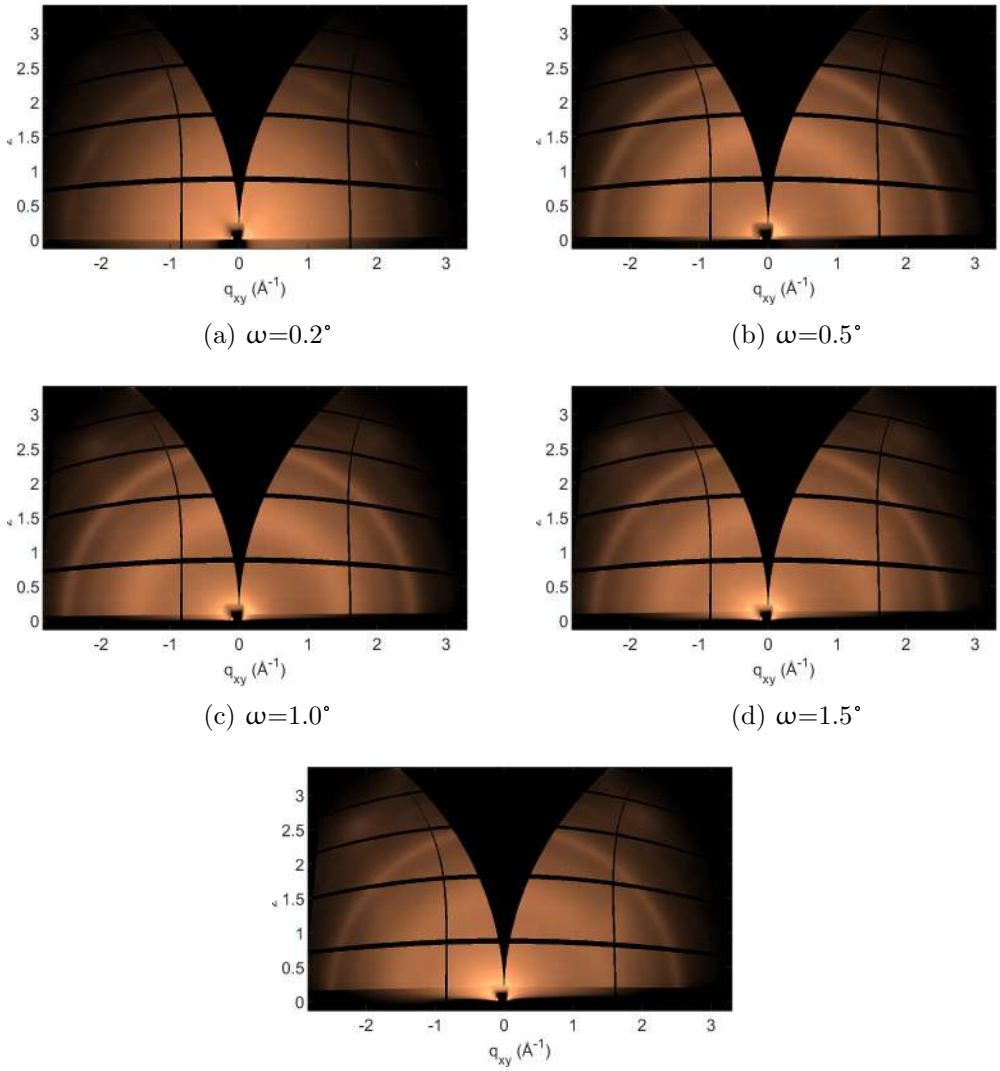

(a) ω=0.2°

(b) ω=0.5°

(c) ω=1.0°

(d) ω=1.5°

(e) ω=2.5°

Figure 3.5: An example about how different incident angles can influence the results. All this measurements have been on a sample growth for 60 minutes and then TT at 700°C for 30 minutes.

in 15h of measurement) was used. The results are reported in Figure 3.6.

Comparison between the bulk and the films shows strong similarities. In particular, the expected main diffraction from the amorphous matrix (the tetraedral distances approximated with the crystobalite $\langle 1\ 1\ 1 \rangle$ plane) and the nanocrystals ($LiGa_5O_8$) happen more or less at the same angle for all the samples, including the bulk. Different studies on the bulk ([17, 19, 20]) suggested that either a γ-Ga_2O_3[36] or $LiGa_5O_8$[34] phase can be formed (depending on the TT temperature).

Diffractograms were further corrected and analysed implementing:

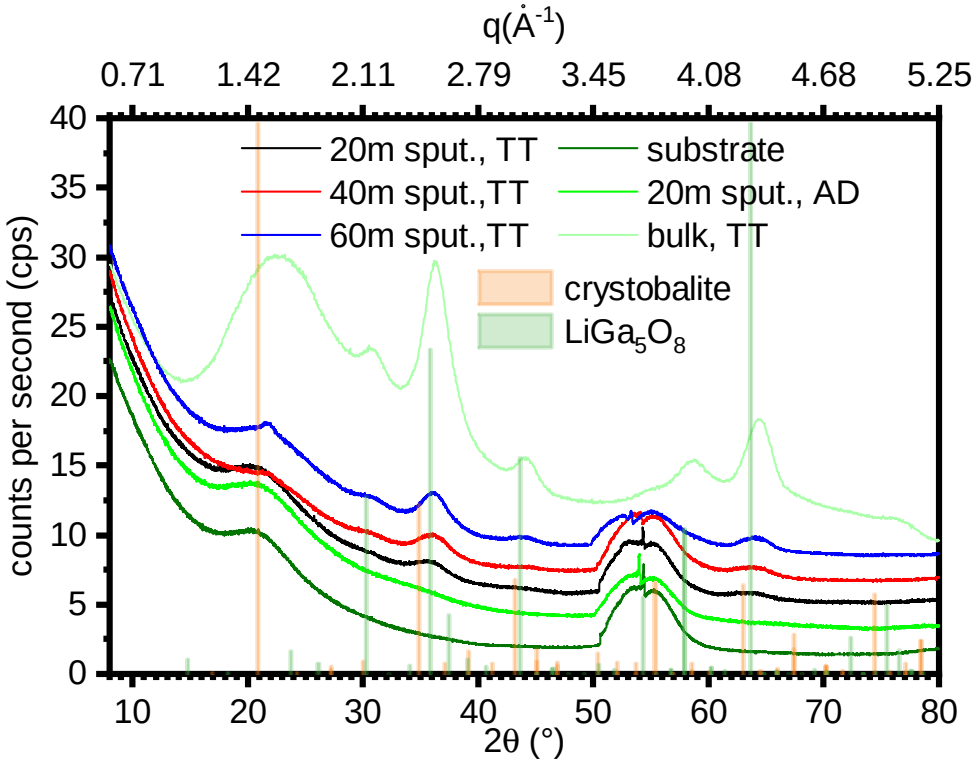

Figure 3.6: The measured difrattographs for Thermal Treatment samples, togheter with two references (in green): the substrate used, the As Deposited sample and the Thermal Treatment bulk. Vertical bars represent the expected peak patterns from two phases: $LiGa_5O_8$[34] and crystobalite[35] (low crystalline phase of SiO_2).

- normalizations respect to the acquisition time;
- normalizations respect to a local/global maximum;
- subtractions of a reference signal (either just the substrate or a not treated film);
- smoothing using a moving average with range of 5 points;

Of course, not all of them could always applied together (i.e. the two normalizations). After obtaining a clean graph, fits as shown in Figure 3.7 using a Voigt profile were performed. From the fit, and applying the Scherrer formula (Equation 3.6), the grains size have been obtained. Such data are summarized in Figure 3.8.
In Figure 3.8a I'm showing how the fits from different peaks converge to positions close to, but not the same as, the expected one. They also agree on the fact that the crystal domains should be around 3.6 nm. The exception in this second aspect is the peak at q=2.5Å^{-1}, however in Figure 3.7 we could see that at this position we

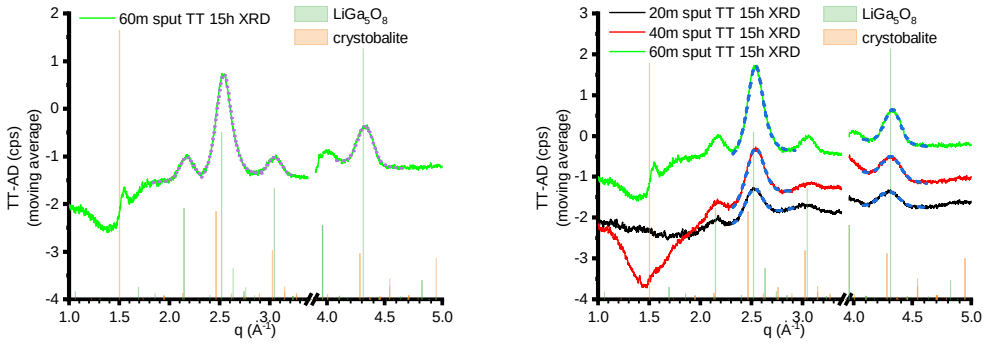

(a) (b)

Figure 3.7: Signals from samples growth for varying time and Thermal Treatment at 700°C for 30 minutes subtracted by the As Deposited one and then fitted. (a) the thicker film (∼130nm) with the 4 main peaks analysed (one by one). (b) different films with different thickness, but only 2 peaks analysed.

should expect a peak from both the $LiGa_5O_8$ phase and the matrix (crystobalite), and that the shift between the two is quite large. In general, two near broad peaks can merge together, forming a larger one that "cannot be resolved", and hence leading to a wrong estimation of the crystals domains size. In the case of the suspected diffraction, the two guessed phase have, according to the literature, a displacement between their peaks of about:

$$\Delta(q) = |q_{SiO2} - q_{LiGa5O8}| = |2.48206 - 2.54041|\dot{A}^{-1} = 0.05835\dot{A}^{-1} \qquad (3.7)$$

while the fit return a FWHM of $0.20\dot{A}^{-1}$, supporting the theory of the unresolved peak. Actually, also all the other peaks from the Ga-rich phase are overlapped with a (weaker) expected peak from the matrix, so there exist the possibility that I'm underestimating the grain size.
In Figure 3.7b I instead reported the estimated crystal size in function of the film thickness calculated starting from the peaks at $2.5\dot{A}^{-1}$ (most intense one, but unresolved) and $4.3\dot{A}^{-1}$ (second intense one but should be fully resolved). According to the later, the size of the crystallites seems to scale linearly with the deposition duration and hence with the film thickness.

3.1.4.2 Synchrotron experiments

Similar experiments have been performed also using synchrotron radiation. As mentioned above, this set-up has the advantages that it is possible to choose the desired wavelength, the measurement takes less time (seconds vs. hours) and, thanks to the 2D detector, it is also possible to access the in-plane directions.

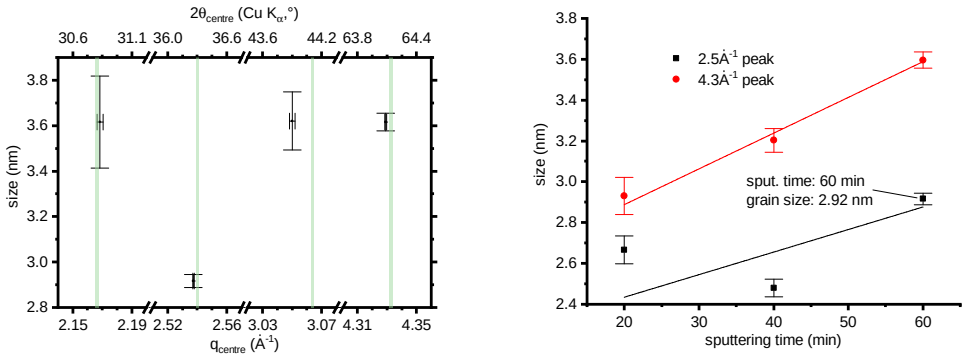

(a) (b)

Figure 3.8: The results of the fits reported in Figure 3.7 expressed as grain size; vertical bars are the expected peaks positions of $LiGa_5O_8$. (a) results from the thicker film (∼130nm). (b) results from different films with different thickness.

A comparison between laboratory XRD results and synchrotron measure is reported in Figure 3.4. According to such comparison, using synchrotron data it is still possible to have access to the peaks situated at about 2.2Å^{-1}, 2.5Å^{-1} and 3.0 Å^{-1}. There is a better resolution at low angles while at higher we can see some features from the substrate (at q=3.75Å^{-1}).
In Figure 3.9 I summarized the results collected on samples with varying thickness.

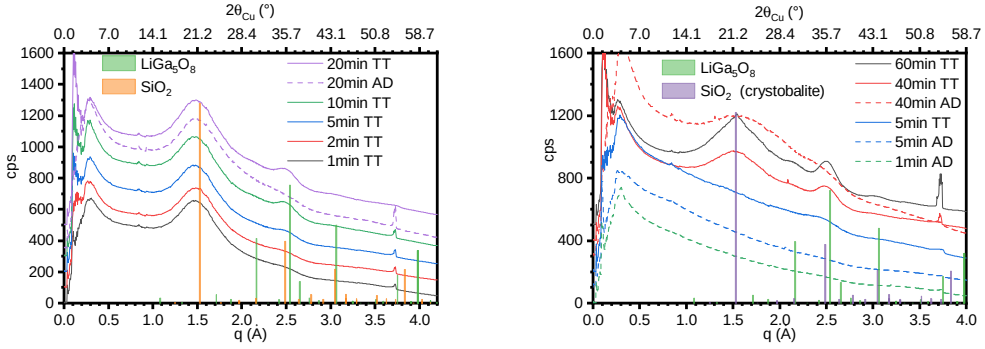

(a) substrate: thermal oxided Si (b) substrate: native oxided Si

Figure 3.9: The line scans integrated over the whole detector from images collected from samples with different thickness. (a) thinner films deposited on substrates with 150nm of SiO_2. (b) thicker films deposited on bare Si (although a layer of native SiO_2 cannot be excluded, especially on TT samples).

The peak at q=1.5Å^{-1} is always present in the line scans collected on films deposited on the substrates with the SiO_2 layer while it can be present or not on films deposited on bare silicon. The peak center/maximum for films on native oxide is just after the theoretical crystobalite peak position (see Figure 3.10b, square points) and it is very

symmetrical. Instead, in the films deposited on substrates with the SiO_2 layer, the maximum is slighter shifted to lower q (about 1.45Å^{-1}), a knee can be seen at higher q values (about 1.6Å^{-1}) and the peak centres, according to the fits, is between them, at around 1.5Å^{-1}. All these features suggest the presence of two distinct phases: one inside the films and the other that originates from the short order inside the SiO_2 amorphous layer of the substrate. The fact that the peak center of the phase from the substrate has the center at slightly lower q suggest also that the tetrahedrals units of such phase are slightly bigger than expected. This expansion can find a confirmation from XRR measurements and fits, where such layer is best fitted using a lower mass density than the one known for the bulk (for further details see subsection 3.2.3), and can be probably be explained by the high disorder degree that a fast growth led to.

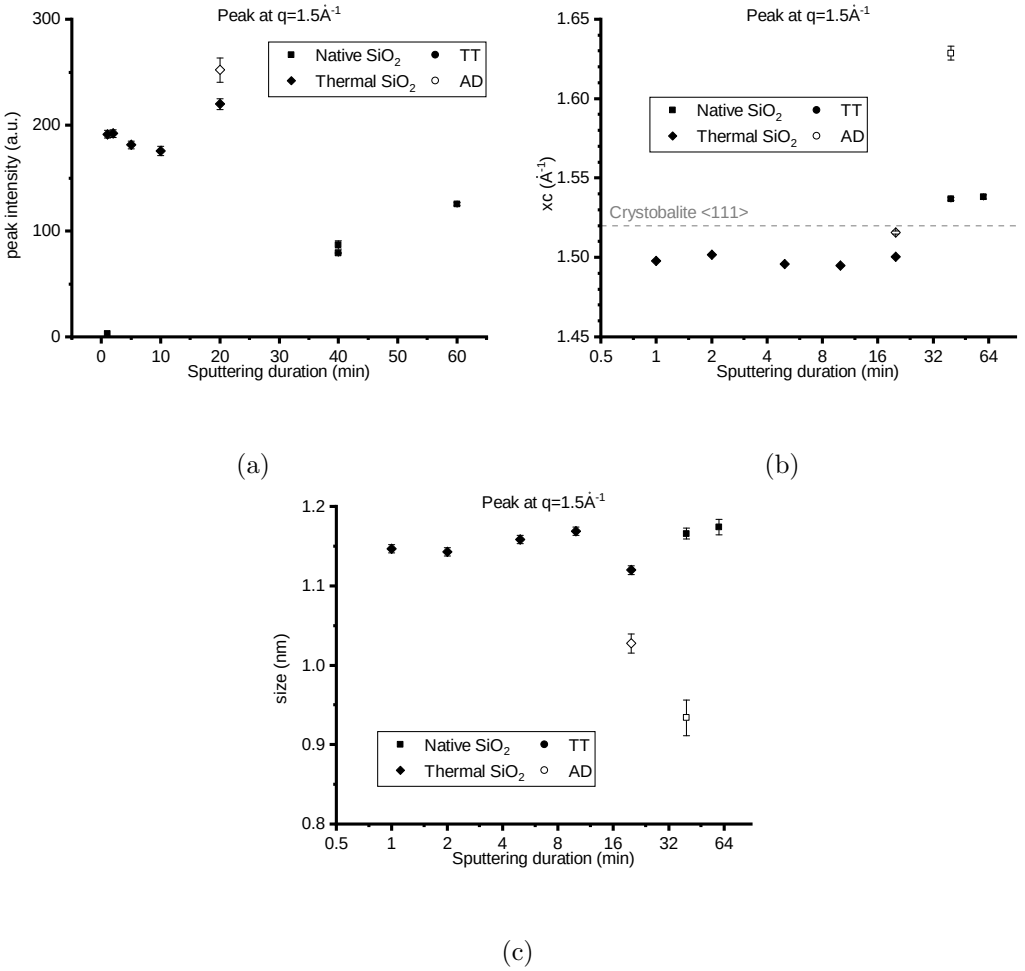

Figure 3.10: The results from the fit of the peak at 1.5Å^{-1} in the linescans in Figure 3.9, attributed to the crystobalite phase. (a) peak intensity (integrated area); (b) peaks centres (the dashed line is the expected position); (c) estimated particle size.

Moving to the features from the studied material, the main peak is still the one at

q=2.5Å^{-1}: this peak is visible in all the TT films, also the thinner ones, and its centres are reported in Figure 3.11b. According to the TT data points, such signal undergoes a step-like increase when the duration of the sputtering is about 5 minutes (corresponding to a thickness of the film of about 11 nm), so this can be somehow a critical thickness for the formation of crystallites. Note that in the other regions of the plot (including shorter sputtering duration), the growth of the signal is almost linear, indicating that the density of such crystallites doesn't change. However, some question remain open: if there is really this critical thickness for the formation of the crystallites, what happen in thinner films? There are really some crystalline region in them? What's their origin?

Those question become even more important when one look at the estimated

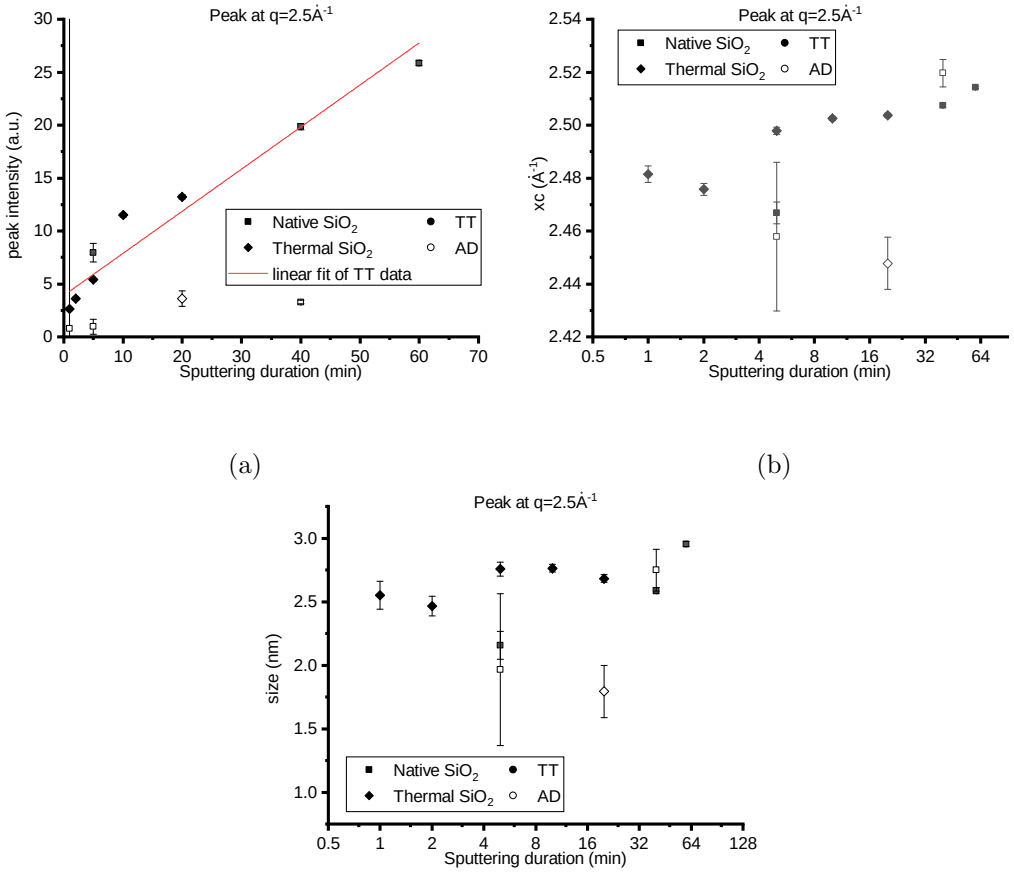

Figure 3.11: Results from the fitting of the peaks around q=2.5Å^{-1} in Figure 3.9 using a Voigt profile: (a) peak intensity (integrated area), (a) the centres of the peaks and (c) the grain size.

grain size (Figure 3.11c): they appear to be almost independent from the sputtering

duration, and they do not have a clear discontinuity around 5 min of sputtering. Another confirmation of the robustness of these data, come from the fact that the estimated size calculated from GIXRD and from lab-based XRD (Figure 3.8b) agree very well each other.

3.1.5 TT temperature results

3.1.5.1 In-house experiments

To study the effect of annealing temperature in crystal size and volumetric concentration, we prepared 7 samples, smaller than the previously described (1 cm^2 instead of 4 cm^2; they were optimized for synchrotron experiments). This synthesis lead to some artefacts in the in-house experiments, as it can be seen in Figure 3.12a. For this reason, we used the bare Si substrate as background curve. The results of such subtractions are reported in Figure 3.12b.

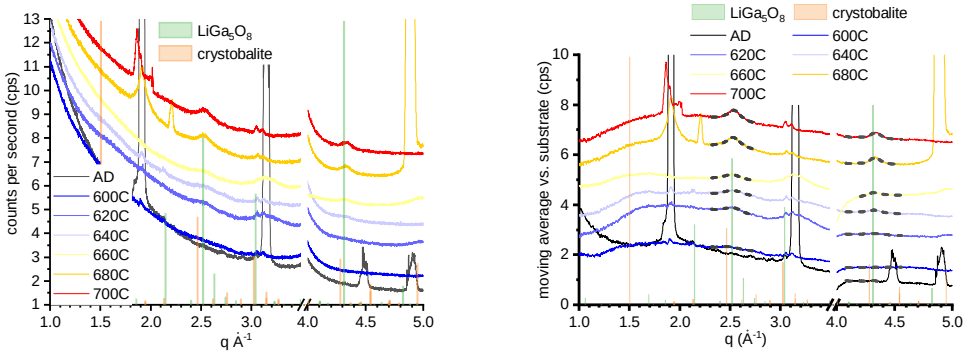

(a) (b)

Figure 3.12: Line scans from films treated at different temperatures with the fits result reported as dark dashed lines. (a) raw data counts per second, (b) the same data but corrected for the substrate signal and then smoothed (range of ±3 points) for removing eventual spikes.

Both the peak families (the one at q=2.5$Å^{-1}$ and the other at q=4.3$Å^{-1}$) increase with increasing temperature, suggesting that higher portion of the film undergoes the amorphous to crystalline phase change. Moreover, both peaks grow toward a saturation limit (Figure 3.13a). For this reason, the data have been fitted by an exponential saturated model. This choice can be justified taking account that there should be two different plateau for the signal intensity: one before the TT start to take effect and one when the NP cannot growth any more (probably due to physical constrains and/or to the lack of more available Ga nearby). During the process an exponential

growth can be used since it is thermically activated. The formula used is:

$$Y = Y_{min} + (Y_{max} - Y_{min}) \cdot \left[1 - \exp\left(-\frac{(T - T_{start})}{T_K}\right)\right] \tag{3.8}$$

with the additional condition that Y cannot be less then Y_{min}. Here Y denote the peak integrated intensity, with Y_{min} and Y_{max} representing the two plateau (Y_{min} was fixed to 0 counts during the fit), T_{start} being the temperature at which the effect starts to take place and T_K a temperature constant associated with the activation energy of the process. In Figure 3.13a there are the curves associated to such fit and the relative associated parameters. Interestingly the energy required for the formation of the NPs are quite low (corresponding to 34°C and 50°C for the 2.5Å^{-1} and the q=4.3Å^{-1} peaks, respectively).

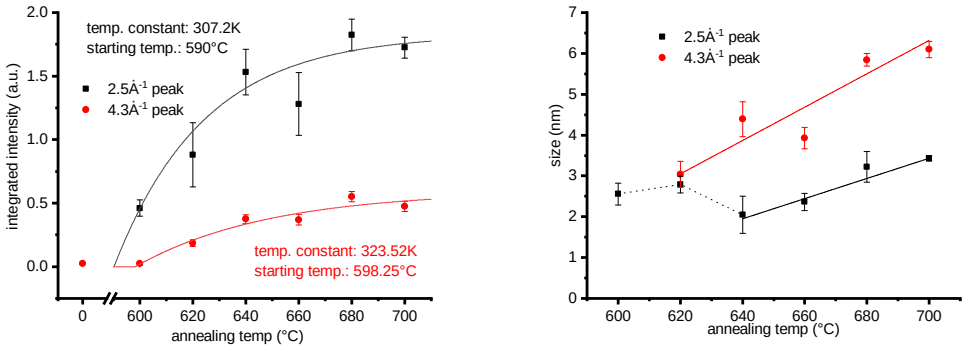

(a) (b)

Figure 3.13: The results from the fits showed in Figure 3.12b: (a) peaks intensities (togheter with additional exponential fits) and (b) particles size.

The size of the crystallites follows a linear regime (see Figure 3.13b). However, the size grow at two different rates, supporting the theory of multiple origin of such peaks presented in the end of section 3.1.4.1.

3.1.5.2 Synchrotron experiments

The same samples were also measured using synchrotron radiation. As stated before, such samples were optimized for this measurement, and indeed the quality was way better, as shown in Figure 3.14a.

From a qualitative point of view, these measurements confirm that higher temperatures lead to higher peak intensities. Such change is steeper when moving from 680°C to 700°C, the maximum probed temperature. At this temperature, two additional peaks (situated at about 2.0 and 3.0Å^{-1}) can be recognized, as in Figure 3.7a. Indeed, this behaviour is also confirmed by quantitative fits (Figure 3.14b), with the

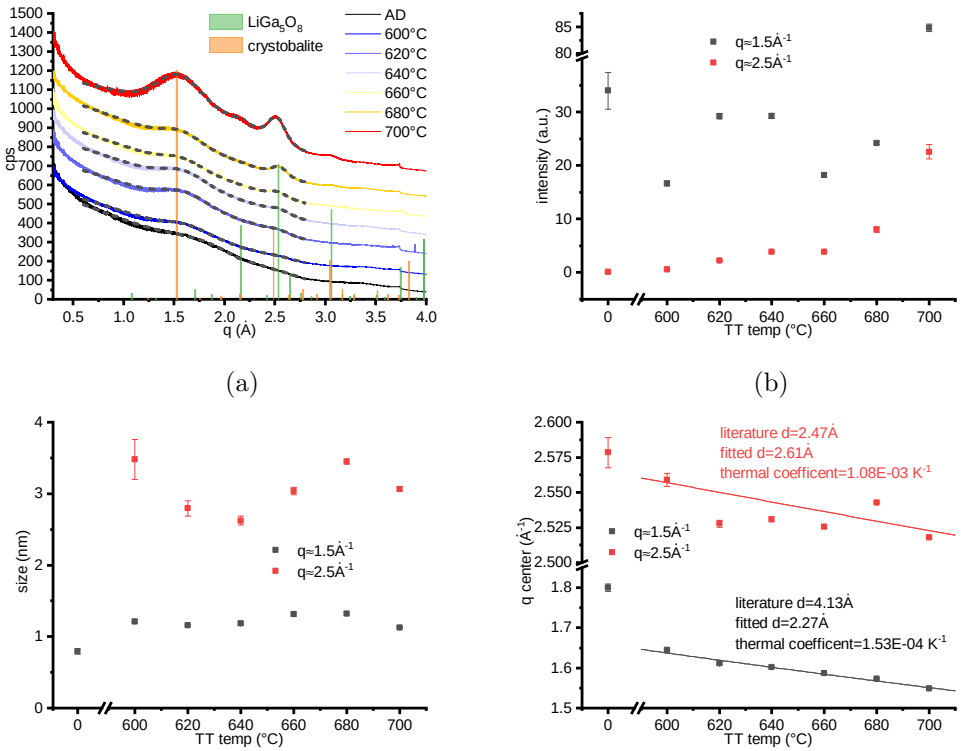

Figure 3.14: (a) Line scans from GIXRD collected on films treated at different temperatures together with the fits at q=1.5Å^{-1} and q=2.5Å^{-1}. From such fits,(b) peaks intensity, (c) broadening (converted to crystallites size) and (d) centres have been calculated and evaluated respect to the TT temperature.

crystobalite peak tripling its intensity in such range. However, the peak of interest ($LiGa_5O_8$, 2.5Å^{-1}) has a less steep growth (but still, the intensity grows by a factor of 2). This increase in the integrated area (proportional to the number of probed crystal planes) seem to have also the side-effect to decrease the size of the NCs when the temperature is too high (in Figure 3.14c the maximum is located at 680°C), suggesting that in this regime the formation of new nucleation centres is faster than the growth itself, and one should take this in account when optimizing the annealing.
The last quantity presented in Figure 3.14d is the centres of the peaks. The q position tends to move to lower values. This difference is not barely a thermal expansion. In case of thermal expansion, the expected values for the thermal coefficients should be 2/3 order of magnitude smaller (theoretically, one should expect something like $10^{-6}K^{-1}$ for glasses; for fitted ones see the graphs) and the intercept of the linear fit should give the room temperature inter-plane distance (see the graphs for the fitted and the theoretical values according to the literature[34, 35]).

3.1.5.3 Particles isotropy

One of the advantages of GIXRD is its capability to also probe scattering vector not perpendicular to the sample surface.
According to AFM measurement, we expected particles with a lateral width way higher than the vertical size (see for example Figure 5.7). To have a confirmation of that, I have extracted different linescans from the image collected on the sample TT at 700°C, specifically using the representation showed in Figure 3.3b (Polar space) and extracting the data every 10° in Ψ. Such line scans are reported in Figure 3.15.

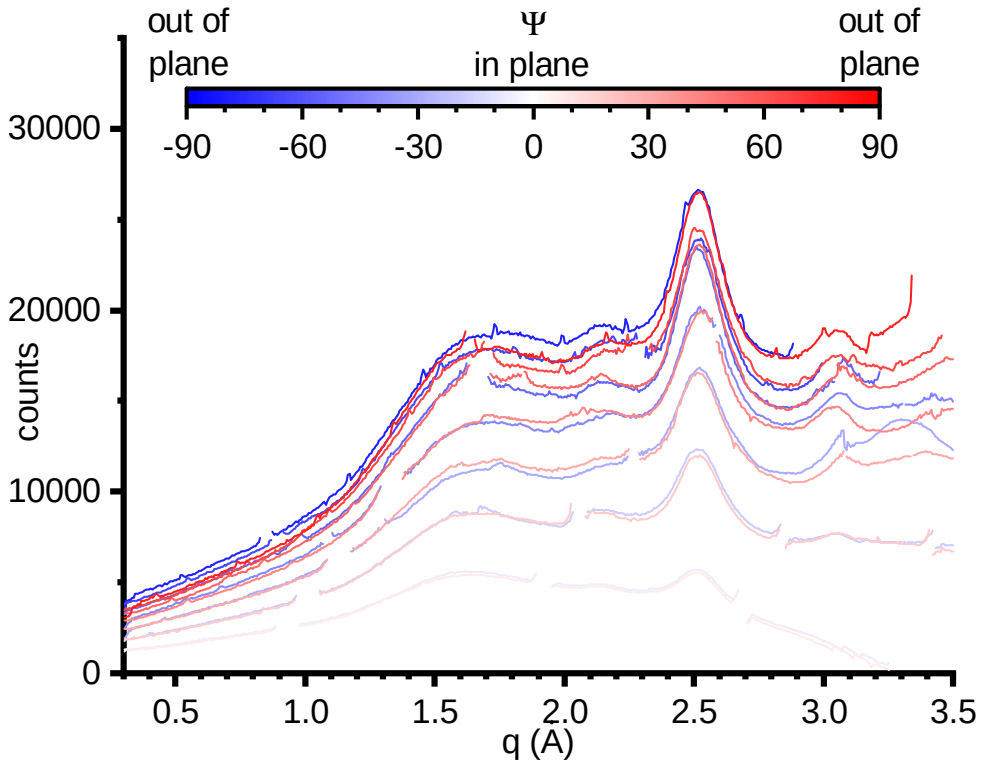

Figure 3.15: Line scans extracted from a single GIXRD image sectioning the ring at varying Ψangles (inclination).

Line scans obtained from positive and the corresponding negative angles (Φ) from the surface normal have similar intensity, and this intensity seems to be larger for directions closer to the in-plane one (but some systematic errors can be present due to geometrical factors). For our purpose, the most important parameter is the FWHM of such peaks, that has been extracted (starting from the fitting of the peaks through a Voigt profile) for 4 different positions and is reported in Figure 3.16a.
In my case, this analysis doesn't usually show any difference in size. One noticeable exception is the peak situated at $3\dot{A}^{-1}$ and only for what concern the positive tilting:

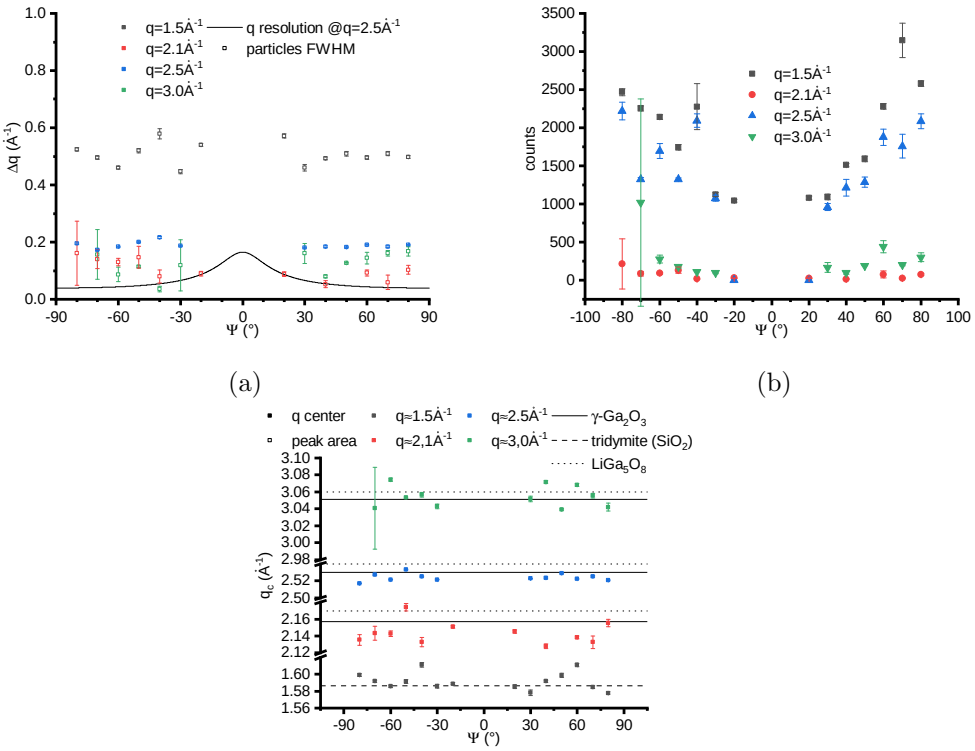

(a) (b)

(c)

Figure 3.16: Peaks parameters extracted from the line scans reported in Figure 3.15. (a) FWHM; (b) integrated intensity; (c) experimental (colored marks) and expected (horizontal lines) peaks positions.

in this case only, the peaks seems to be sharper (and the NPs larger) closed to the out-of-plane direction. However, the FWHM from the other datasets and the fitted intensities (Figure 3.16b) of such peaks lead me to consider such trend only as a statistical possibility.

The third extracted parameter (Figure 3.16c) concern instead the peaks position compared to the expected positions from literature. Also in this case, the data point are quite scattered around the theoretical value and this uncertainty is greater than the difference between the two hypothized phases ($LiGa_5O_8$ and γ-Ga_2O_3), but often the γ-Ga_2O_3 phase is closer to the experimental values.

The solid line in Figure 3.16a represents the broadening due to the Elettra experimental setup, obtained by applying the consideration of [37] to the XRD1 beamline. In particular, as reported in Figure 3.17a, in our case the main contribute to the broadening of the diffracted peak is the divergence of the primary beam.

The points presented in Figure 3.16a have been calculated using

$$B_{sample} = \sqrt{B^2_{measured} - B^2_{setup}} \tag{3.9}$$

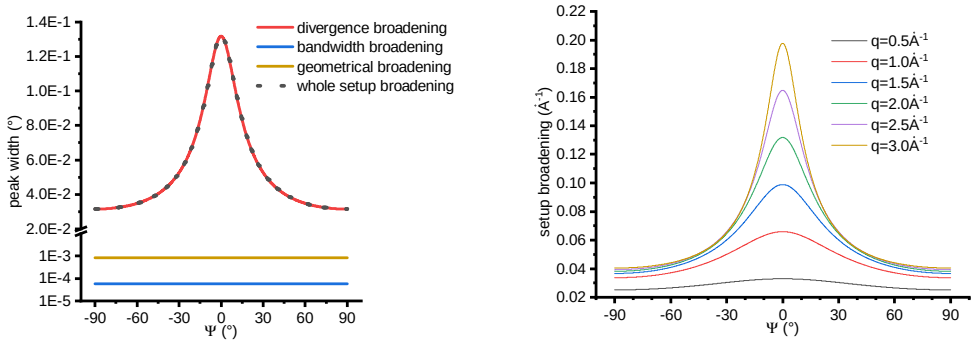

(a) (b)

Figure 3.17: The expected broadening of a peak at the Elettra XRD1 beamline (or at least with the setup used) versus the Ψ direction probed; for optimal Scherrer analysis, the experimental broadening should be deconvoluted in this component and the one that arise from the sample morphology. (a) the components that originate such broadening; (b) how such broadening evolve by probing different scattering vectors.

where B denote the broadening of the investigated peak, and the subscripts refer to the components arising from the sample morphology (sample), the actually measured/fitted broadening (measured) and the experimental setup used (setup), for which the closer curve reported in Figure 3.17b has been used for each different peak family.

3.1.6 TT duration results

3.1.6.1 Lab experiments

A total of 7 samples were prepared by depositing the glass-ceramic on HF cleaned Si and then being treated at 700°C for different times. Additionally, also the thicker TT sample presented in section 3.1.4.1 is compared (and marked with an asterisk).
Respect to the previous investigations, here the differences appear to be smaller, both in intensity and in the shape of the peaks. A notable exception are the pattern from the films TT for very short time (1 and 5 minutes) that do not show clear peaks.
These similarities are confirmed also by the parameters obtained from the fits (Figure 3.19).
The intensity of the peaks, that should be proportional to the crystalline volume, slightly increase with increasing the annealing time, following what seems to be an exponential regime (x scale in Figure 3.19a is in $\log_2$). This increasing in the volume however does not correspond to an increase in each NP size, at least not in the whole tested range. The data presented in Figure 3.19b show that during the process

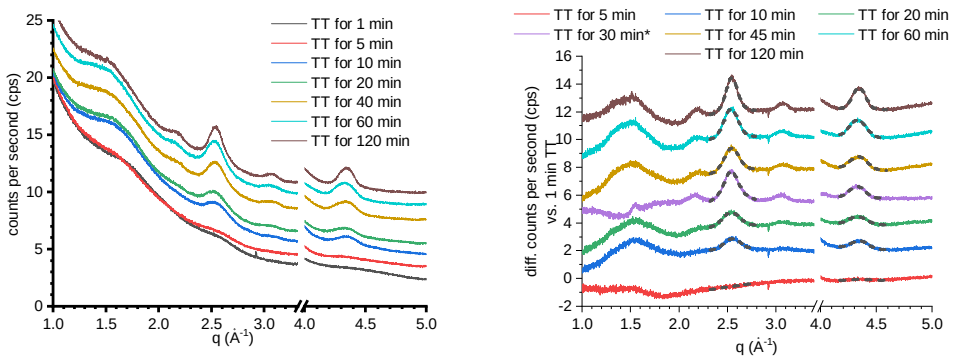

(a) (b)

Figure 3.18: Laboratory XRD pattern collected on films TT at 700° for different times. (a) raw data and (b) the same data corrected by removing the signal from the film treated for just 1 minute. *Please note that the film treated for 30 minutes is the one already presented in section 3.1.4.1, deposited and measured further in time respect to the others (and with many other deposition in between that could slightly modify the target surface), so the discrepancy with the other patterns is normal.

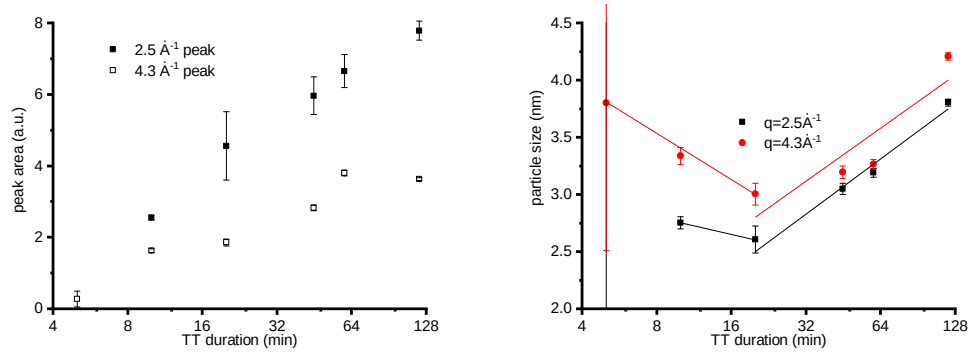

(a) (b)

Figure 3.19: Parameters from the fits in Figure 3.18b. (a) peak intensity and (b) calculated particle size; the lines are just guidelines for the eye.

different phenomena happen, starting from the formation of somehow big regions (10 minutes of TT) that later on shrink (minimum at around 20 min) and then grow again. This mean that the formation of the crystalline regions does not obey to a law dominated by a single activation energy.

3.1.6.2 Synchrotron experiments

The same sample described before were also characterized with synchrotron light. The powder-like diffractograms of this characterization are presented in Figure 3.20.

These measurements confirm what observed with the laboratory scale instrument,

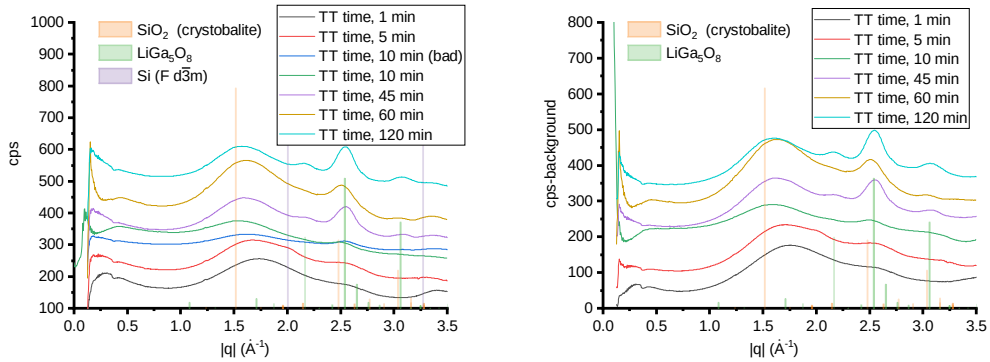

(a) (b)

Figure 3.20: Synchrotron GIXRD pattern collected on films TT at 700° for different times. (a) raw data and (b) the same data corrected by removing the signal from the substrate.

although the influence of the time doesn't appear so linear in this case, especially if one consider not just the main peak (at 2.5 $\dot{A}^{-1}$) but also the side ones (at 2.2 and 3 $\dot{A}^{-1}$).

GIXRD maps of samples treated for very long times, such as 120 min (in Figure 3.21a),show that some φ directions have higher intensities than others. This difference can be highlight by analysing some integrated linescans around the region of interest, ie. from 2.45 to 2.65$\dot{A}^{-1}$ as reported in Figure 3.21b.

These difference means that there are some preferred orientation of the crystallites (some crystal planes are more common, Equation 3.3). Comparing the peak positions and the intensities at different Φ (Figure 3.21b), they seems to be somehow correlated, in particular, when the intensity is higher, the peak appears at a lower q. The experimental peaks are always centred between the theoretical positions of $LiGa_5O_8$ (2.54041$\dot{A}^{-1}$) and γ-Ga_2O_3 (2.64223$\dot{A}^{-1}$), so, maybe, the observed difference can be related to a different ratio between the two phases indicating that the $LiGa_5O_8$ prefer to orient itself in a given direction (the one highlighted in Figure 3.21a is the $LiGa_5O_8$ one with the $\langle 111 \rangle$ direction perpendicular to the film plane, with the crystalline structure being cubic).

This analysis has been performed on samples treated for different times (Figure 3.22) and for different incident angles (Figure 3.23).

3.1.7 Multi layered sample

Finally, we collected XRD data on multilayered sample, with thicknesses higher than 130 nm. For further details about these samples, see section 3.3.

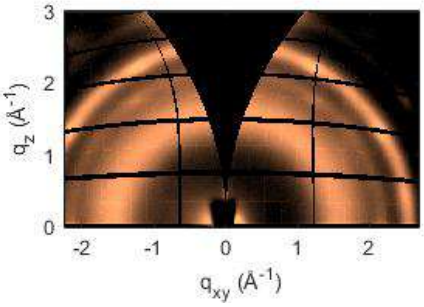

(a)

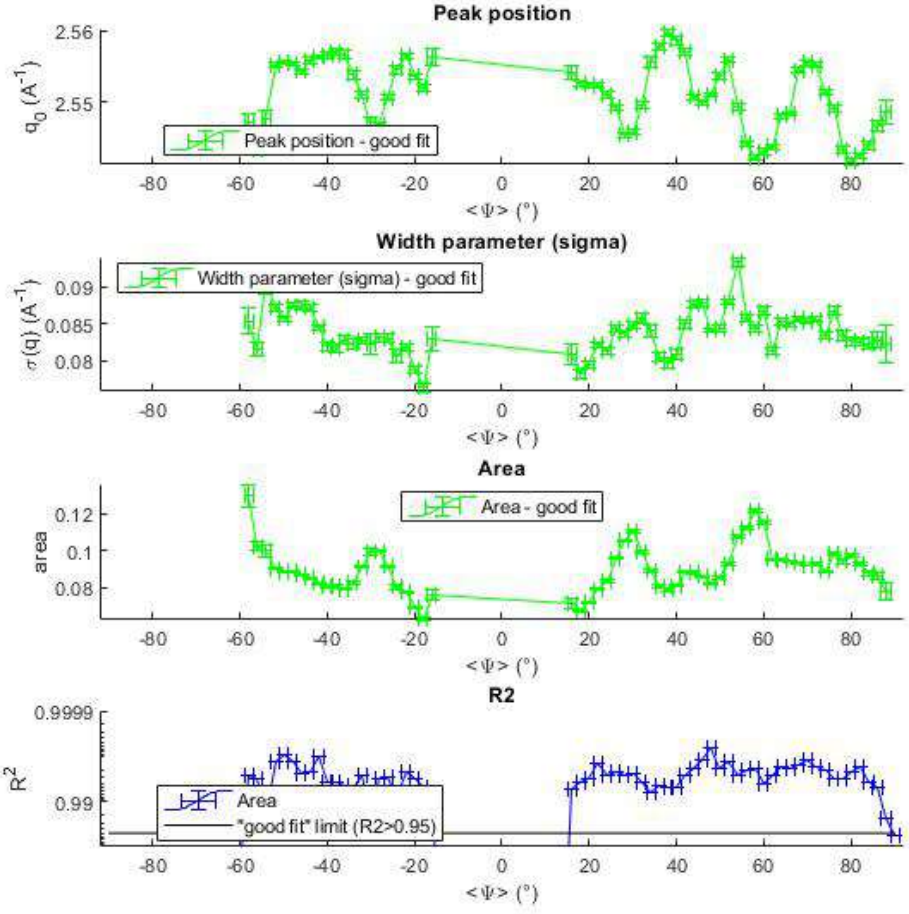

(b)

Figure 3.21: (a) synchrotron GIXRD map collected on a film TT at 700°C for 120 minutes and Figure 3.21b parameters from fitting the diffraction peak (gaussian+linear baseline) at different Ψ orientations.

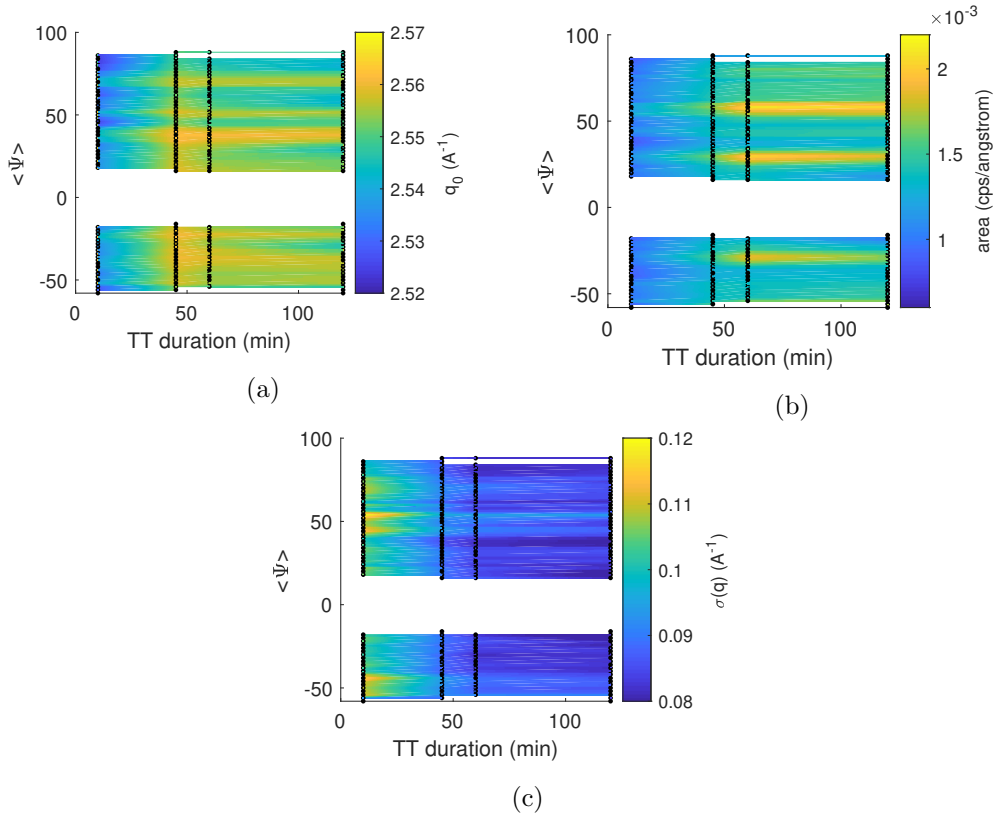

Figure 3.22: Data obtained trough the analysis described shown in Figure 3.21 performed on samples TT for different amount of times. Fit quality on samples treated for shorted periods (1 and 5 minutes) were bad, so they are not shown. (a) peak positions, (b) peak integrated intensities and (c) peak widths.

The diffractographs are shown in Figure 3.24a, and the results of the fitting procedure about crystallites size and intensities are reported in Figure 3.24b and Figure 3.24c respectively. The results confirm the same relation between peak intensity and center shift described in previous sections. All the fitted parameters agree with the previous data with the exception of the estimation of the particle size.

3.2 XRR

3.2.1 XRR theory

X-Ray Reflectivity (XRR) is a thin film characterization technique in which the X-rays are optically reflected on the film so to form interference pattern thanks to the films geometry. Depending on the instrumentation and the quality of the film itself, this technique can handle films of 1 nm to 1µm in thickness and can be used to probe different layers on top of each others. For optical reasons, symmetrical/specular

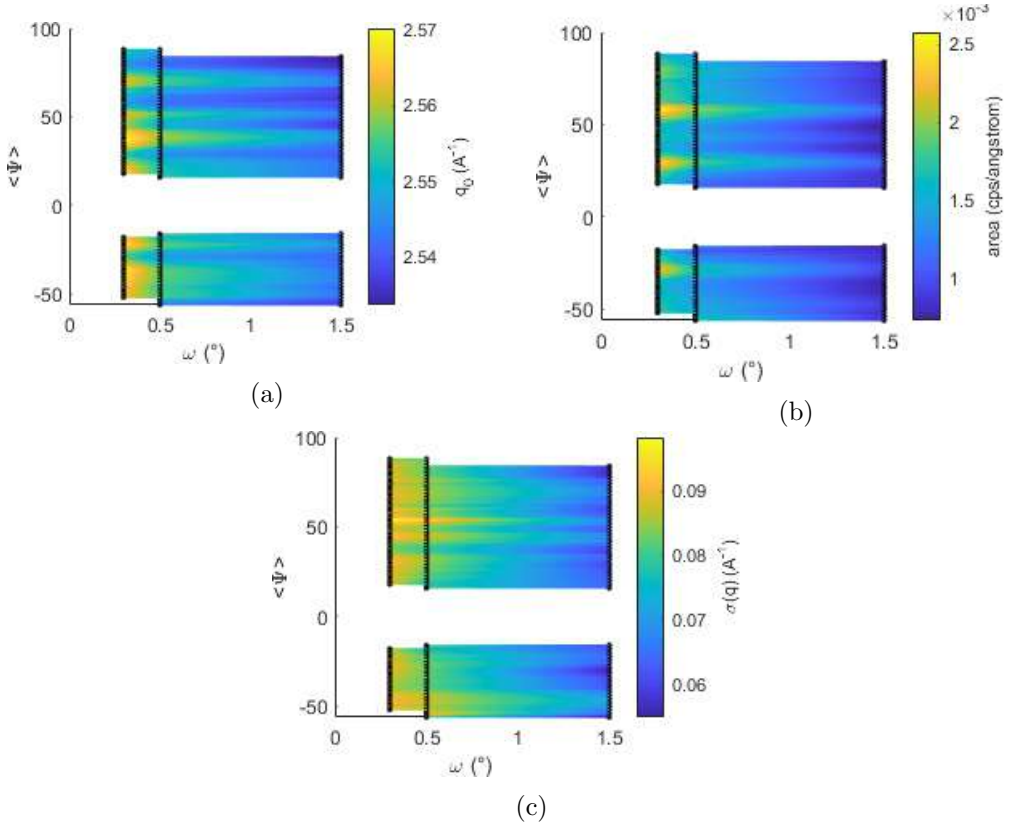

Figure 3.23: Data obtained trough the analysis described in Figure 3.21 performed on the sample TT for 120 minutes measured at different ω. (a) peak positions, (b) peak integrated intensities and (c) peak widths.

conditions between the incident and the reflected beams must be used and usually the probed angle (defined as 2θ in section 3.1) between these two beams is between 0 and 10 degrees. In general, it's not destructive, but sometimes the X-ray can modify the sampled material due to the degradation promoted directly by the beam or by reactive chemical species created by it (i.e. O_3).

To understand the theory behind such measurement, it's important to start from the refractive index of typical materials at x-ray wavelengths:

$$\tilde{n} = 1 - \delta + \imath\beta \tag{3.10}$$

where δ and β represent the real and imaginary part of the refractive index, and they assume small positive values (typically, respectively $10^{-6} \div 10^{-5}$ and $10^{-8} \div 10^{-7}$). The real part of the refractive index strongly depend on the electronic density according to the formula[38, eq. 9]:

$$\delta = \frac{e^2 \rho_e}{2\epsilon_0 m_e (2\pi c)^2} \lambda^2 = \frac{r_0 \lambda^2}{2\pi} \rho_e \tag{3.11}$$

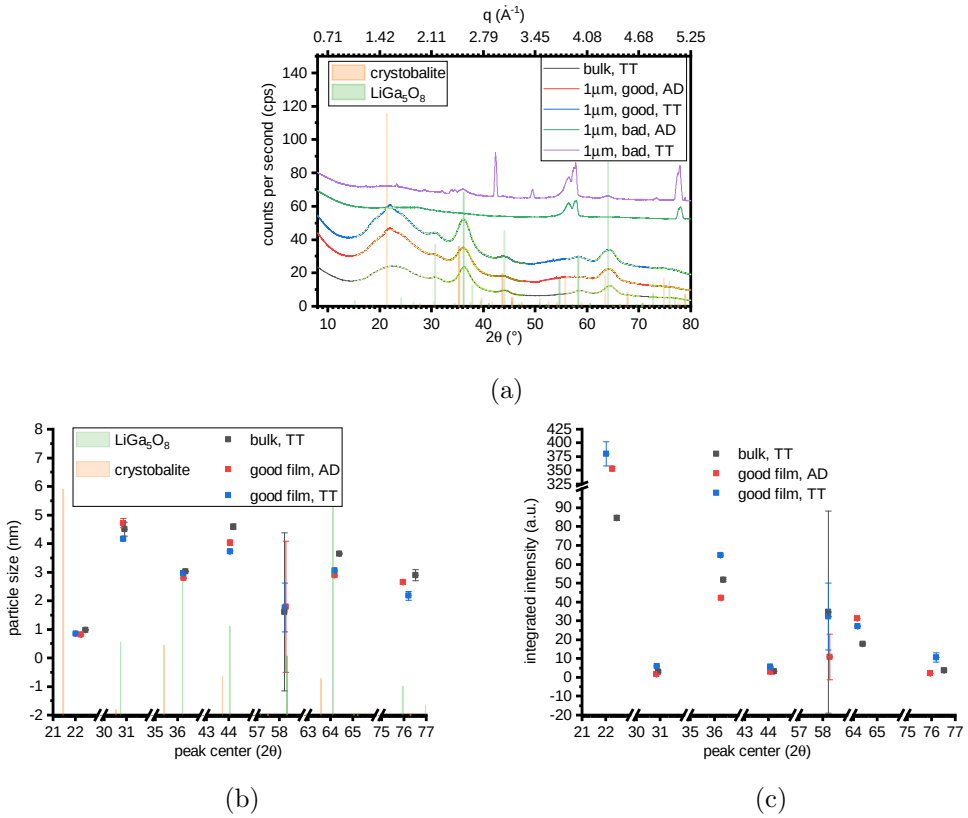

Figure 3.24: Laboratory XRD pattern collected on very thick (either 1µm thick films or bulk slab) samples. (a) linescans; (b) crystallites size analysis; (c) peak intensity. "good" and "bad" refer to the optical quality of the film that depends on the morphology at the µm scale (see Figure 5.13 and Figure 2.2 for more details).

with e the electron charge, ρ_e the electron density, ϵ_0 the dielectric constant of vacuum, m_e is the mass of the electron, c is the speed of light and λ the x-ray wavelength used in the experiment (in my case 1.54Å), so knowing δ can give useful informations about the electronic density of the medium (and eventually about the mass density of it, if the exact elemental composition is known).
Experimentally, this value is accessible trough the Snell law:

$$n_1 \cos(\theta_1) = n_2 \cos(\theta_2) \tag{3.12}$$

that can be simplify in

$$n_{mat} \cos(\theta_{mat}) = n_{air} \cos(\theta_{air}) \rightarrow n_{mat} = \cos(\theta_c) \tag{3.13}$$

with n_{mat} being the investigated material refractive index and θ_c the critical angle of total external reflection (calculated from the boundary between the film and the air). Together with Equation 3.11 this lead to:

$$\cos(\delta_c) = \Re(n) = 1 - \delta \approx 1 - \frac{\theta_c^2}{2} \rightarrow \theta_c \approx \sqrt{2\delta} \propto \sqrt{\lambda^2 \rho_e} \tag{3.14}$$

A second important aspect that can be obtained using this technique is the film thickness, including the thickness of layers under the top one (and for so, experimentally difficult to measure). This information appears in the reflectivity graph as a series of minima and maxima caused by constructive and destructive interference between two different path that the x-ray can take: one that involves the investigated layer, and the other that doesn't. The spacing between 2 fringes is:

$$\Delta(q) = \frac{2\pi n}{d} \tag{3.15}$$

in reciprocal space (q) or

$$\Delta\theta \approx \frac{\lambda}{2d} \tag{3.16}$$

in 2θ space[3], with d representing the film thickness. The height of these oscillation is instead proportional to the difference between the two layers electronic densities and film roughness.

Finally, also a third aspect can be measured using this technique: the surface roughness of each layer. Normally, according to Fresnel reflectivity law [39], we should expect that the reflected signal should decay at a speed of

$$R = r^2 \approx \left(\frac{2\theta}{\theta_c}\right)^{-4} \tag{3.17}$$

where R is the reflected signal and r is the Fresnel reflection coefficient (either for s- or p-polarization), but usually it is stronger, and the difference between the actual and the theoretic value must be attribute to the the scattering of the surface. The theoretical decay should be corrected to

$$R_{exp} = R_{theo} \cdot \exp\left(-q^2\sigma^2\right) = R_{theo} \cdot \exp\left[-\left(\frac{2\pi}{d}\right)^2 \sigma^2\right] \tag{3.18}$$

With d representing the film thickness and σ its Root Mean Square (RMS) roughness. Considering these 3 main contributions, during a typical measurement, we can distinguish three different regimes:

1. at the beginning (before $\theta = \theta_c$) the signal is dominated by the direct beam (eventually partially blocked by the sample itself) or the full reflection of it;

2. after θ_c the signal drop rapidly (faster for rougher samples) and with modulations according to the thickness of the films;

[3]Actually the maximum m is located at $\theta_m^2 \approx m^2 \frac{\lambda^2}{4d^2} + \theta_c^2$, but for simplification, the θ_c^2 term was neglected.

3. at the end, the incident beam is completely adsorbed by the sample itself and the detected intensity is basically just a background noise consisting of few (depending on the acquisition conditions) counts per seconds.

3.2.1.1 Data analysis

The analysis of XRR patterns can be performed either qualitatively or quantitatively. For the latter case, some dedicated fitting softwares are required, and in my case I used two of them: X'Pert Reflectivity (today replaced by AMASS [40]), from the difractometer vendor, and StochFit ([41]). Both have their own advantages and drawbacks. From the point of view of the information they handle (both as initial and best parameters), X'Pert software deals with more "basic" quantities (i.e. every layer thickness and mass density), while Stochfit works with "just" the electron density profile (normalized to the substrate), without converting it to anything else. One thing to consider is the fact that both software packages are quite old (last updated in 2009) and especially for what it regards the Stochfit one, their compatibility with modern computers is very poor, so finishing the fits or even running the softwares wasn't so easy.
Thickness analysis can be calculated also in a qualitative way by converting XRR data in real space. As an example, a couple of simulated pattern are provided in Figure 3.25, together with a table with the parameters used to compute them (Table 3.1). As it can be seen, there are three different representations for each example. These are alternative ways to convert/look at the same data. In particular, the conversion between the 2θ-space and the q-space is performed using the formula[42]:

$$Q(\theta) = \frac{4\pi}{\lambda}\sqrt{\cos^2(\theta_c) - \cos^2(\theta)} \tag{3.19}$$

where θ is the incident angle, Q(θ) is the corresponding q-vector, θ_c is the critical angle and λ is the x-ray wavelength. The value θ_c must be known before applying the formula and the converted data will loose the information about it, so fitting algorithms that work in q-space (like the one of Stochfit) cannot really estimate this quantity but they have to calculate it before the fit.
To obtain all the data representation, the following procedure has been used:

1. **collect** an XRR scan up to a certain (small) angle (Figure 3.25a and (b));

2. **pad/decimate** such data by adding/removing the background (this is necessary to optimize the data for the next steps);

3. **convert** the θ-spaced data to q-space using the formula in 3.19 (Figure 3.25c and (d));

4. **interpolate** the q data so to have an equi-spaced vector (this is needed to get a better result in the next step);

5. calculate the **FFT** of q data so to obtain a distribution (of thicknesses) in the real space (Figure 3.25e and (f)).

layer #	**comp.**	**ρ [g/cm³]**	**thickness [nm]**	**roughness [nm]**
1	SiO_2	3	10	0
0	Si	2	∞	0

(a)

layer #	**comp.**	**ρ [g/cm³]**	**thickness [nm]**	**roughness [nm]**
2	Sn	6	50	0.6
1	Ge	4	10	0.4
0	Si	2	∞	0.2

(b)

Table 3.1: The parameters used to simulate the data in Figure 3.25. (a) for the left column and (b) for the right one.

The effect of roughness can be better see in Figure 3.26 where, to the system described in Table 3.1a, was applied a roughness of 0.5nm (RMS) to either the substrate, the film surface or both.
As it can be seen from such graphs and as already stated, the whole informations can be found in the central portion of the data, and they are surrounded by the signal-to-noise ratio limit of the instrument (higher θ limit) and the critical angle (θ_c) whose actual position in the pattern is not really universally accepted among the community, but usually it's found between the (local) maximum before the drop (θ_{max}) and the angle which has an intensity equal to half of such maximum ($I(\theta_{max/2}) = I(\theta_{max})/2$). More informations can be found in [38] or in some technical brochures from the instrument makers such as [43].

3.2.2 Qualitative results

3.2.2.1 Thermal treatment effect

Here, I will present data on film morphology evolution during the TT.
For doing so, sets of 4 films with different thickness were prepared. Of those films,

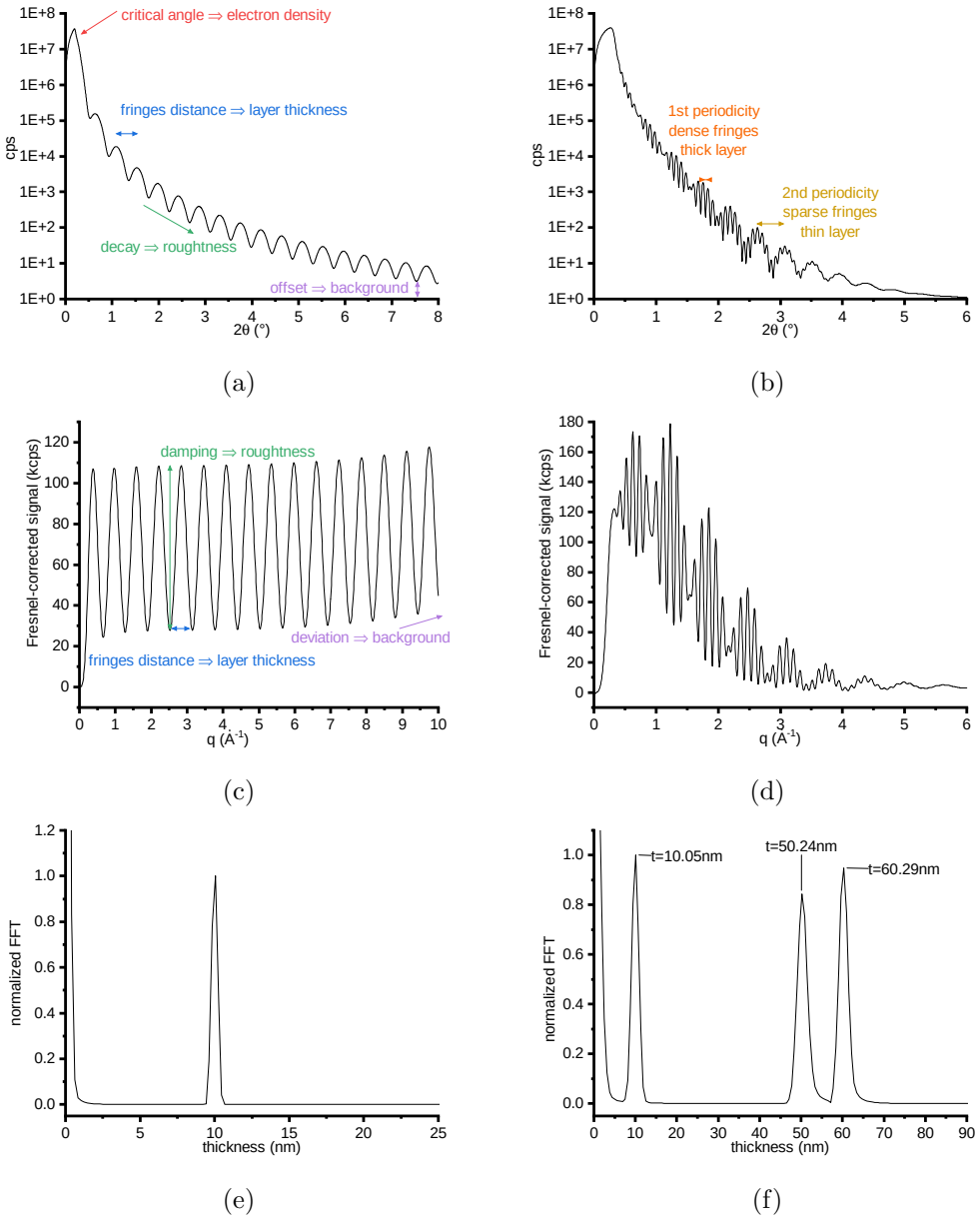

Figure 3.25: Simulated XRR patterns for a single layer ((a), (c) and (e)) and a bilayer ((b), (d) and (f)) systems. The three representation are the "as-recorded" pattern in a diffractometer ((a) and (b)), then converted in q-space and corrected according to Equation 3.17 ((c) and (d)) and finally transformed in real space distribution with the FFT algorithm ((e) and (f)). In color there are highlighted the features influenced by the measurable quantities. Note that the FFT can easily determine the starting thickness and, with some limits (expecially due to the fact that the data are finite and sparse), also the roughness (in Table 3.1).

the ones deposited for 10 and 20 minutes have been tested. On each tested film, 2 different measurements were collected, one before and one after the annealing. The results of these experiments are collected in Figure 3.27.

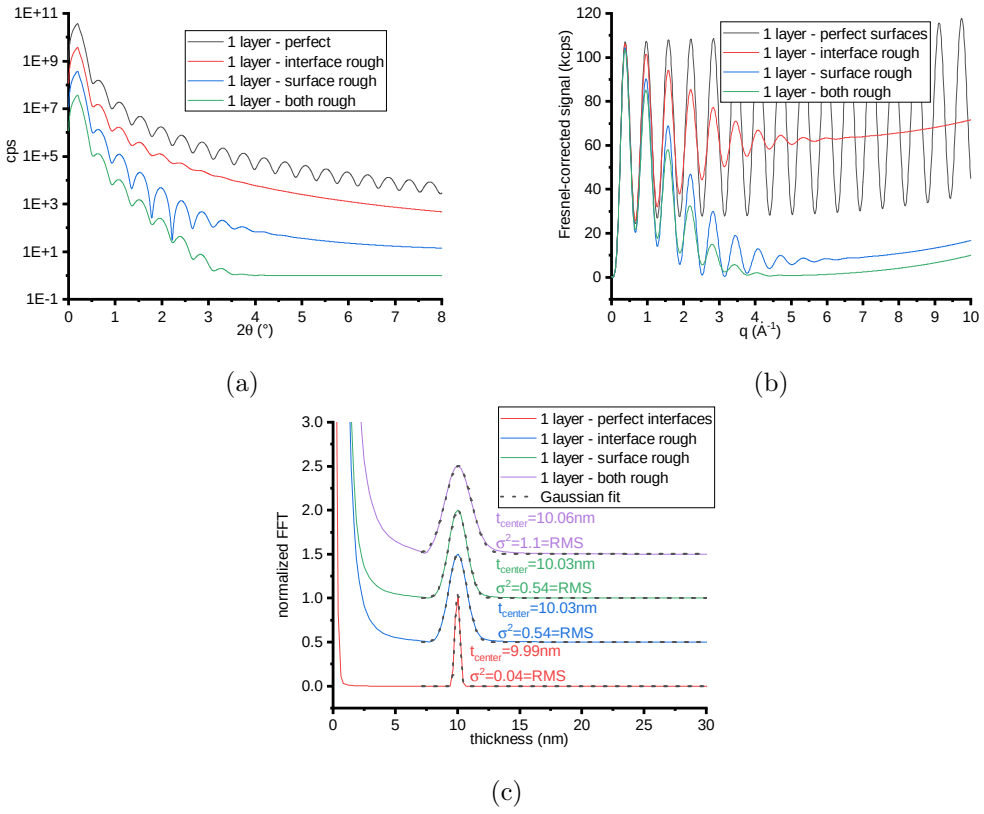

Figure 3.26: Simulated XRR pattern for a single layer system, with different roughness. The three representation are (a) the "as-recorded" patter in a diffractometer, (b) then converted in q-space and corrected according to Equation 3.17 and (c) finally transformed in real space distribution according to FFT algorithms. Note how the peaks widths from the fits of the FFT datasets are very close to the sum of the setted rough (0.5 nm RMS for both the surfaces) and the one coming from the data manipulation (from the perfect layer fit).

This experiment gives us an hint on the quality of the steps used to produce our films. In perfect conditions, the curves should look the same, but this is not the case. A slight difference in the periodicity was expected due to the fact that the RF sputtering deposition is not uniform over a large area, but I have also found other differences, mainly related to the intensity of the fringes.

The main goal for this characterization was to understand what is the effect of the TT on such measurements. As it can be seen, such effect vary a lot from sample to sample. One quite common effect is the change of the large fringe (between 3 and 8° in 2θ) in the AD samples that usually turns into a modification of the bump present in this region, corresponding to a very thin (probably $t < 1$nm) layer. The intensity of this modification, however, is also not constant: sometimes it disappear completely while other it just blur out. Both cases are compatible with a (partial) incorporation

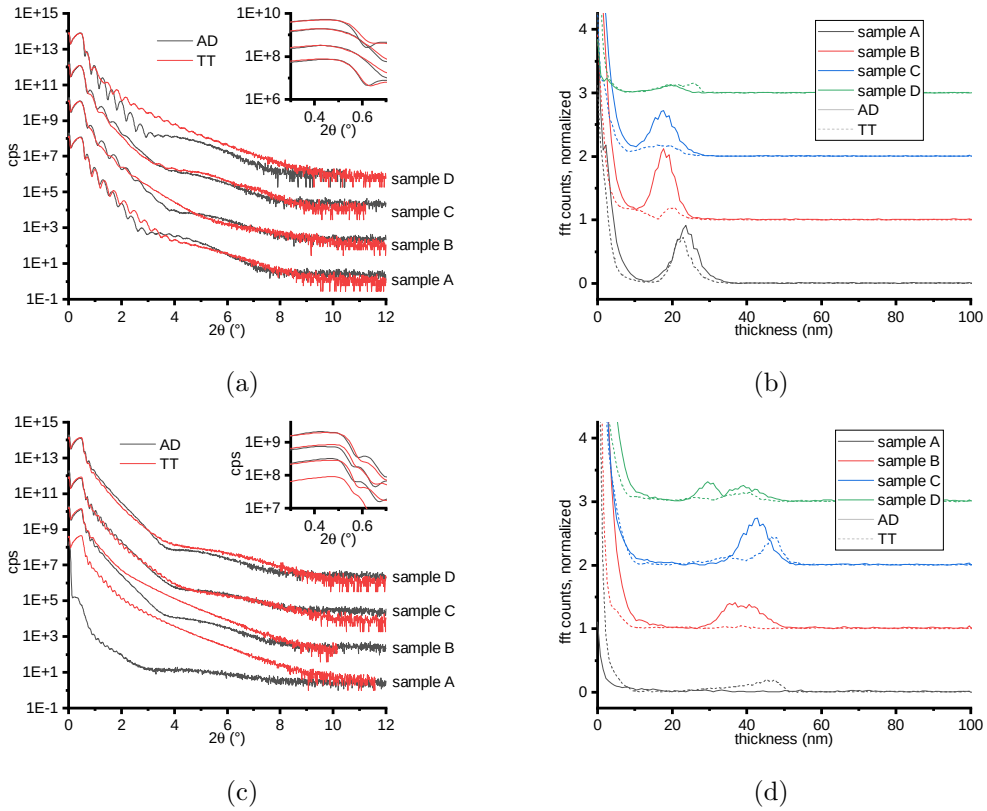

Figure 3.27: The effect of the TT on the films according to XRR measurements on films sputtered for 10 minutes ((a) and (b)) and 20 minutes ((c) and (d)). Both the raw data ((a) and (c)) and their FFT ((b) and (d)) are shown.

of such layer into the main one. A more reliable feature is instead present in the FFT graphs, and consists in a generally lower intensity of the peak (that is related to the already mentioned fringes intensity change).

3.2.2.2 Films with varying thickness

The second analysis performed was to check the thickness of the deposited layer. For doing so, many of the samples studied in XRD (section 3.1.4.1) were measured also in XRR. The resulting patterns with the corresponding FFT are presented in Figure 3.28.

The result is quite interesting: the XRR pattern show an increase of the fringes frequency, more or less at the same rate as the deposition duration (i.e. twice the duration, twice the frequency), but in the FFT graph, this rule isn't respected at all. Moreover, in such representation, all the layers with a thickness less than about 10 nm are mixed up, resulting in a quite hard determination of it.

At the end, the thickness obtained from XRR (using different methods to extract

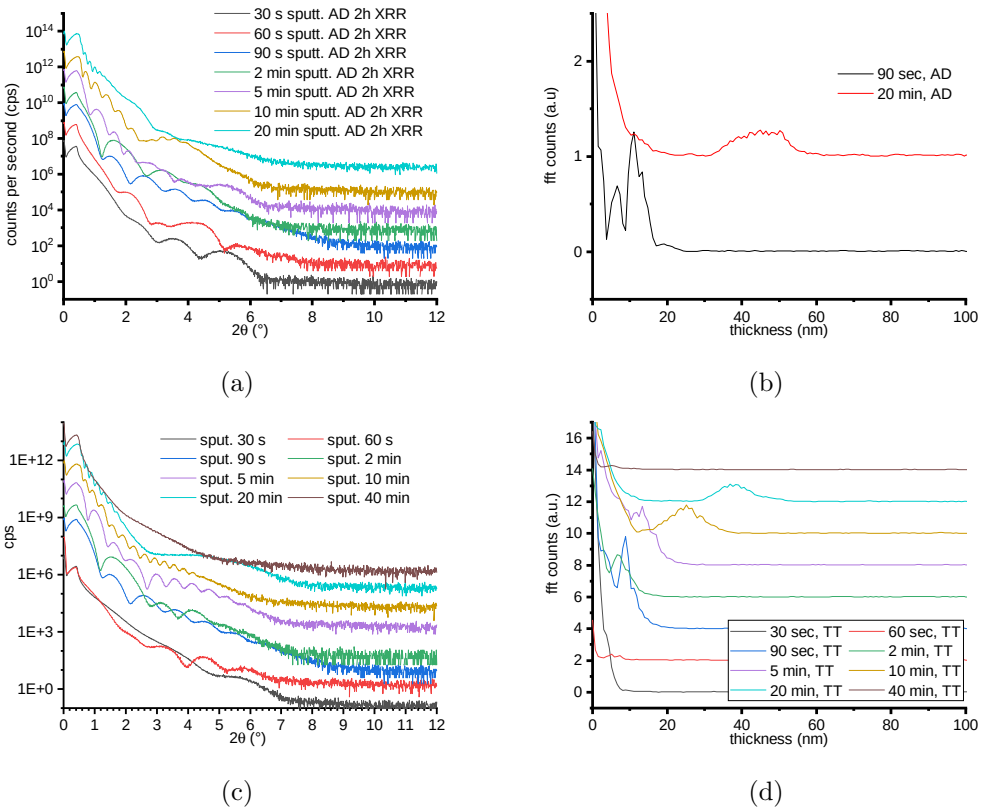

Figure 3.28: The effect of the thickness on the films according to XRR measurements on films (a) AD and (c) TT; (b) and (d) corresponding FFT plots, meaningful only for films with an average thickness.

them) have been compared with the one obtained using a profilometer. The results are reported in Figure 3.29.

3.2.2.3 Multi-layered films

The thinner version of the films prepared for SAXS measurements (see section 3.3 for more details regarding their preparation) had a total thickness compatible with this analysis, so I measure them to complete the investigation about films deposited using multiple runs (necessary for thicker films). As it can be seen in Figure 3.30a and (b) when the deposition is done using multiple runs ("5x60 min, AD" sample, blue line) the pattern is quite complex.

Some features are common to the other AD film (black line), and such features are more evident in q-space (Figure 3.30b): a very short periodicity (less than 1Å^{-1}) multiplied by a larger one (about 2nm^{-1}). The TT films instead appear very different: the one deposited in a single run (red line) keeps the short order periodicity, while the one deposited with multiple cycles has a different one (about 0.5nm^{-1}); the long

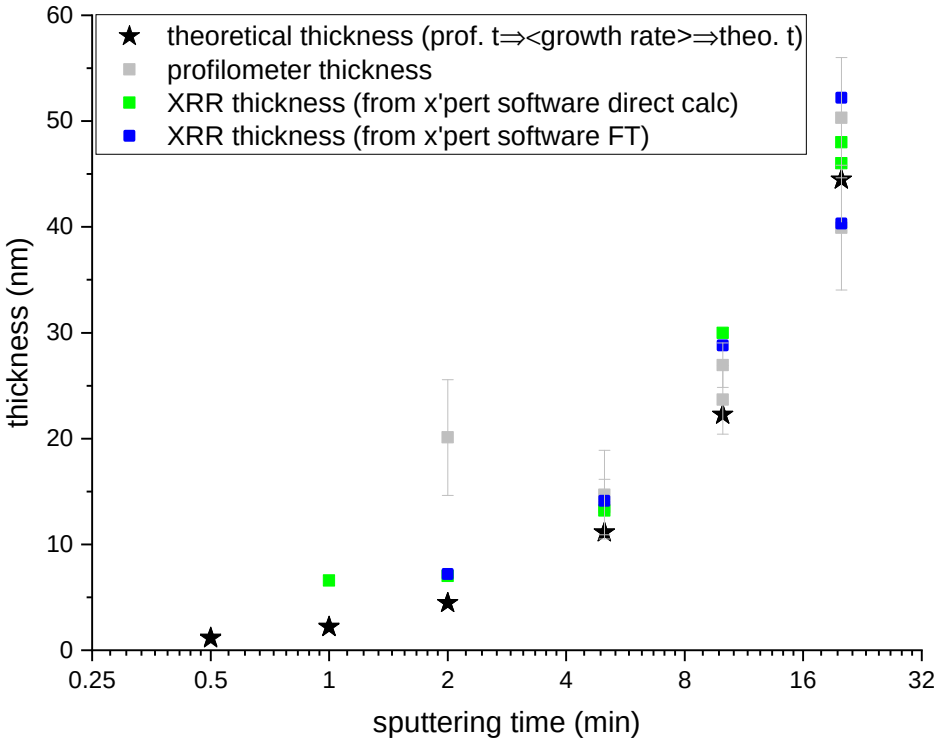

Figure 3.29: Confrontation of the thickness determined using different methods. For what concern the XRR points, the starting pattern was the same for all the methods.

range periodicity is lost, meaning that the corresponding layer disappeared.
All of this observations are reflected in real space: the two samples deposited in a single run show the same thickness (70nm, from the short periodicity), while the 2 AD samples have a common peak at around 3 nm (that can be confused with the fictitious 0-order growth). The complex pattern of the AD sample deposited with multiple runs results in a series of peaks/thicknesses equispaced (see labels). Finally, the FFT of the multi layered TT film is almost completely flat, except for some features at about 10nm, corresponding to the observed periodicity. Quite interesting, this value is very different from the expected one, suggesting the fact that something else is being observed instead of the thickness of the whole deposition.
A possible reason is that for each of the intentionally deposited layer, a second one forms. This second layer appears to be very thin and quite difficult to evaluate. The most plausible explanation for the existence of this second layer is that, due to the RF-sputtering apparatus (especially the lack of a physical barrier between the active and the rest positions) and the deposition protocol used (see section 2.0), some spurious atoms can deposit also during the warming up/stabilization of the plasma.

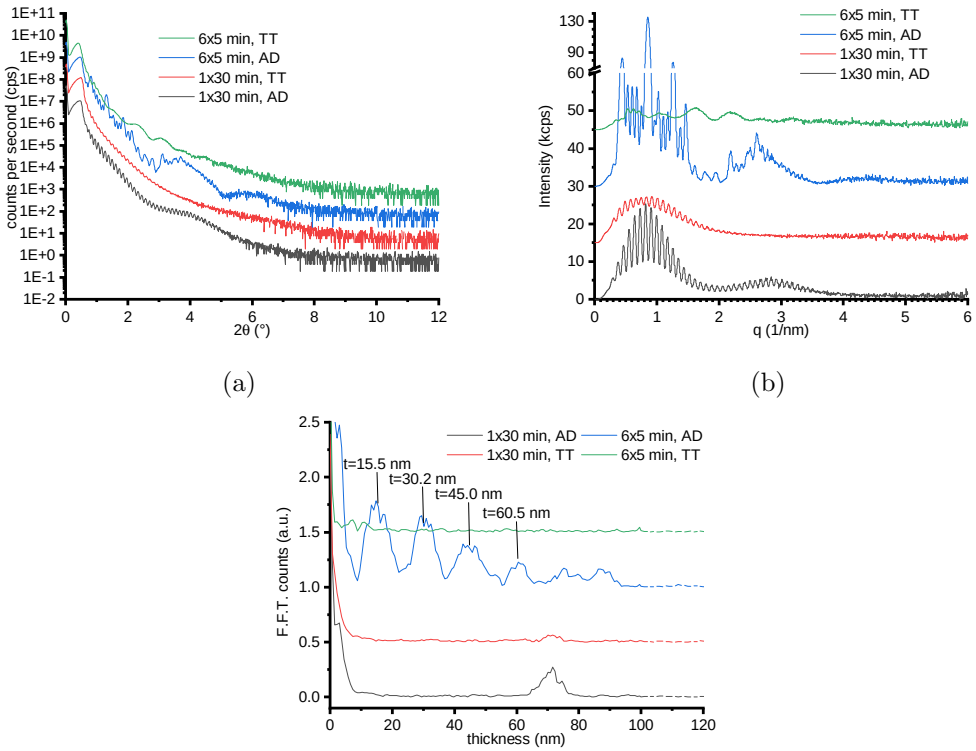

Figure 3.30: XRR ddata collected on the thinner GISAXS samples (with expected thickness around 70 nm). Data presented in: (a) 2θ-space, (b) q-space and (c) real-space (FFT).

During such time, the substrate is not placed directly under the target, but in a near (about 20cm far) position. In theory, the plasma (together with the depositing material) should not extend so far in space, but in practice there isn't any physical barrier in between, and the plasma field strength should follow a decay rate proper of electromagnetic waves ($\propto 1/d^2$). In this case one should expect very few particles to reach the substrate, resulting in a very irregular layer, and this is exactly what quantitative results suggest (Figure 3.32a).

3.2.3 Quantitative results

As already stated, two software packages have been used to quantify the XRR data. The first (X'Pert Reflectivity from Panalytical) requires a modellization of the sample structure, while the second (StochFit) does not.

3.2.3.1 Model-free quantification

The results of this kind of quantification is a profile of the electron density in the sample measured along the direction perpendicular to the surface. Unfortunately, multiple profiles can explain the same resulting XRR pattern. Anyway, for its property of being model free, this quantification can be used to guess input of other fitting softwares.

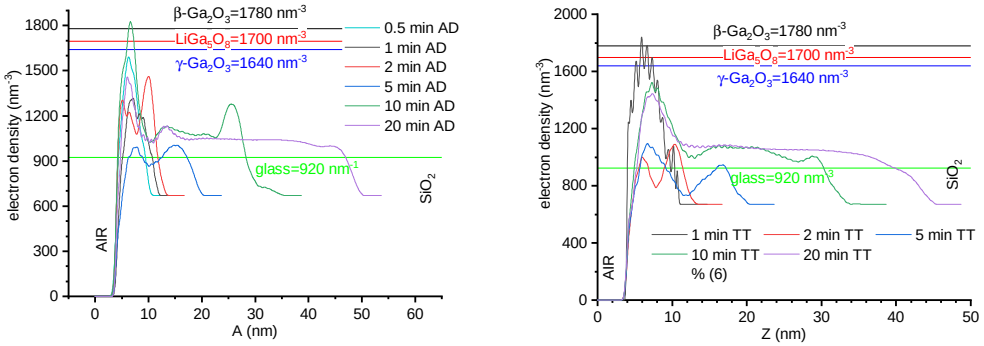

(a) (b)

Figure 3.31: Electron density profiles for some AD ((a)) and TT ((b)) samples according to StochFit fits.

When looking at the electron density profiles of the films in Figure 3.31, the common feature between all the plots is an increase in the electron density at the sample surface. According to the estimated mean electron density for the whole glass and the possible crystalline phases (horizontal lines) this should correspond to an increased ratio of some Ga-rich phase, as if the crystallites are preferentially formed on the surface. A second hill in the profile can be often seen at the interface, and this hill height is inversely proportional to the total film thickness. Especially in thinner film, this can indicate that for the formation of such areas, the Ga atoms must diffuse from near locations, depleting the matrix from it and so preventing the formation of other nanoparticles very close to the ones already present. In thicker films these two clipped layer are quite far away each other, so the disorder inside the material can average the electron density, but when the film thickness decrease, the averaging factor is not strong enough, and the nanoparticles pinned to the interfaces deplete the region in-between from the Ga atoms, negleting the averaging factor. In very thin film (d$\leq$2 min) the profile is larger (so the film appear to be thicker) than expected. AD and TT films seems to differentiate each other only in the intensity of these peaks, especially the one near the interface, with the AD film having it more pronounced. These can be a consequence of the diffusion promoted by the high temperature, and if

this is the case, this diffusion promotes the formation of crystallites also in the region far from the boundaries.

3.2.3.2 Quantification though modellization

In this section, I'm reporting the model based fits on a selection of samples.
In Figure 3.32, for example, I tried to understand the layering structure of the samples sputtered for 10 minutes, both before and after the TT.

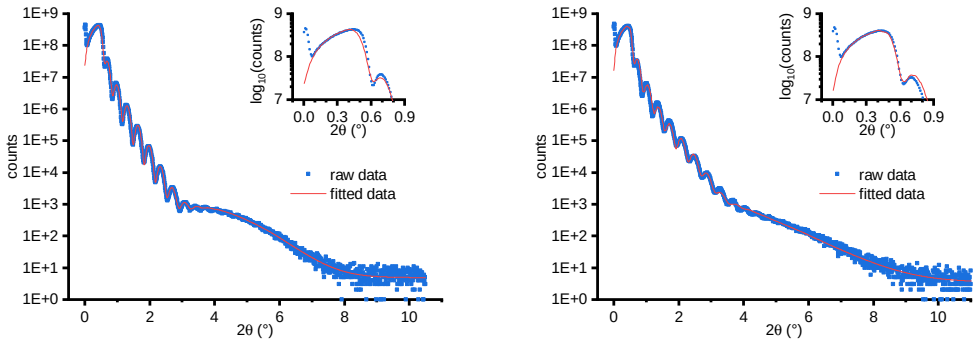

(a) (b)

Figure 3.32: XRR data from samples in Figure 3.27a, together with the best fits. In the inset there are the zoom around the critical angle. (a) sample D, AD; (b) sample A, TT.

The quality of these fits could appear great if one simply look at how well the calculated curves matches the experimental ones, but unfortunately the density of the SiO_2 layer from the substrate resulted in a value lower than the expected (around 2.2 g/cm^3), so the reliability of the results is not really granted.
The optimal fit for the two samples also requires a change in the model, and in particular the low density, atomically thick, glass layer located just above the SiO_2 disappear with the TT, as it was incorporated in the main one, while a new layer, with an higher elecron density, appears on the very top of the structure. Please note that this kind of analysis cannot return any information about the chemical nature (elements and crystal phase) of each layer, but just the average electron density for each position, so the setted composition (Ga_2O_3) and mass density can be completely wrong, but the corresponding electrons density should be correct, and in our case it is higher than the glass phase.
A second interesting pattern is the one collected on the sample measured also in GISAXS (Figure 3.30); here the Fourier transform showed different equispaced peaks. So, this seems to correspond to each deposited run. Anyway, if the deposition is

layer #	comp.	ρ_m [g/cm^3]	ρ_e [1/nm^3]	thickness [nm]	roughness [nm]
3	glass	2.9236	819.27	25.3142	1.3576
2	???	???	107.69	0.1698	0.7834
1	SiO_2	1.2169	365.96	155.008	0.4073
0	Si	2.329	699.26	∞	3.0614

(a)

layer #	comp.	ρ_m [g/cm^3]	ρ_e [1/nm^3]	thickness [nm]	roughness [nm]
3	???	???	708.42	3.4123	1.1331
2	glass	2.9553	828.16	20.0444	0.2784
1	SiO_2	0.5216	156.86	146.1696	1.1837
0	Si	2.5876	776.90	∞	1.055

(b)

Table 3.2: Models and parameters to obtain the fitted curves in Figure 3.32. (a) AD curve and (b) TT curve. "???" refer to layer which nature wasn't understand, so composition/mass density is not provide.

uniform for the whole duration, XRR analysis should not see any interfaces at all, returning a pattern similar to the 1x30min sample. So to obtain a good agreement, each intentionally deposited layer has been alternated by a low density one, as reported previously. The resulting structure has been reported in Table 3.3 and the calculated pattern fits quite well the experimental data (Figure 3.33) especially considering the strong limitations imposed by considering the 6 depositions perfectly equal each other (while is almost impossible as demonstrated in Figure 3.28 with films deposited at the same time).

	layer #	comp.	ρ_m [g/cm^3]	ρ_e [1/nm^3]	thickness [nm]	roughness [nm]
x6	3.b	???	???	1356.31	2.2423	1.4201
	3.a	glass	3.4395	963.84	12.5374	1.8551
	2	???	???	811.12	4.3679	0.1982
	1	SiO_2	1.5952	479.73	155	0.5433
	0	Si	3	900.72	∞	0.6064

Table 3.3: Models and parameters to obtain the fitted curves in Figure 3.33. The first 2 layers (3.a and 3.b) have been repeated alternated for 6 times to obtain the final fit. "???" refer to layer which nature wasn't understand, so composition/mass density is not provide.

After the TT, the pattern of these films just becomes similar to the already reported.

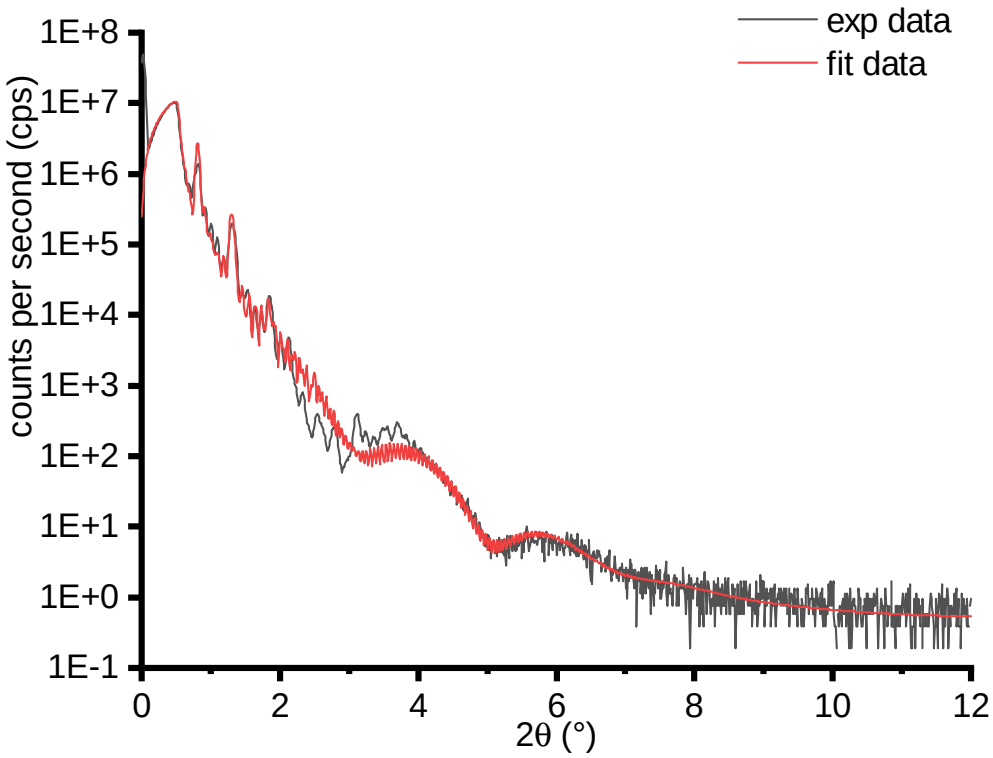

Figure 3.33: XRR pattern and fit from a sample deposited with multiple runs.

3.3 Small Angle X-ray Scattering

3.3.1 SAXS theory

Small Angle X-ray Scattering (SAXS) experiments consist in measuring the scatter effect due to small structures in a sample. "Structures" here mean a region of the sample characterized by an electron density sufficiently different from the surrounding medium. The main limit of this technique is that it cannot really determine if such region is more electron-rich or electron-poor than the matrix.

SAXS data are quite complex to handle because there are many different effects that can occur in such region, and some of them can results in an intensity way larger than the SAXS signal itself. Also the equations behind each effect are not simple, so, for this reason, many different softwares (encouraged by a quite wide comunity working on biological samples) have been developed.

However, a simpler approach is possible if quantitative informations or particle shapes are neglected. In this case is enough to plot some line scans according to some specific representation, the most used of which are:

linear plot: simply the intensity (eventually normalized to the highest or to the measurement duration) versus the reciprocal space coordinate;

Guinier plot is usually used to determine the gyration radius (R_g) of particles; due to the Guinier fit, the data are presented as $\ln(I)$ vs. q^2; this representation should be linear up to q values less than about $1.2/\mathrm{R_{gyration}}$ of the investigated regions;

log-log plot, useful to emphasize behaviour at very small angle/scattering vector q and to extrapolate the data toward q=0, so to obtain the total number of electrons inside the particle;

Porod plot is used to determine the internal specific surface area of the particles, starting from Porod relation $I \propto S \cdot q^{-n}$ (n is a number greater than 2 that depend on the nature of the material to be investigated) and presents the data corrected by the Fresnel decay ($I \cdot q^4$ vs. q); this representation gives better visibility to points situated at large q vectors;

Zimm plot is used as an alternative to the Guinier plot, and can lead to the same informations (I_0 and R_g); the data are presented as $1/I$ vs. q.

An example of the most important plots are presented in 3.34.
The real-space dimension can be retrieved using:

$$|\vec{q}| = \frac{2\pi}{d} \Leftrightarrow d = \frac{2\pi}{|\vec{q}|} \tag{3.20}$$

the previous equation can be derived from 3.4 and the magnitude of the scattering vector:

$$|\vec{q}| = \frac{4\pi \sin\theta}{\lambda} \tag{3.21}$$

Further details can be found in [44].

3.3.2 GISAXS apparatus and experimental procedures

3.3.2.1 Apparatus

SAXS measurements have been performed at the ELETTRA synchrotron facility located in Trieste, IT, using the SAXS ("AustroSAXS") beamline in Grazing Incidence (GISAXS) mode.
The main features of this set-up are:

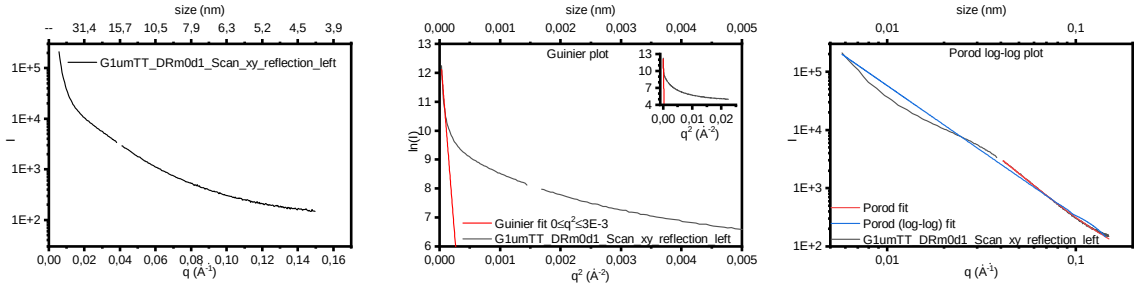

(a) Linear (I vs. q) plot. (b) Guinier (ln(I) vs. q) plot. (c) Log-log plot.

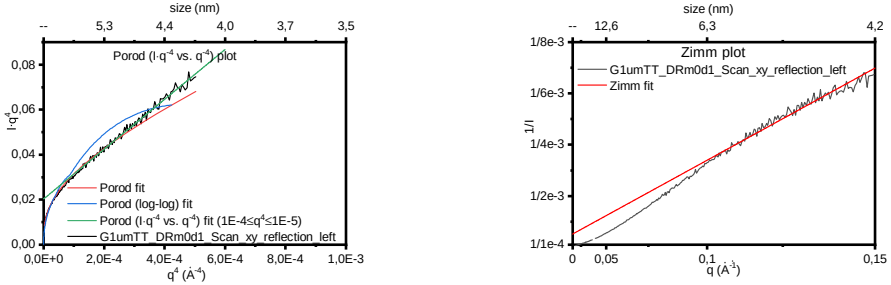

(d) Porod (Iq^4 vs. q) plot. (e) Zimm ($1/I$ vs. q^2) plot.

Figure 3.34: The above figures contain all the same data (nickname of the sample is "1µm good TT", with "good" referring to the relative high optical quality of it, see 3.3.2.2) collected at $\omega = 0.3°$ and along the "q_{xy} reflection left" integrated line scan, see 3.35) but presented according to the most famous representations of SAXS data.

- the incident beam can be collimated using 3 sets of 4 slits each (square spot), so to obtain a very small divergence;
- Sample-Detector Distance (SDD) up to 2.3 m (about 2000 mm in my case), most of which in void (so to reduce air scattering);
- a Pilatus3 1M [45] as main detector for SAXS data together with a Pilatus 100k [46] secondary detector for Wide Angle X-ray Scattering/XRD data;
- a sample stage with 2 motorized axis (the two perpendicular to the beam) and a goniometer (ω);
- three available monocromated wavelengths: 5.4 keV, 8keV (the one used, corresponding to about the wavelength of Cu K_α) and 16keV.

3.3.2.2 Goals and samples

GISAXS measurements have been collected for three main reasons:

1. to confirm that crystalline regions observed in XRD or the hills in AFM images does really have a different electron density (and so a different elemental composition);
2. to have an idea of the size of such regions and confront it to the one observed in bulk [19];
3. to measure the porous size found in the sample obtained through the method described in 2.3

To do so, eight films and the bulk material were tested. The eight films are all the possible combination regarding the following dual characteristics:

thickness either about 1µm (10 depositions of 1 hour each) or 100nm (a total deposition length of 60 minutes, either in one shoot or in 4 runs of 15 minutes each);

thermal treatment either AD or TT samples;

optical quality either optically "bad" (with pores) or "good" (without pores); the "good" films have been prepared with a single deposition (thinner films), or if it wasn't possible (thick films), by annealing the sample at 600°C for a night between each deposition; instead, the "bad" samples were prepared by multiple deposition without removing the sample from the deposition chamber.

For more details about the preparation, please see 2.0. The raw data have been collected on all the prepared samples (the bulk was also measured in transmission mode and not only in grazing incidence), however the data of the thick, TT, optically bad sample produce a too diffuse signal, and it was impossible to recognise the main features (the reflected beam and the Yoneda peak) in the resulting image, and thus was impossible to evaluate properly.

3.3.2.3 Data treatment

The raw output from the beamline is just an image from the Pilatus detector in real space. Again, as in 3.1.3, I converted them at least in the reciprocal (q) space using the software GIDVis [33].
In opposition to the GIXRD experiment, here the q_{xy} and q_z direction are not equivalent since there is some anisotropy. In fact, I'm dealing with low dimensionality samples (thin films), so some confinement along the Z axis (the film thickness itself at least) that we don't have in the plane is expected. So, to further proceed in the analysis, 6 Region of Interests (RoIs) corresponding to the white rectangles in 3.35 have been selected/extracted from each map. Of these, the q_xy_near and q_z_near regions always lay as close as possible to the dark area in the images (corresponding to the sample and the vertical beamstopper) while the q_xy_reflection position must be changed in every image so that it is always just above the main reflection from the film.
Over these regions, integrated line scans were calculated (the integration length, corresponding to the shorter side of the rectangles, was 3E-3$\dot{A}^{-1}$) so to extract 1D datasets to be visualized and elaborated. Concerning the q_z scans, the axis origin was set on the Yoneda peak (Y line in Figure 3.35). This is due to the fact that informations coming from the inside of the sample appears at this position (critical angle). Of course, since the Yoneda peaks should appear at the outgoing critical angle that depends also on the tilt of the sample, this position must be calculated for each investigated picture.
Fitting such data was more difficult than expected: dedicated software for 2D SAXS analysis are few, often not accessible (as FitGISAXS [47] that require the licensed IgorPro software to be executed), not so straightforward to use (as IsGISAXS [48]) or they do not grant enough degrees of freedom to correctly model my material (as BornAgain [49], in which there is no possibility to set a random distribution along x, y and z of particles with size r also randomly generated; without such distribution the simulation/fit was completely inaccurate). On the opposite, trying to fit the data

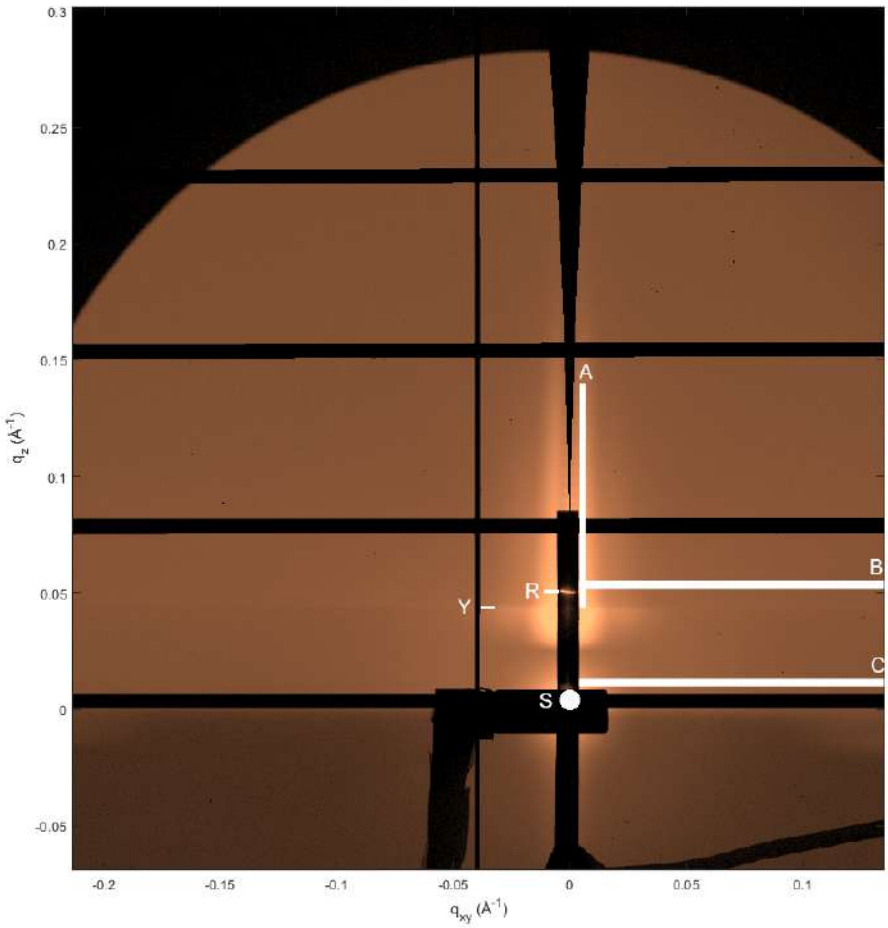

Figure 3.35: An image taken from a sample (100 nm good AD) with drawings about important elements. S is the spot where the direct beam hit the detector (origin of the q space), R is the main optical reflection of the primary beam from the film (so intense that must be hide from a thin layer of metal, but is still the brighter point on the detector) and Y is the position of the Yoneda Peak. A, B and C are the RoIs where I extracted the data show in the next sections. A is denoted as q_z_near_right, B as q_xy_reflection_right and C as q_xy_near_right. Other 3 regions, mirrored respect to the vertical beamstopper, were also measured at q_xy < 0, but otherwise in the exact position/size, and have been called _left.

with general softwares (i.e. origin Pro) with custom made functions following the most used law (Guinier, Porod and Zimm) lead to either very poor fit ($R^2 \leq 0.70$) or with physically unacceptable parameters (assuming sphere particles, their radius was less than 1 Å or more than the film thickness in the Z coordinate, without results in between). Another problem, especially for what concerns the Guinier law, was the small region where these approximation apply, which require that

$$|q| \cdot R \lesssim 1.2 \tag{3.22}$$

that in my case ($R \approx 10\text{nm} = 100\dot{\text{A}}$) correspond to q values up to $0.01\dot{\text{A}}^{-1}$, about 6 data points/pixels.
however, in general, raw data were good enough: proper visualization and/or very basic elaboration (converting q values to real space values with eventually the use of a Fourier Transformation) already gives satisfactory results. For this reason, only pseudo-quantitative results will be presented.

3.3.3 Results

After being extracted from the intensity map, the SAXS linescans appear as in Figure 3.36a. q_z and q_{xy} scans are very different each other, but they do not vary too much between the half left and half right q space. They still have some differences, mainly the intensity. These differences depend on many factors, including the fact that the scans have been collected not really in a symmetrical way due to the bad centering of the beam stopper. q_{xy} scans are almost correct and really show the SAXS informations (peaks) we are interested in. On the opposite, q_z scans show (at least in this case) two peaks: one, narrow and symmetric, that is the reflected beam that wasn't fully covered by the beam stopper (in this case it's at 0.05 $\dot{\text{A}}^{-1}$), while the other, wider and asymmetrics is the so-called Yoneda peak [50] (in this case it's at 0.043 $\dot{\text{A}}^{-1}$). As already stated, the photons coming from the inside of the sample start to hit the detector in this position, and thus this should be our real origin of the q-space. The order in which the Yoneda peak and the reflection (if present) appear on these plots depends on the incident angle used (the reflected beam is tilted twice as much respect to the incoming beam, while the Yoneda peak is shifted by the critical angle from the sample surface direction, and the latter is basically the incident angle itself). After the proper corrections, what we obtained was the Figure 3.36b plot.
To check the quality of this correction we compare the results of the scans acquired on the bulk in grazing-incidence and in transmission mode. The latter, only applicable to sample macroscopic in the directions perpendicular to the beam, and thin in the other (that mean the opposite of the films geometries), has the advantage that the incident angle is known (0 by definition) and that the origin of the q space is exactly where the primary beam hits the detector (no Yoneda peaks involved). In Figure 3.37, this comparison is reported.
Of course the bulk should be isotropic, and this is reflected in the fact that the two curves taken in transmission (red lines) show two features more or less at the same q positions (0.02 and 0.05 $\dot{\text{A}}^{-1}$). In the scans collected in grazing incidence mode these features disappear and a new one, located more or less in the middle, appears. This

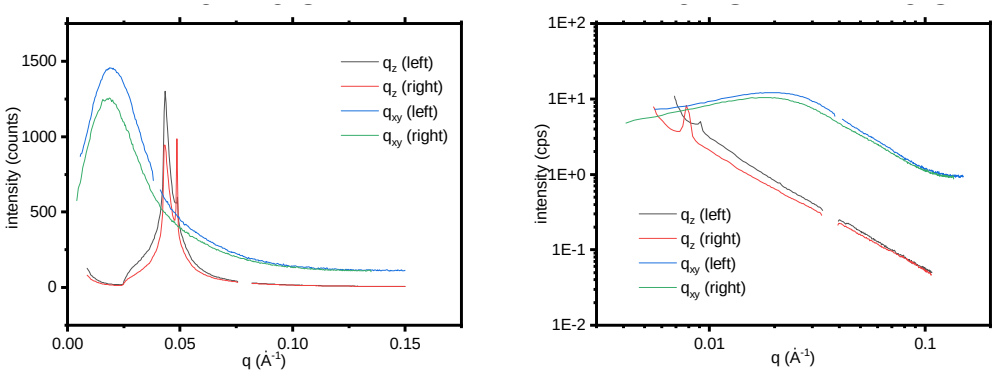

(a) (b)

Figure 3.36: SAXS linescans from the sample deposited in a single run of 60 minutes and then treated. (a) the intensities as exported from the q map and (b) after being corrected for the Yoneda peak position and the lateral distance from the q-space origin.

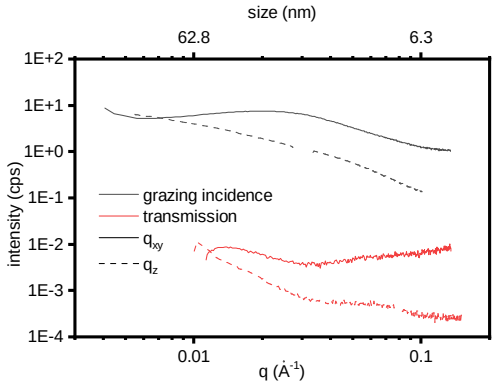

Figure 3.37: SAXS linescans from the bulk sample. Only the right scans are presented since the sample itself shade half the detector.

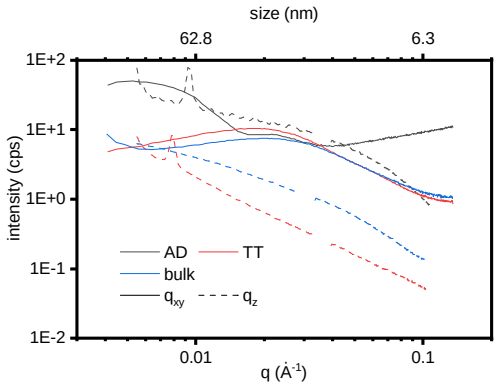

Figure 3.38: SAXS linescans from the bulk and from the films deposited in one run of 60 minutes.

implies that the calculated q values are wrong in at least one method, so they are not reliable. However they indeed hint at a presence of features both in the in-plane and in the out-of-plane directions occurring at the same position (about 0.03Å^{-1}), so they appear to be subjected to the same shift. For this reason, I'm going to use the GI measurement of the bulk as reference in the next plots.

The first thing we were interested in, was the evaluation of the TT samples. I'm doing this in Figure 3.38. According to these data, the lateral size of the NPs in the films is similar to the ones observed in the bulk. The same size is observed in both the AD and in the TT samples, so the annealing doesn't seems to change the Ga-rich regions. The AD sample also shows way larger ($\approx$ 100nm) features, probably the large islands observed at the AFM (section 5.1.3).

Concerning the out-of-plane direction, we observed a quite important change during the annealing. In fact, patterns of AD samples are very similar to the (TT) bulk with a single broad shoulder corresponding to features of about 20 nm, but after the annealing this shoulder disappear completely.

The next parameter we evaluated was the effect of films thickness (good optical quality). Data are summarized in Figure 3.39a. Before the annealing, the thicker film ($\approx$1 µm) seems very similar to the thinner ones ($\approx$130 nm), both in the in-plane and in the out-of-plane directions. However this changes significantly with the TT: in the xy direction we observed a shift to higher q (small real sizes) of the peak, while in z direction we didn't noticed any major change.

The last investigation we did using SAXS data was about the differences in films which have different optical qualities. In Figure 3.39b the data collected on the thinner films are reported. The signal in general appears very weak, so weak that especially in the

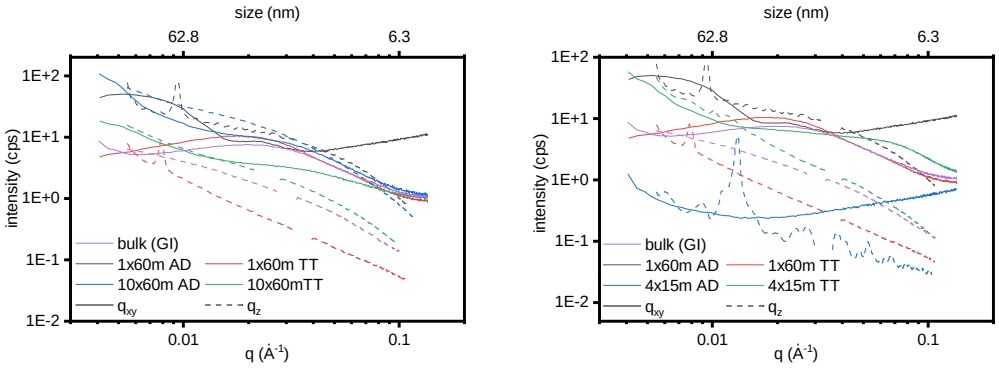

(a) (b)

Figure 3.39: SAXS linescans from samples (a) deposited for different total times but that posses an high optical quality and (b) from sample deposited for a total time of 60 minutes, but both in a single run or in 4 runs of 15 minutes each.

xy direction we could only observe an excess of the Lorentz correction (the raising of the high q tail; see GIDVis [33] manual for an explanation of the correction). In the out-of-plane direction we instead observed a pattern similar to the XRR observed on similar samples (section 3.2.2.3), but no informations about any possible NP presents in the film.

As suggested in section 2.3 the TT have the effect to improve the films, also from the point of view of the NPs size and concentrations. In particular, thanks to the annealing, we retrieve the out-of-plane shoulder at 0.07 $\dot{A}^{-1}$. Also the xy peak returns, but in a different (higher q) position.

3.4 X-Ray results

The used x-ray-based techniques, combined together, give a picture of the inside of the films: especially after the TT, they appear as many Ga-rich NCs embedded in an amorphous matrix. The nanocrystals show a distributions in size (around 3.5 nm according to diffraction experiments). These NCs also appear to be groupped in clusters about 50 by 200 nm (h by ∅, according to scattering experiments). Electron density profiles (obtained trough XRR) suggest a non uniform distribution of them in the out-of-plane direction of the films, with an higher concentration near the film boundaries (in primis the surface).

Chapter 4

Optical characterization

The following techniques have been used for optical characterization of the sample:

Imaging using an optical microscope (an Olympus BX40);

UV-VIS absorption using a Variant Cary 50;

µ-FTIR, using a Thermo Fisher scientific nicolet iN10 in reflectivity mode;

Raman shift, using a system based on the BX40 microscope and the Jobin – Yvon model Labram optics;

refractive index measurements using a Metricon 2010 prism refractometer.

The quality of most the data of this chapter resulted to be poor (especially FTIR and raman shifts), so they have been considered as just failed attempts, and the theory behind them wasn't studied deeply and thus will not be reported in this document.

4.1 Imaging

The films deposited on silicon have a metal-like aspect (see for example Figure 4.1a), which includes nice reflections and an overall color that is very sensible to the film thickness. Occasionally, especially for the thicker films (including the one obtained alternating a deposition with a night in the oven), some area of the films surface appear a bit foggy.
On the opposite, films deposited on transparent substrates (i.e fused silica), before the TT, are completely transparent (Figure 4.1b) and differ from the substrate only by a slightly different refractive index, which led to a different critical angle for the external total reflection that is the main way to check the film position.
If the film has been obtained in a "good way", with a single deposition or multiple

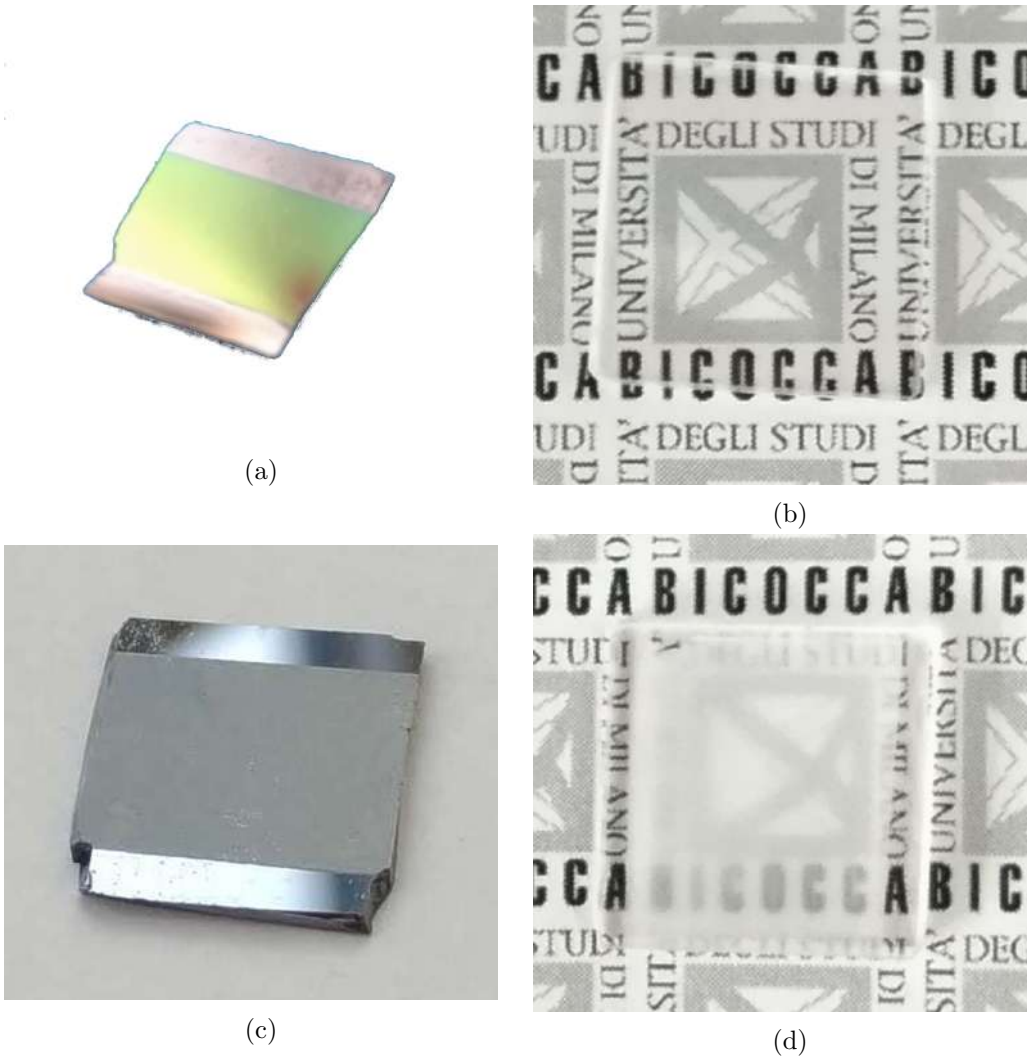

(a) (b) (c) (d)

Figure 4.1: Optical images of films taken with a normal camera: example of the aspect of the films deposited (4.1a,4.1c) on silicon and (4.1b, 4.1d) on fused silica of (4.1a, 4.1b) AD films and (4.1c, 4.1d) multiple-deposited TT films (single deposited ones look similar to AD ones).

depositions alternated by the pre-annealing treatment described in section 2.3, the optical quality doesn't change so much during the TT: only sometimes the foggy regions already described become larger, but no other differences can be observed.
On the opposite, in the case of films obtained in multiple deposition without any proper treatment between them, after the TT they become grainy, loose any reflection and turn grey/white (Figure 4.1c and in Figure 4.1d). We attribute this change to diffuse scattering.
Looking at the optical microscope images reported in Figure 2.2, this hypothesis finds a confirmation with the presence of structures which density increases with increasing

TT temperatures.

4.2 UV-VIS absorption

These measurements (200-1100 nm) have been performed on films growth on SiO_2 (fused silica) substrates in 4 depositions of 60 minutes each. The main experiment performed with this technique was to test the formation of the γ-Ga_2O_3 inside the films by looking at the appearance of its typical absorption band at around 5 eV (about 250 nm), but unfortunately the observed effect was the film internal reflection in accordance to its thickness (Figure 4.2) that hide the possible shift in the absorption edge in the samples treated at higher temperatures, making this test at least dubious.

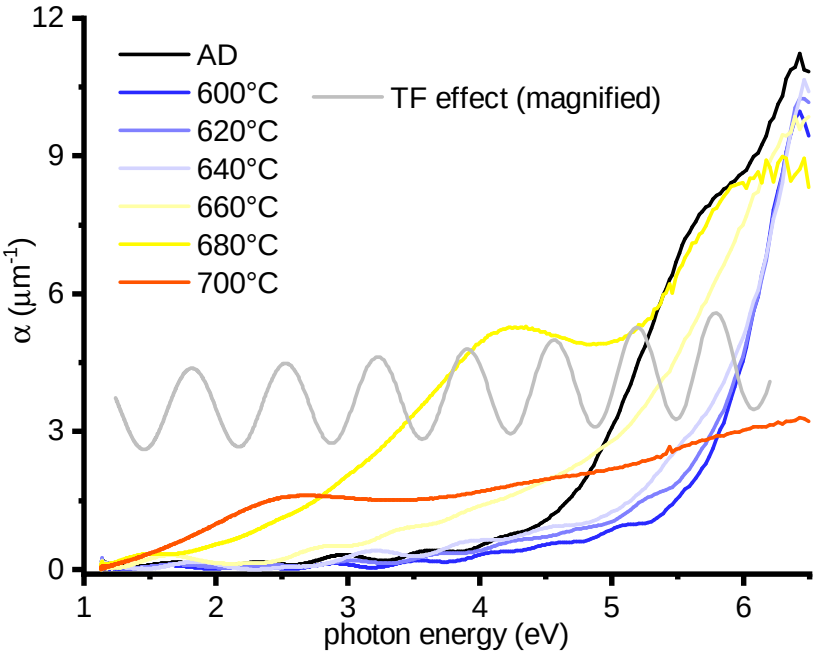

Figure 4.2: Absorption coefficients of films treated at different temperatures. Gray curve is a scaled simulation of the absorption of a SiO_2 film with the same thickness of the AD film. The absorption coefficient has been calculate from transmission spectra, ignoring other effects.

As it can be seen, the simulated spectra has maxima and minima at the same position of the AD film, in accordance with a simulation[51] of a film with thickness 520 nm (corresponding to the theoretical thickness of the measured films) and a refractive index of 1.6433. Annealing the film at high temperatures changes the film thickness (as already show in Figure 2.2h), resulting in more separated ripples.

However also the effect we were looking for can be seen: the absorption band present in the AD film at the beginning disappears, but over 650°C it moves again towards lower energies till 700°C, when the absorption is almost flat for all the photons with energy greater than 2.5 eV (500 nm), and indeed the sample appears brownish.

4.3 Refractive index

Refractive index measure has been carried out using a Metricon 2010 prism coupler refractometer, an instrument that can measure the refractive index of a material (either a film or a bulk) by coupling it with a prism with higher refractive index, using a laser (a He-Ne operating at 633nm) and then measuring the critical angle(s) that occur in the system. In the case of the bulk, only one critical angle can be seen, and it corresponds to the internal total reflection of the Snell law. Instead, in the films, more critical angles appear due to destruction interference between a light beam that bounce on the external surface of the film and a second one that travels through the film, is reflected at the substrate and exits again the film. In this second case, both the thickness and the refractive index of the film influence the difference in the beam paths and so the critical angles positions. At least two destructive interferences must be observed for a complete characterization of the film; with just one, either the refractive index or the film thickness must be measured in a different way.
Multi-layered films have been measured, and even with such samples, the extinction were weaken and usually just one was observed, so the thickness from the profilometer had been used. The films appear to have a refractive index (n_{AD}=1.8052 and n_{TT}=1.8035) higher respect to the bulk (n_{AQ}=1.627 and n_{TT}=1.635) but closer to the calculated values[20].

4.4 Other techniques

In this section I'm reporting the results from other techniques (Fourier transformed infra-red, Raman and x-ray photoelectrons spectroscopies) which have been performed on my samples, but that give very poor results, both in term of quality and validity.

4.4.1 FTIR

During a FTIR measurement, the resonance frequency of the vibrations modes between the atoms are probed.

The instrument used can collect spectra between 400 e 4000 cm^{-1}, but below 800cm^{-1} the detector efficiency become very low, resulting in lower signal-to-noise ratio and resolution power in such region.
IR reflection spectra have been collected on the same samples used for the UV-Vis measurements. The normalized spectra can be seen in Figure 4.3.

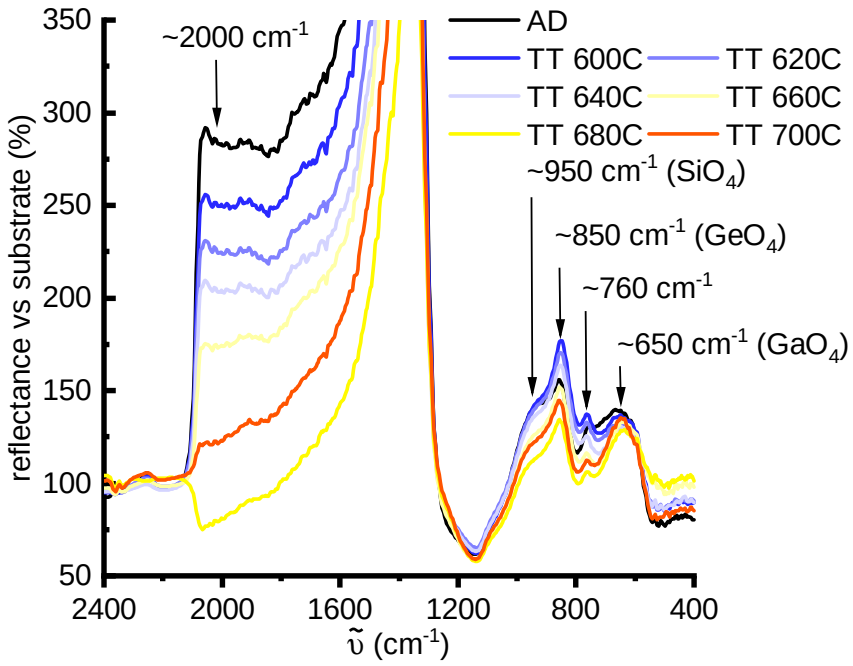

Figure 4.3: Fourier Transform InfraRed (FTIR) spectra collected on samples treated at different temperatures.

On these spectra, some features can be observed (marked with arrow and labelled), but an unequivocal interpretation is not given due to a couple of problems (the signal seems somehow vertically shifted in a rigid way and the 680°C curve seems to be outside the serie).

4.4.2 Raman

A Raman measurement is often seen as a complementary method respect to the FTIR due to the different vibrational modes that can be observed with the two techniques. Unfortunately, with our equipment, the penetration depth of the analysis is few µm, resulting in the analysis of the Si substrates instead of the films (even for the ones deposited with multiple cycles, that should be over 1µm in thickness) as it can be seen in Figure 4.4, so no useful information has been collected in this way.

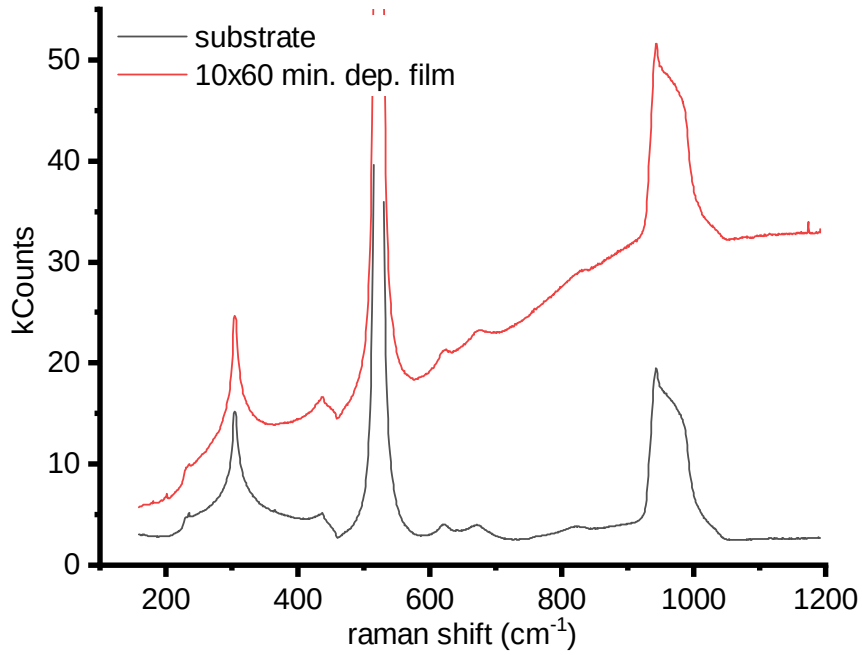

Figure 4.4: Raman spectra collected on the bare substrate and on a film.

4.4.3 XPS

Investigation made in collaboration with **Prof. G. Koller** group from **Universität Graz**.

The XPS is a surface elemental analysis technique, with also the capability to measure different electron shells, thus providing some knowledge about the electronic state of the probed atom, allowing one to have some insights about which atoms it is bonded to.

Apart from a general confirmation of the oxides really present in the films (and an estimation of their respective ratios), the main goal of this kind of experiments was to understand what was the nature of the bubbles observed on films TT after being deposited with multiple runs, and observed using microscopes (both electronic, Figure 5.12, and optical, Figure 2.2).

For such purpose, 4 films with a total deposition time of 30 minutes were prepared: 2 of them using a single deposition session, while the other 2 by 6 depositions of 5 minutes each. One sample of each kind was then TT at 700°C for 30 minutes.

The XPS survey scan (binding energy from 0 eV to 1100 eV) of them are reported in Figure 4.5. Some samples were excited with both Al and Mg radiation, while the multi layered AD were excited only with Mg radiation.

Qualitatively, the only difference seems to be the peaks of the multi layered AD

sample situated between 800 and 600 eV (binding energy from Mg excitation)/1200 and 1100 eV (binding energy from Al excitation), however the origin of these peaks is still unknown since they do not coincide neither in binding energy (XPS signal) neither in kinetic energy (Auger signal).

No high resolution scans have been acquired on any peak due to the high complexity

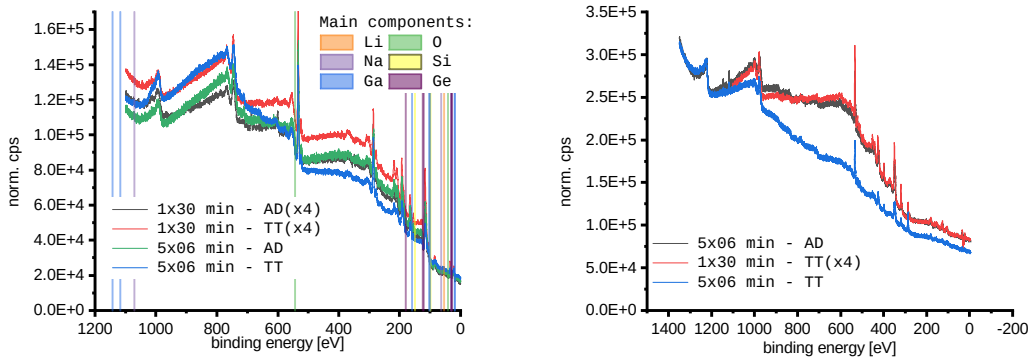

(a) (b)

Figure 4.5: Survey XPS scans on the samples prepared to investigate the effect of multiple deposition excited by (a) Mg K_α radiation (1253.6 eV) and (b) Al K_α radiation (1486.61 eV).

of the spectra who forbid us to fully understand and label all the signals and thus differentiate between different excitation state.

Chapter 5

Surface morphology characterization

5.1 AFM

Investigation made in collaboration with **Prof. A. Sassella** group.

5.1.1 AFM theory

Atomic Force Microscope (AFM) allows a non destructive characterization in which the surface of samples is probed to get 3D morphology informations from it.
The data are acquired by scanning the surface with a very thin tip and collecting its height and the force needed to keep it in such position, usually with a cantilever (force) coupled with a laser and a detector (height). A diagram explaining this can be found in Figure 5.1.
The historically first two measurement methods were the constant height (so only the force were actually measured) and its counterpart, the constant force (height is measured) methods, but nowadays a third method is usually used, one that involve the oscillation of the tip at a certain frequency. The method used in this work is the latest, and has two main advantages:

1. is more reliable and accurate;

2. due to the fact that the probing (the tip height) and collected (the force) signal evolve in time with a given periodicity, we can define a phase shift in time between them, and this shift can be related also to the material phases present at the surface of the sample;

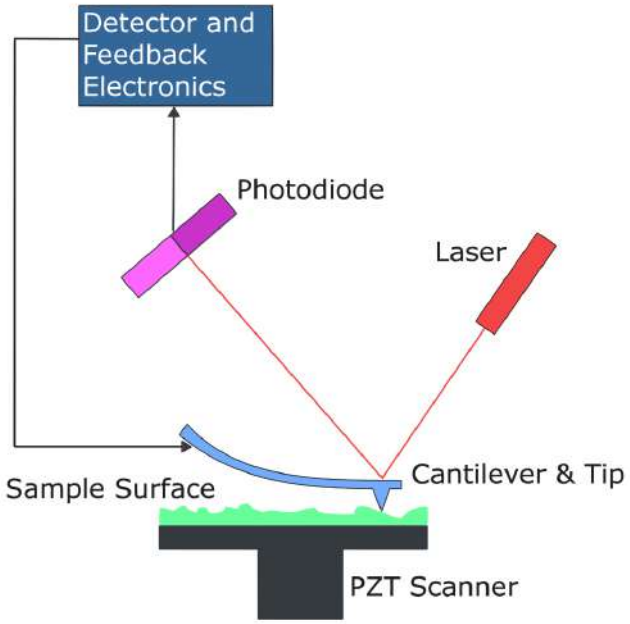

Figure 5.1: Diagram with the principal components of an AFM instrument (from Wikipedia).

Here I will usually present only the height data because the maps described in the second point strongly depends on the height of the sample itself, so different stiffness cannot be assigned with enough certainty.
All the following data have been acquired using a Nanoscope V Multimode AFM Bruker instrument in tapping mode, in air, with silicon tips at a resonance frequency of about 340 kHz, spring constant 40 N/m, and tip radius 8 nm. The elaboration of the data/maps have been performed using either the instrument vendor, specific open surce (Gwyddion[52]) and/or general (ImageJ, Origin Pro,...) softwares.

5.1.2 AFM vs. simulation

The first experiment we performed was a comparison between the surface of AD and TT films. To have additional information about the uniformity of both processes along the thickness, we etched the film using a diluted solution of HCl (about 1e-4M) for 5 minutes at 37°C. These conditions have been found to be optimal to selectively etch the matrix of the films while leaving the Ga-rich regions intact. The images taken from these 4 samples (AD full, TT full, AD etched and TT etched) can be found in Figure 5.2.
These images have been analysed so to obtain a distribution of the NPs radii by automatically identifying them. Such distributions have been reported in Figure 5.3.

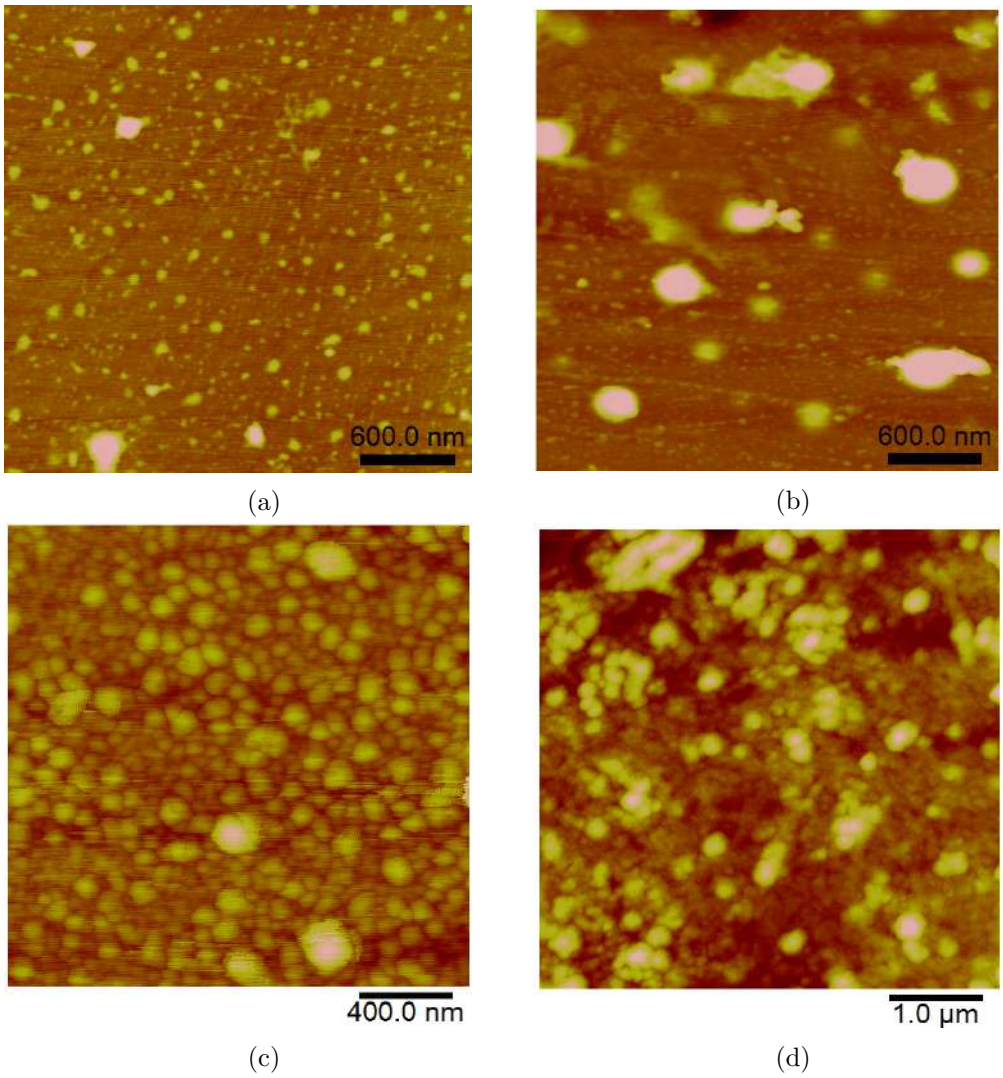

(a) (b) (c) (d)

Figure 5.2: AFM height map collected on AD ((a) and (c)) and TT ((b) and (d)) samples, either as-is ((a) and (b)) or after been etched ((c) and (d)) so to obtain informations also on the inside of the films.

In order to better understand the kinetic behind the NPs formation, these experimental distributions have been compared with some simulated ones.
This simulation consists in filling a parallelepiped (representing the film) with ellipsoids with shorter out-of-plane radius (representing the NPs we observed in the AFM images) like in Figure 5.4a and then cutting the structure at different height, so to simulate the etching. A top view of the system is then collected (Figure 5.4b) and from such view the structures that emerged from the matrix were detected and their radius measured (Figure 5.4c). The size distributions obtained with such simulations (averaged over many possible configurations so to avoid special cases) have then be

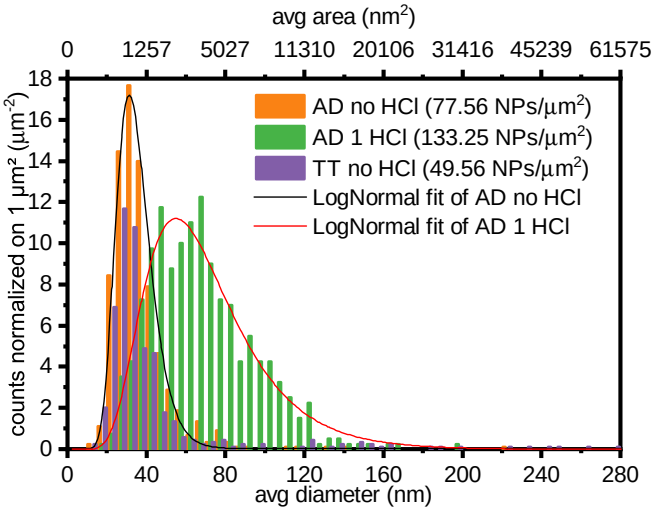

Figure 5.3: The number of particles observed on 1 µm divided by size obtained by the analysis of 3 samples (bars). Such distributions can be fitted quite well by log-normal distributions (line).

compared with the experimental one (Figure 5.4d).

The same theoretical experiment have been repeated varying the parameters used to create the original distribution of NPs (size and number, plus their distribution also accounting for a not homogeneous distribution along the thickness). The scenario that best matched the experimental data have been reported in Figure 5.4d and among many parameters, two are quite importants: this simulation tell us that there are around 560 NP/µm^2 (distributed not uniformely along the film height and thus a volume density cannot be given) and that the growth of the NPs follows a third degree Avrami[53, 54, 55] law. The degree of this law indicate how many dimensions grow rapidly (relative to the others). These dimensions can be any perpendicular physical directions (i.e. x, y and z) and/or the formation of new centres. Probably, in our case, we have the the formation of new centers and the growing in the in-plane directions, while the growing in the out-of-plane is slower.

5.1.3 AFM vs. film thickness

Another interesting investigation we performed was to look at very thin samples (also with a predicted thickness of around 1 nm) at the AFM. So thin samples are representative of the real shape of the NPs since probably the matrix cannot reach the half height of them (according to XRD the crystallites in them should be at least 3 nm in diameter).

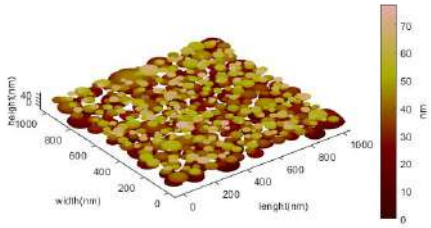

(a)

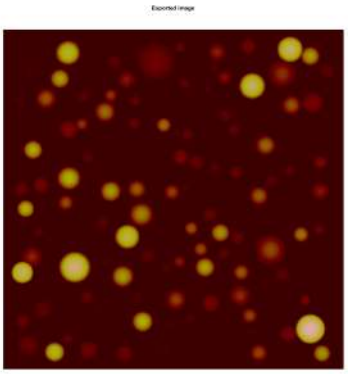

(b)

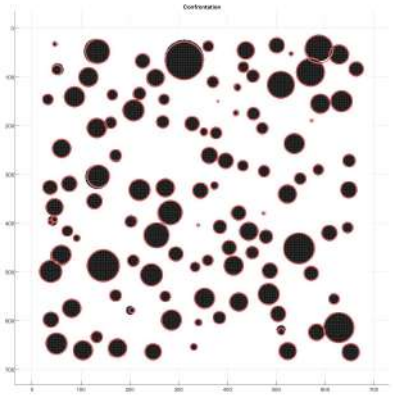

(c)

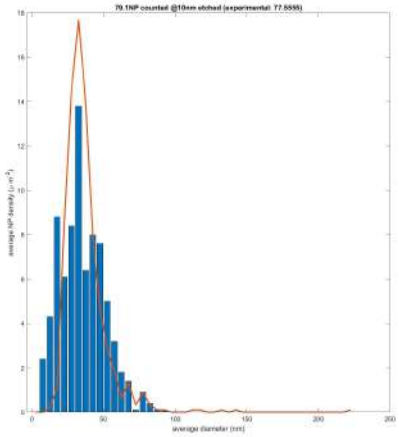

(d)

Figure 5.4: The main steps involved in the study of the NPs formation using morphology simulations. (a) The 3D structure constructed to resemble the film; (b) a top-view of such structure; further steps always originate from the studying of such images, so to try to keep the same systematic errors as the experimental studies; (c) each circle represent each detected and measured NP inside the previous image; (d) the NPs detected in the previous step have been divided according to their dimension and then counted; the obtained distribution (bars) have been confronted with the experimental data (line).

In Figure 5.5 there are the height maps taken from AD samples. Different thickness of the films correspond to completely different morphology. We also look at the phase map, reported in Figure 5.6. When compared with the height map in Figure 5.5a, we identified the visible terraces as those regions where the film was already growth (higher plateau) and other regions where just the substrate was present (lower plateau).

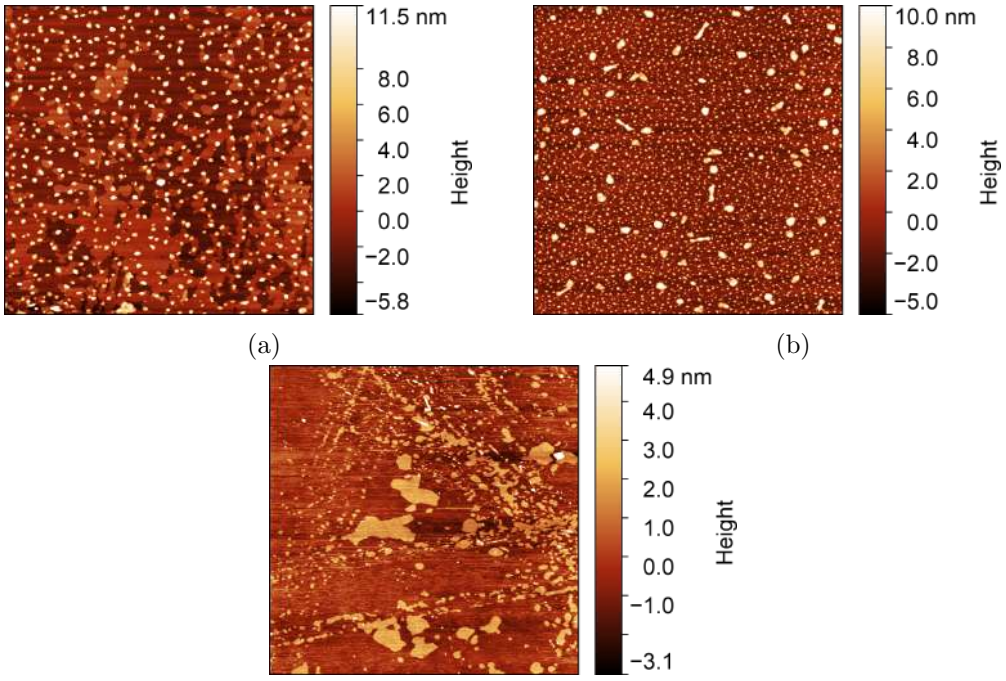

Figure 5.5: AFM 10 by 10 µm height maps collected on films growth for (a) 30 seconds (corresponding to about 1 nm of thickness), (b) 2 minutes (corresponding to about 4.5 nm of thickness) and (c) 10 minutes (corresponding to about 20 nm of thickness).

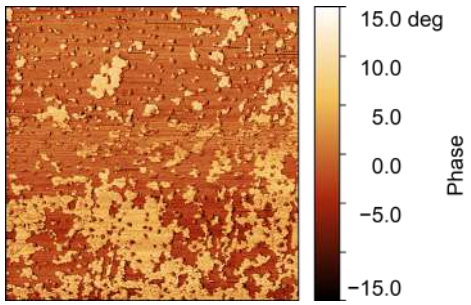

Figure 5.6: AFM 10 by 10 µm phase map (corresponding to Figure 5.7d).

The morphology changes after the TT (maps reported in Figure 5.7): the previous detected terraces disappear and a full layer forms also in the thinner film. Probably the TT allowed a local partial diffusion so that the material of the islands move to the other regions so to fill the empty spaces.

5.1.4 AFM vs. Thermal Treatment

We studied both the effect of the temperature and the duration of the TT. The collected images, together with some profiles, are reported in Figure 5.8 (temperatures) and in Figure 5.10 (duration).

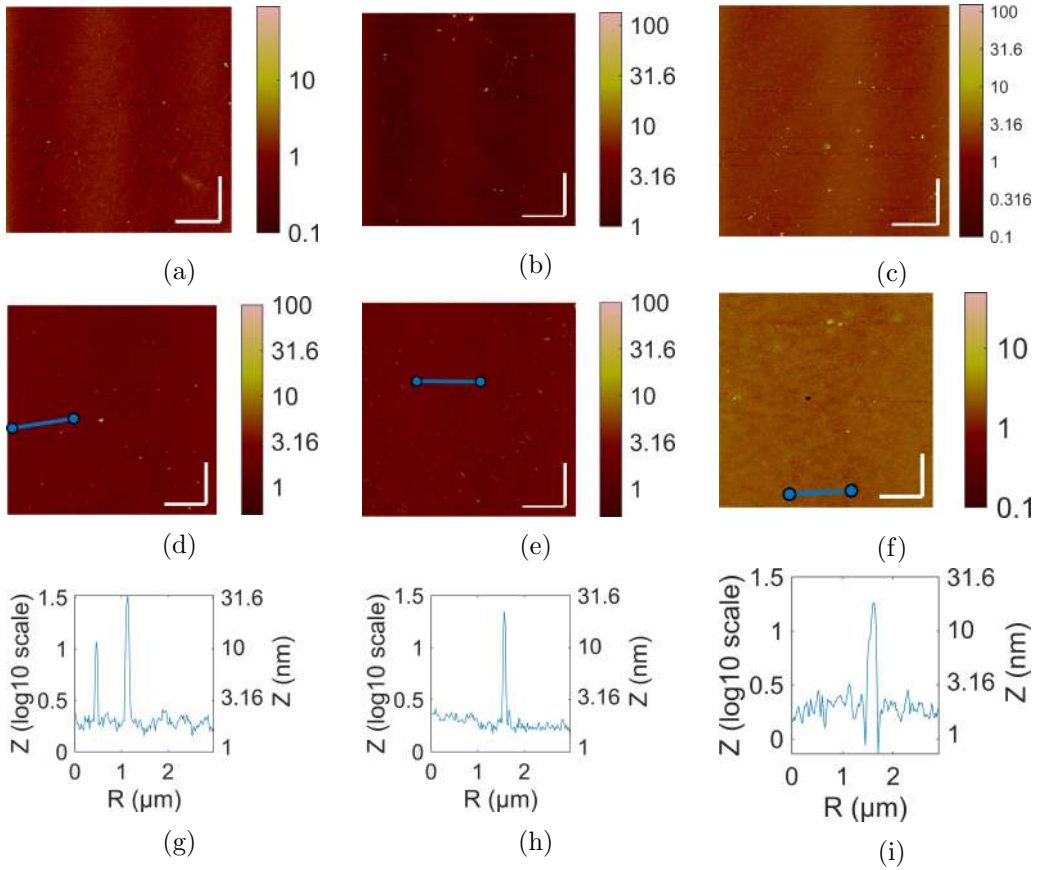

Figure 5.7: AFM maps collected on films growth for 30 seconds (first column, corresponding to about 1 nm of thickness), 2 minutes (second column, corresponding to about 4.5 nm of thickness) and 10 minutes (third column, corresponding to about 20 nm of thickness) and then TT at 700°C for 30 minutes. The lateral colorbar refer to the height (in nm). Top line: wide scan (scalebars are 10 by 10 µm); middle line: narrow scan (scalebars are 2 by 2 µm); bottom line: height profiles obtained along the blue lines in previous images.

We estimated the number of particles (arbitrary divided into 3 families) and the total surface fraction occupied by them when the temperature varies. The results of these analysis are reported in Figure 5.9.
The results show that the optimal temperature to have uniform NPs is about 650°C: below such temperature their number, especially the smaller ones, growth with the temperature, most probably because they are forming, but over this temperature, their density decrease. However, thanks to the occupancy fraction, we know that they are not simply dissolving, otherwise this latter number should decrease too. The only possibility is that they merge with the others, resulting in fewer but larger NPs. The change in the occupancy variation (the line slope) is a collateral effect of this phenomena: a large portion of the extra increase come from the area between an old center and the other that appear as part of the new NP to the AFM.
Concerning the duration of the treatment, reported in Figure 5.10, we can say that the optimal time is around 10 minutes(Figure 5.10b). In this situation we still have some very small NPs, but larger ones are also present. The latter is not true for samples treated for shorter times (Figure 5.10a) where only the NPs from the "small" family are observed. Longer times led instead to an almost flat surface (Figure 5.10c). We explain this last result considering the fact that we are annealing the sample at a temperature very larger than the measured glass-transition one (around 570°C) for quite some time. Doing so, we rise a lot the viscosity of the entire film enhancing the diffusion to the point that the hills can flatter, moving the exceeding matter to the surrounding.

5.2 SEM

Investigation made in collaboration with **Piattaforma di microscopia** group.

5.2.1 SEM theory

A Scanning Electron Microscope (SEM) is an instrument used to probe the surface of samples by using a focused beam of electrons accelerated thanks to a voltage ranging from fractions of kV (on modern instruments) up to few tens of kV. The electrons will then hit the samples with the corresponding energy on a very small spot at each time. The size of this spot depends on the selected magnification and will correspond to a pixel in the final image.
The electrons have enough energy to interact with the investigated material in many way, both being absorbed by the atoms and re-emitted or they just can be deflected.

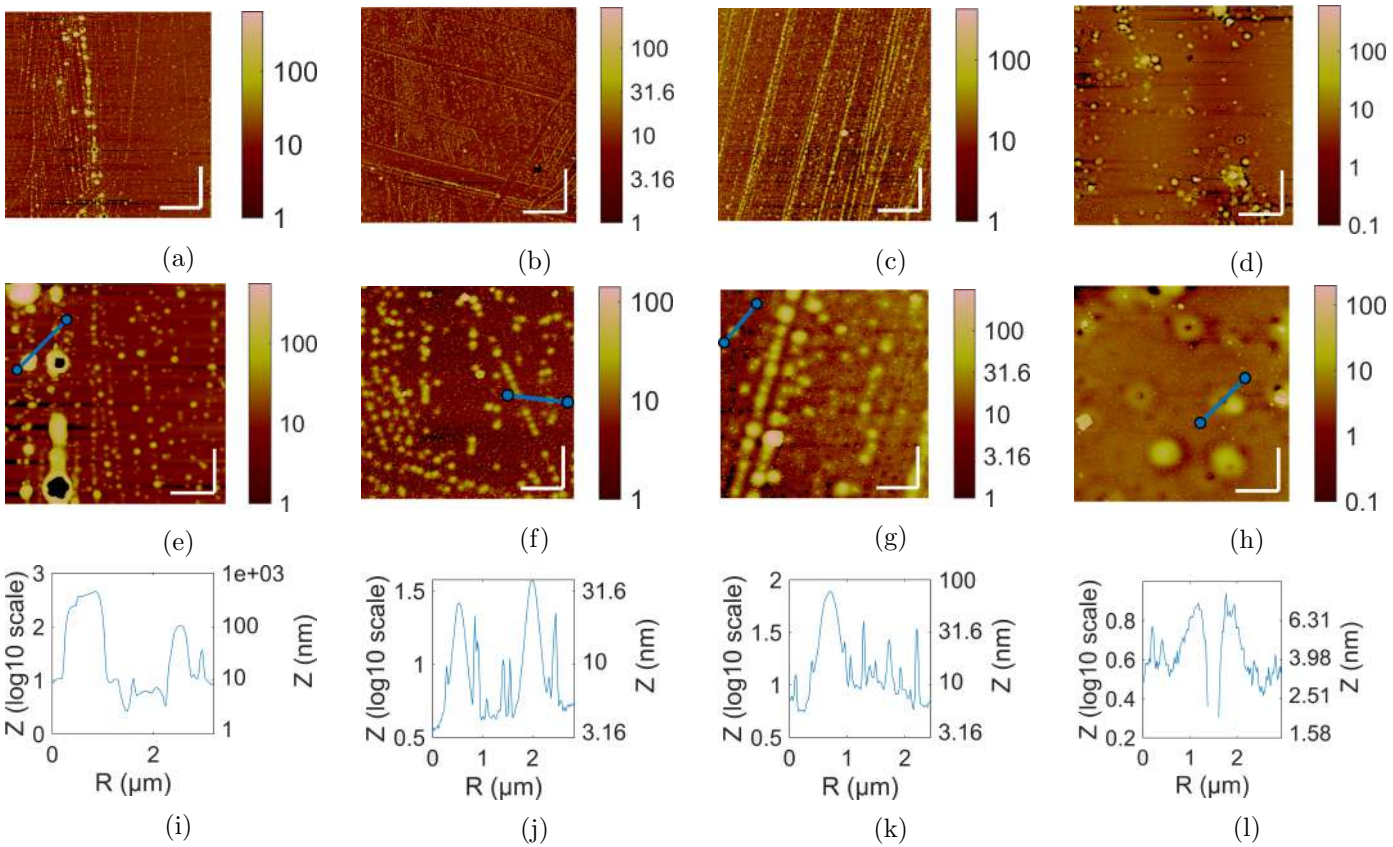

Figure 5.8: AFM maps collected on films growth for 60 minutes and then TT for 30 minutes at 600°C (first column), 640°C (second column), 660°C (third column) and 700°C (fourth column). The lateral colorbar refer to the height (in nm). Top line: wide scan (scalebars are 10 by 10 µm); middle line: narrow scan (scalebars are 2 by 2 µm); bottom line: height profiles obtained along the blue lines in previous images.

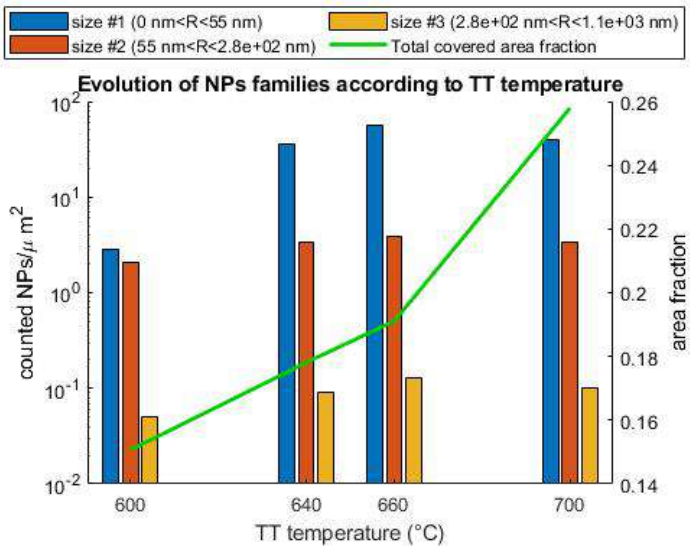

Figure 5.9: Density of detected nanoparticles (bars) and total area fraction covered by them (line) obtained from the analysis of the 10-by-10 µm images in Figure 5.8.

The most common images come from back-scattered (BSE) and secondary (SE) electrons.

BSE originate from electrons that travel quite near an atomic nucleus, so near that the electrostatic force between the electron (negative charge) and the nucleus itself is enough to make the electron backscattered. Due to their origin, the possibility that an electron is deflected at a given φ angle is

$$\frac{d\sigma}{d\Omega} = \frac{4Z^2}{a_0^2} \frac{1}{\left[\frac{16\pi^2}{\lambda^2}\sin^2\left(\frac{\phi}{2}\right) + \frac{1}{R_s^2}\right]} \tag{5.1}$$

and the direction distribution can be found in [56, Fig. 2] and they depends both on the electron nature (the wavelength λ), the scattering nucleus (the atomic number Z that influence also the shielding radius R_s) and some constants (i.e. the Bohr radius a_0). However, when multiple scattering process are considered, on average, the detected electrons follow a simpler rule:

$$I_{observed} = I_{max}\cos(\Phi) \tag{5.2}$$

with Φ being the angle between the detector and the specular reflection of the primary beam, so, for this reason, the BSE detector is placed very near the gun exit, so to have $\Phi \approx 0$ for not tilted samples.

On the opposite, SE are emitted almost homogeneous in all the directions but are easily absorbed again (they have very low energy compared to the primary beam, just

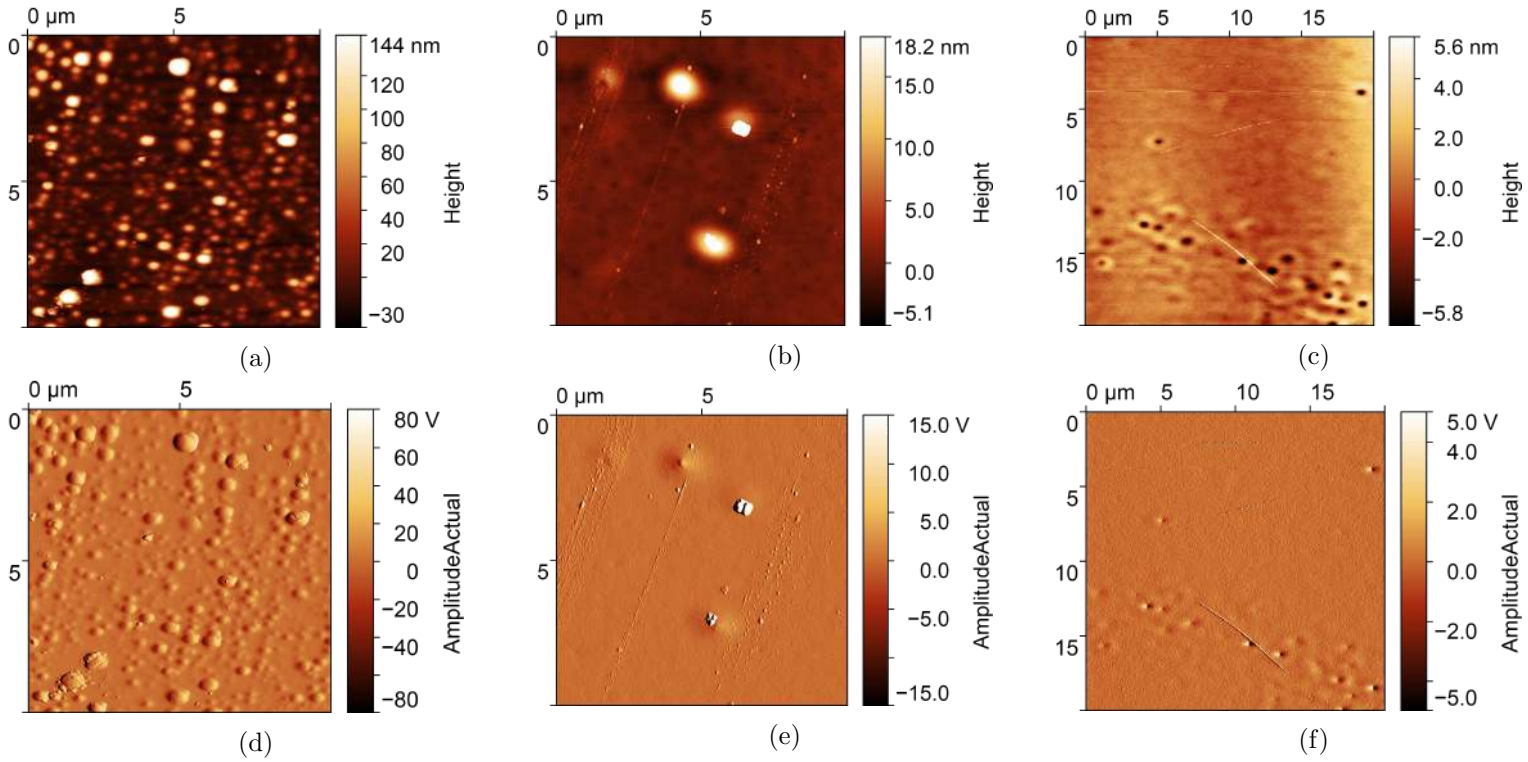

Figure 5.10: AFM maps collected on films growth for 60 minutes and then TT at 700°C for 5 minutes (first column), 10 minutes (second column) and 60 minutes (third column). Top line: height maps; bottom line: signal amplitude maps

few eV) from the material itself, so is very sensitive to the surface and the detector doesn't have to be placed in any special position. However, SE can come from different point of the sample (i.e. where the primary beam hit the sample, SE1, or when a BSE exit the sample, SE2) or even from other sources (such as the BSE detector, SE3). Select just the "correct" electrons is not trivial due to the fact that all these emissions have undistinguishable energy, so, in the recent years, manufacturers of SEMs have found a different way to filter such electrons: a combination of a mechanical filter (the primary beam window) coupled with a secondary electrical field that allows the selection of just the electrons that came straight from above such window. This solution involve the use of a detector that is inside the column, and that is usually called *in-lens* (see for example Figure 5.11).
SEMs also have other possible use. For example, at high energies (tens of keV) electrons acts similar to the photons with corresponding energy, allowing similar characterization, such as diffraction (EBSD when BSE are probed, however it is more common to see these results using a transmission microscope where traditional diffraction figures can be seen) or XRF, that in this case take the name of EDX (Energy Dispersive X-ray Analysis/Spectrometry) and gives access to the same informations (elemental analysis) but with a smaller lateral resolution. A side effect of working with a SEM is the fact that working in vacuum, also elements lighter than nitrogen can be observed.
In this work we used two SEMs: a Tescan VEGA TS Univac 5136XM and a Zeiss Gemini 500 equipped with a Bruker Quantax EDX micro probe that could work at very low energy (sub keV) so to avoid charging effects, quite common in insulating samples. However, for elemental analysis, an order of magnitude higher energy was required to detect all the atoms (emissions up to 3 keV that required 5 to 10 keV from the primary beam).

5.2.2 SEM imaging

Many images have been collected on different samples and at different magnifications, so to fully record the morphology of them. In Figure 5.12 there is a selection of them taken on samples TT at different temperatures, so to show the differences between them.
Every image look very different from each other, so no proper consideration about the effect of the temperature can be done, however, we can say that the films are not homogeneus, showing particles of different size and that sometimes these particles can merge together to form larger structures. Moreover, we studied samples deposited in

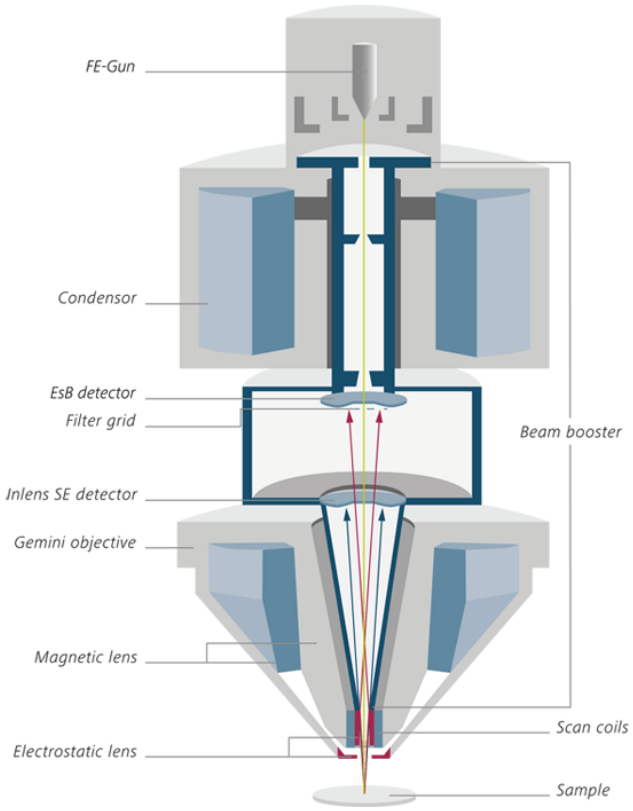

Figure 5.11: Diagram with the principal components of an SEM column (Zeiss Gemini layout). Image from Zeiss website.

multiple runs. Something inside the material produces gas bubbles (like the one in Figure 5.13) that broke the homogeneity of the films, introducing scattering centres (optical properties) and inducing an expansion of the film (increased thickness). According to SEM images, these bubbles have a lateral radius of few µm, so the reported increase in volume of 4/5 times during the annealing is fully explained, but despite their volume fraction, the investigation about the possible elemental composition of this gas, tested with different techniques (XPS, EDX, selective etching, ...), returned different possibilities. The most probable one however is the evolution of gas species starting from the alkali metals present in the starting glassy target.

5.2.3 EDX analysis

On normal XRF instruments (even the micro- ones) the incident beam is macroscopic, so it probes a region of the sample so large that it can return the average composition of the whole sample. The advantage of using the electron beam of a SEM instrument to perform this analysis is that the lateral resolution of this kind of beams is better

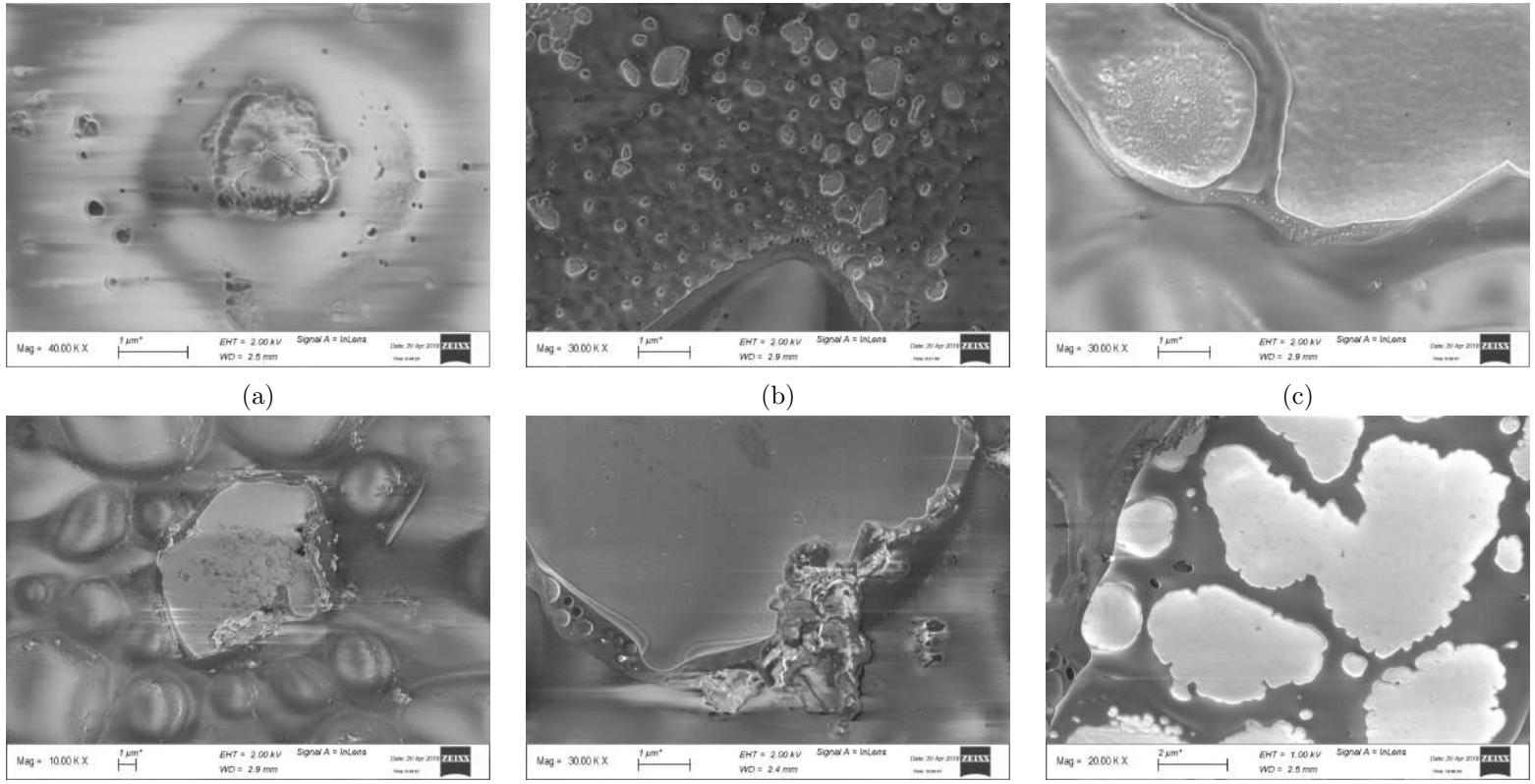

Figure 5.12: SEM images collected on films growth in 4 runs of 60 minutes each and then TT for 30 minutes at (a) 600°C, (b) 620°C, (c) 640°C, (d) 660°C, (e) 680°C and (f) 700°C.

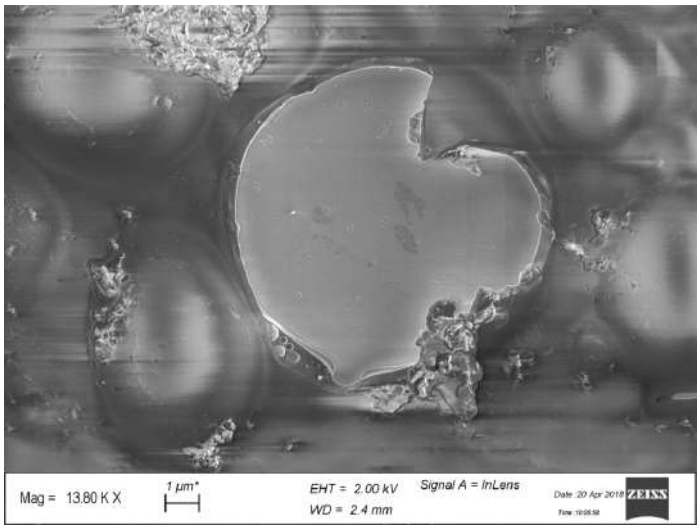

Figure 5.13: Another picture taken from the sample TT at 680°C. This image in particular show clearly a broken bubble on the film surface.

(basically a pixel in the images), so that punctual analysis or micro mapping are theoretically possible. However, in practice, this in not true because even if the incident beam is smaller than 1 nm, it excites the material in a pear-like region that extend for few µm (the exact extension can be approximated using some simulations and it depends on the density and composition of the medium).
Some example of EDX analysis are reported in Figure 5.14, together with the detected lines. The high concentration of carbon is an experimental artefact: as already stated, charging effect can occur on insulating samples, so to reduce such effects, a thin layer of graphite (C) was evaporated on the films.
Precise quantification of these spectra is not possible, also because they were taken not in standard conditions (beam energy of 5keV instead of 20 keV)and due to the analysis volume spacing also to the substrate. We however did a pseudo-quantification by comparing the signals from the three elements that should only be inside the films: O, Ga and Ge. The results of this analysis is reported in Table 5.1. All the data appear to be quite far from the expected values (probably due to the wrong measurement conditions), but the Ga/Ge ratio inside and outside the NPs appears to be statistically different.
In Figure 5.14b, a spectra collected on a bubble is reported, where a weak peak of Ar can be seen at 3 keV.

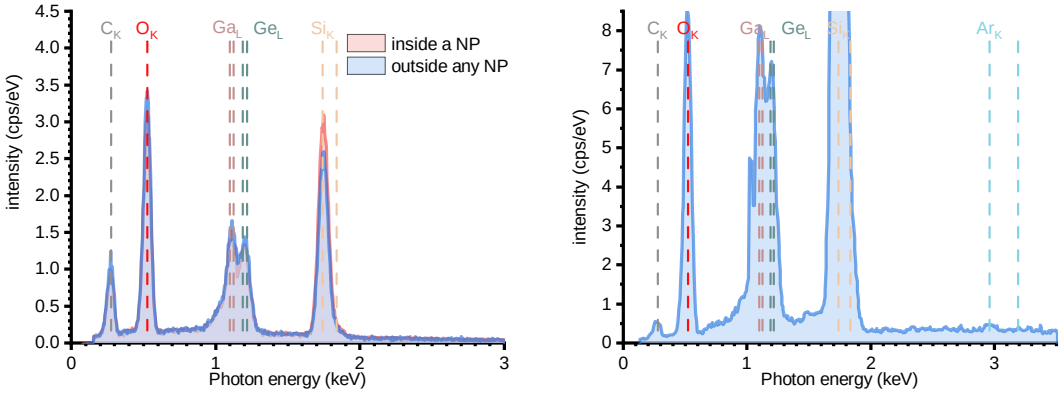

(a) (b)

Figure 5.14: EDX spectra collected on my samples. Vertical lines are the expected position corresponding to the labelled transitions. (a) confrontation of two point scans collected above a detected NP and in the surrounding area. (b) EDX spectra collected on a sample deposited in 4 runs of 60 minutes each.

location of the scans	Ga/Ge ratio		Ga/O ratio	
	value	error	value	error
inside NPs	1.061	0,002	0.107	0.008
outside NPs	1.026	0.004	0.100	0.013
whole sample (experiment)	1.0432	0.0013	0.105	0.04
whole sample (theoretical)	0.8889		0.1905	

Table 5.1: Ratio between Ga, Ge and O according to EDX measurements. Every value and error has been statistically calculated starting from different scans in different locations of the film.

Chapter 6

Electrical characterization

6.1 Sample preparation and experimental set-up

Investigation made in collaboration with **Polifab** group from **Politecnico di Milano**.

The samples described in section 2.0 are ready to be measured in many different way, but for electrical tests, further steps must be taken in order to connect the instrument to the sample in the best possible way.
The characterization presented in this chapter has been performed on films growth by a former member of the research group (Dr. A. Azarbod) which thickness is around 70 nm. On these films, a top electrode was added by evaporation of different metals at the Polifab facility of Politecnico di Milano. The available metal electrode were:

1. 100 nm of gold;
2. 100 nm of chromium;
3. 5 nm of chromium and then 50 nm of gold;

Two samples (one AD and one TT) with each metallization have been prepared and studied.
The two metals have been choosed because of their conductivity (especially gold) and their work function similar to the conduction band energy of the gallium oxide. In literature, however, a combination of titanium and gold is often used as electrode (for example [57]) so to have a more ohmic contact. In fact, as discussed later on (Figure 6.3.3), the devices characterized in this work, appear to act as 2 asymmetric back-to-back Schottky barrier diodes, although the origin of this effect can be explained by the conductivity inside the glass itself[58]. As bottom electrode, a p-doped Silicon wafer has been used. In this way, the tested devices can be classified

as MOS (Metal-Oxide-Semiconductor) capacitor, with the component to study being the oxide layer.
When dealing with electric measurements, the used set-up should address:

- the possibility to rapidly and easily change the connected device;
- the optimization of electrical conductivity.

Usually these two conditions need opposite requirements, and the solution adopted in this work evolved in the time in the effort to optimize both (in figure Figure 6.1a I included a schematic of the most complex used).
The top electrode is the one that underwent major updates. The first set-up involved a simple needle positioned on the metallization. This connection is very simple but has the drawback of poor reproducibility (both the pressure of the needle on the electrode and their reciprocal position change it) and the scratching of the metallization itself. To overcome these issues, I started to use some short (few cm) wires, either intended for electrical civil cabling or for microelectronic prototyping, secured to the metallization with some silver paint; in case of Cr electrode, a cleaning with a decaping agent (a solution of EDTA) was also implemented at a certain point. These precautions granted more reproducibility and longer life for the electrodes, but the system become more complex and the problem of reproducibility and the consumption of the metallization due to the mechanical failure of the connection (the system was very fragile and the manipulation of the wire itself too often lead to its detachment from the electrode) was more severe than before, eventually leading to the complete consumption of the metalizzation.
The bottom electrode configuration instead was kept more or less the same, and it consisted in a copper plate secured to the silicon wafer again with silver paint. To improve the conductibility of the system, the copper was cleaned in a solution of 5% acetic acid diluted in water and the silicon was scratched with a diamond pen immersed in the In-Ga eutectic.
All these solution didn't proved to be adequate, so further improvement is suggested, maybe using some microelectronic chip carriers, in case of additional electric characterizations.
The instrument used for all the measurements is an HP 4284A LCRmeter (Figure 6.1b), and it is fitted with 4 BNC terminals and a ground "banana" socket (to allow up to 5 terminal measurements [59, sec. 3.1]). The used configuration is only a 2 terminal one, with the extra ground connector completely ignored and the other terminals connected in pairs. The connections closed to the sample are made using

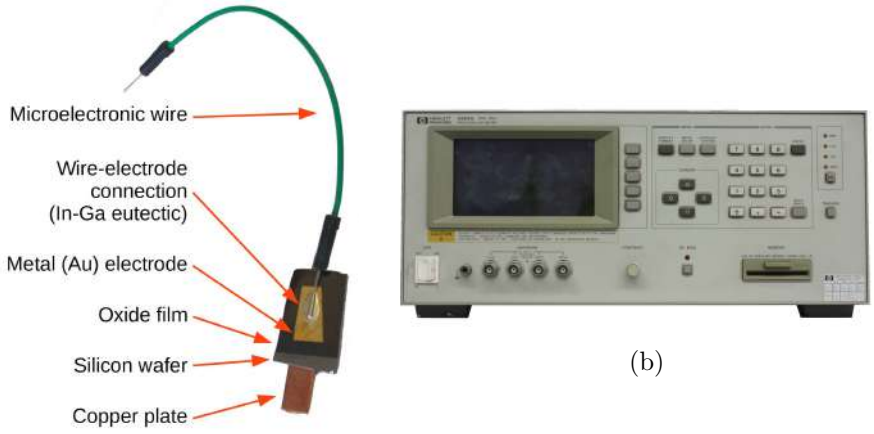

(a) (b)

Figure 6.1: (a) schematic of a sample used for electrical measurement. (b) The instrument used, an HP 4284A LCRmeter, see from the front.

not shielded banana cables. To reduce the effect of this low quality network, open and short circuit corrections have been often used (see section 6.1.1).

6.1.1 Stability and reproducibility

All the efforts employed in the evolution of the contacts described above, was necessary in the attempt to reach stable and reproducible measurements. Unfortunately this objective wasn't fully achieved due to the fact that all the interfaces give in principle a non negligible contribute to the final signal. However, tests have been made to isolate all the possible source of non-reproducibility.
In particular, it has been found that:

- new contacts (especially if not cured with the application of a decade of DC volts);
- applying open/short corrections, sometimes (especially later on) failed resulting in negative resistances at high frequencies (physically impossible);

lead to barely reliable measurement, while others such as

- turning on/off the instrument;
- connecting and disconnecting the sample (especially if the wire set-up is used);
- using different probing (AC) signal voltages;

- using different configurations of the Analogue-Digital Converter (integration time e sample averaging);
- re-measuring the open and short circuit correction (some times).

have a very limited effect on the results.

6.2 I.S. theory

Impedance Spectroscopy (IS) is a technique used in different fields, but especially the ones that involve electrochemical reactions (so diffuse that usually it is referred as Electrochemical-IS, EIS). Other fields involve real-time measurement in sensors and, of course, dielectric systems.
During an IS experiment, an alternate electrical signal (either in the form of current or voltage) is sent to the sample, and the opposite signal (so respectively voltage or current) is acquired in both the intensity and (phase) delay, this happens for many different frequencies. From the ratio between the current and the voltage and the phase delay, the complex impedance

$$\tilde{Z} = R + \imath X = |Z| \exp(\imath\delta) \tag{6.1}$$

is calculated. In the previous formula, R is the resistance, X is the reactance and δ is the angle that the impedance vector $\tilde{Z}$ have with the real positive half-axis in the complex plane.
Depending on the frequency range, different ways to measure such values can be used. The most common are [59, sec. 2.3, 2.5 and 2.6]):

(auto balanced) bridges : this method is basically an extension of the Wheatstone bridge[60] in which not only the real part of the impedance (the resistance) is balanced but also the phase (reactance). Normal bridges require an operator to manually tune the circuit elements, while auto-balanced (and the LCRmeter used is one of them) do it themselves thanks to feedback circuits;

radio frequency I-V decoupling : this instruments, that can work at higher frequencies, are basically an oscilloscope together with a function generator. The function generator provide the voltage probing signal and the oscilloscope is used to measure the response signal. Since one is interested in both the voltage and the current, the measurement is splitted in two: one that is measured directly (voltage) and the second that is delayed by $\pi/2$ by using

a transformer. Each couple of data is then processed and transformed in the complex impedance;

network analysis : this method is the one that can be used for very high (GHz to THz) frequencies. On the opposite of the former, this method measures the reflected impedance and not the transmitted one. The reflection coefficient is defined as

$$\Gamma_x = \frac{Z_x - Z_0}{Z_x + Z_0} \tag{6.2}$$

with Z_0 being a known impedance (usually 50Ω) and Z_x is the sample impedance, so knowing Γ_x, the phase of the impedance can be calculated. Unfortunately there is no way to know the absolute value of Z_x, and more over, the accuracy of the measurement strongly depends on this value and it's higher for $|Z_x - Z_0| \approx 0$.

The collected data are complex numbers and a function of the frequency ($\tilde{Z}(\nu)$). Thus a correct data representation needs a 3D representation (Figure 6.2a). Anyway the clarity of such plots isn't so high, so three different 2D representations are often used, with one of the axis perpendicular to the graph plane. R (Figure 6.2b) and X (Figure 6.2c) plots versus the frequency are trivial (but still have some nice and important characteristics), while the -X vs. R plots (Figure 6.2d), often called "Nyquist plot" or inappropriately "Cole-Cole plot", are the most used. In such plots increasing the frequency leads to the points moving counter-clockwise, forming shapes that range from single point to straight line or semi-circles, depending on the nature of the sample. The first type of interpretation (EC, more engineer oriented) is based on these shapes.
Together with the Z function, there are other three connected physical quantities [61]:

Y , the admittance, is defined as the inverse of impedance ($Y = 1/Z$);

C , the complex capacitance, is one over the impedance times the imaginary unit and the pulsation ($C = 1/(Z \cdot (\imath\omega))$; in this case, $\tilde{C} \doteq C' - \imath C$" (so is the complex conjugate of the usual definition)[62, eq. 3];

M , the impedance modulus, is defined as the inverse of the complex capacitance ($M = 1/C = Z \cdot (\imath\omega)$.

An example of the 4 Nyquist views can be seen in Figure 6.3.
All these quantities also have their intrinsic counterparts.

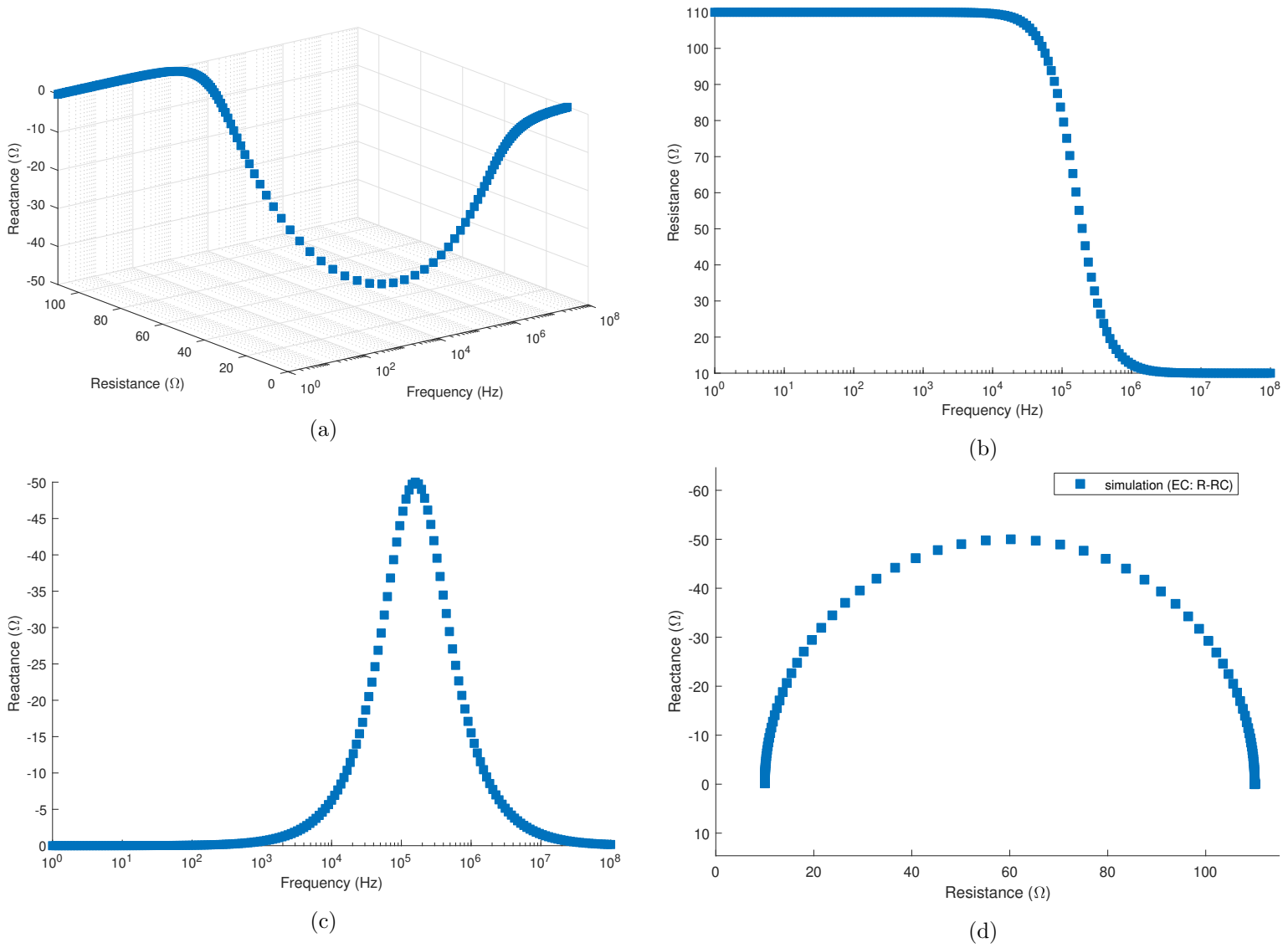

Figure 6.2: Representation of an impedance spectra in Z space: (a) 3D space, (b) R versus frequency (X $\perp$ graph plane), (c) X versus frequency (R $\perp$ graph plane) and (d) -X versus R (frequency $\perp$ graph plane). Data have been calculated starting from an EC made by a serial resistance of 10 Ω and a second resistance of 100 Ω in parallel with a capacitance of 10 nF.

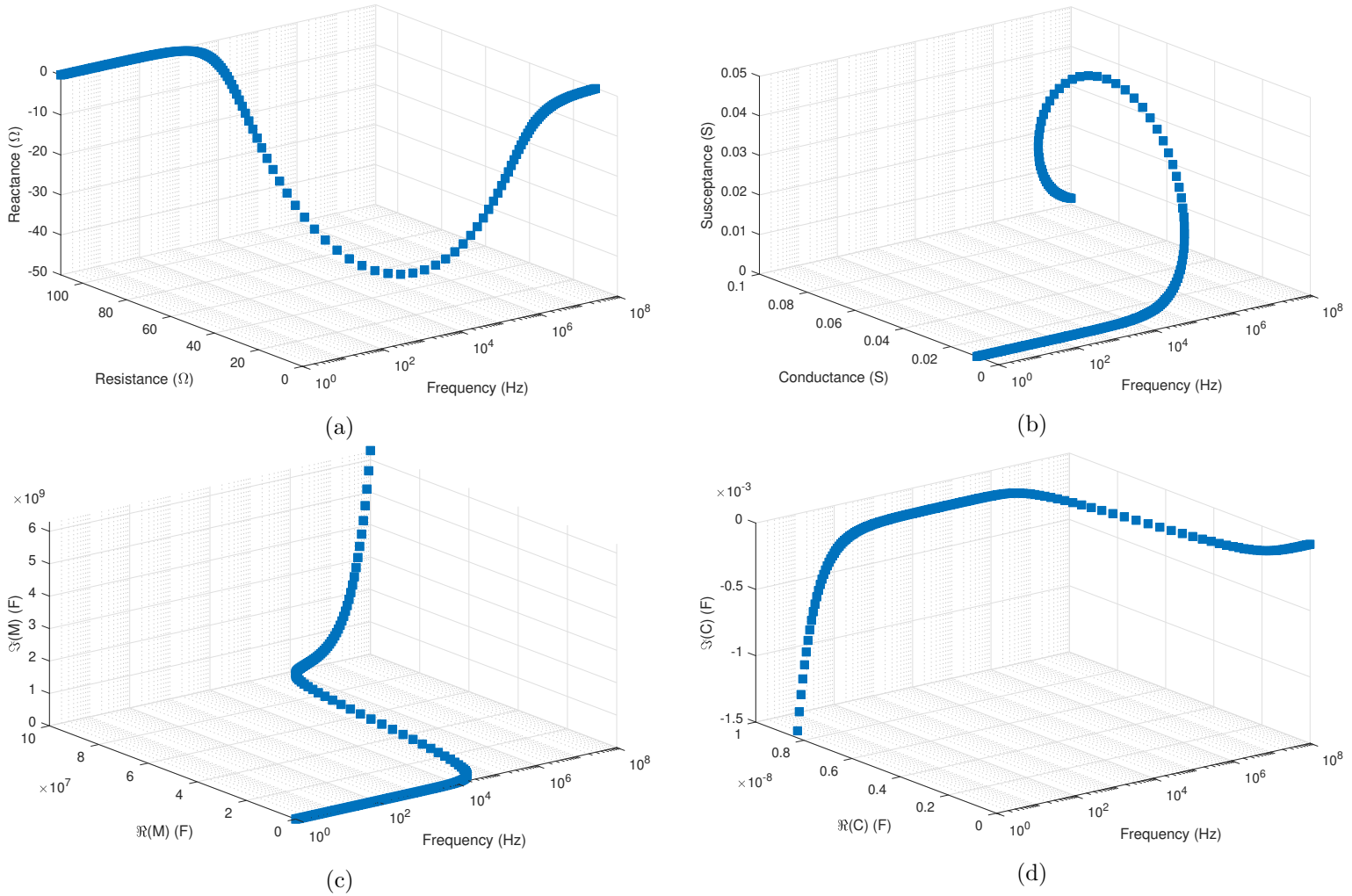

Figure 6.3: 3D representation of impedance spectra in different spaces (imaginary vs. real part vs. frequency): (a) impedance (Z), (b) admittance (Y), (c) impedance modulus (M) and (d) the complex capacitance (ε).

6.2.1 Dissipation/Quality factors

Dissipation (D-) and quality (Q-) factors are quantities that define the overall performances of a device, without entering in the possible conduction mechanisms. In particular, the D-factor is an indication of how well a device can dissipate electrical energy, while the Q-factor evaluate the storing capacity of such device.
Since these numbers only depends on the measured value of the impedance (or Y, C, M and their intrinsic counterparts), there are multiple ways to define them, but usually D is defined as

$$D = |\tan(\delta)| = \frac{R}{|X|} \tag{6.3}$$

with R, X, and δ defined in Equation 6.1. The second quantity is usually defined starting from the first since

$$Q = \frac{1}{D} \tag{6.4}$$

In Figure 6.4, I'm reporting the Q- and D-factors obtained starting from the simulated data in Figure 6.2. In this ideal behaviour the log-log plots show two linear regimes with slopes of ±1, resulting from the fact that far from the resonant frequency the total resistance of the circuit can be approximated to either 10 Ω (at high frequencies the parallel resistance is negligible) or 110 Ω (at DC frequencies the EC degenerate to just the two resistances in series), while the reactance is directly proportional to ν when $\omega \ll \tau$ and inversely proportional when $\omega \gg \tau$.

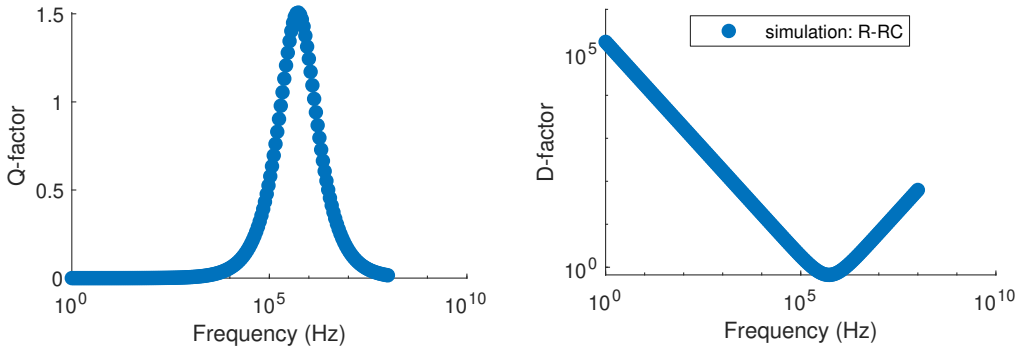

(a) (b)

Figure 6.4: (a) Quality and (b) dissipation factors corresponding to the simulation of Figure 6.2.

In our devices we instead register something a bit different (Figure 6.5): first of all, we cannot detect the post-relaxation recovery (the Q decay and/or the D rise), and this should be a hint that something important is taking place at higher frequencies, but it's outside our spectroscopic range. The second important difference is instead just

after the local Q maximum (D minimum) and appears almost as a plateau. Looking better, it's instead the results of the presence of a second weak contribution.

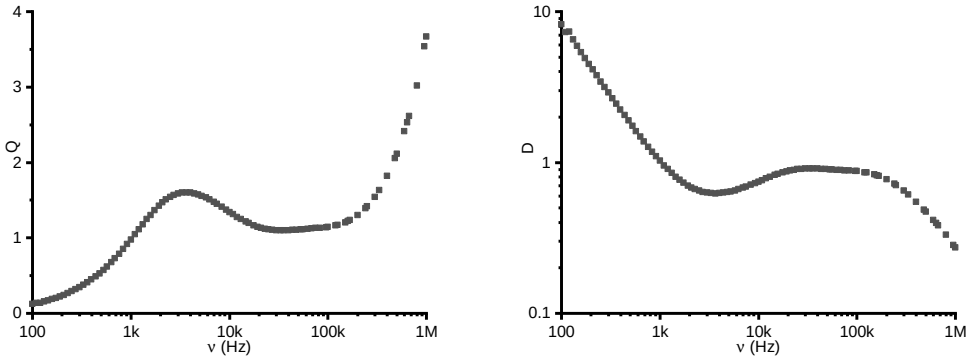

(a) (b)

Figure 6.5: (a) Quality and (b) dissipation factors calculated starting from impedance measurements collected on our samples at rest conditions.

This is confirmed when an external (positive) DC bias is applied (Figure 6.6): the low frequency contribution disappears completely and the high-frequency one moves to even greater frequencies becoming at the same time more defined.
The effect of the temperature (Figure 6.7) is instead more rigid, shifting all the values up or down with the temperature, however different region in the spectra are affected with different intensities.

6.3 E.C. fitting

6.3.1 Theory

This first kind of fitting is based on the assumption that three[1] basic type of elements (resistors, capacitors and inductors), if properly linked together, can replace any "black box" system. The electrical layout is commonly called circuit and since that it acts as the unknown object, it's said that the two entities are (electrically) equivalent, from here the name of Equivalent Circuit (EC). Together with these three basic and real elements, often other three elements can be seen in the IS analyses: the Constant Phase Element (also called CPE), the Gerisher and the Warburg ones. These three elements cannot be really associate to a single physical entity, but they are more like

[1]actually, especially for what concern electrochemical systems, other elements must also be used to describe many systems

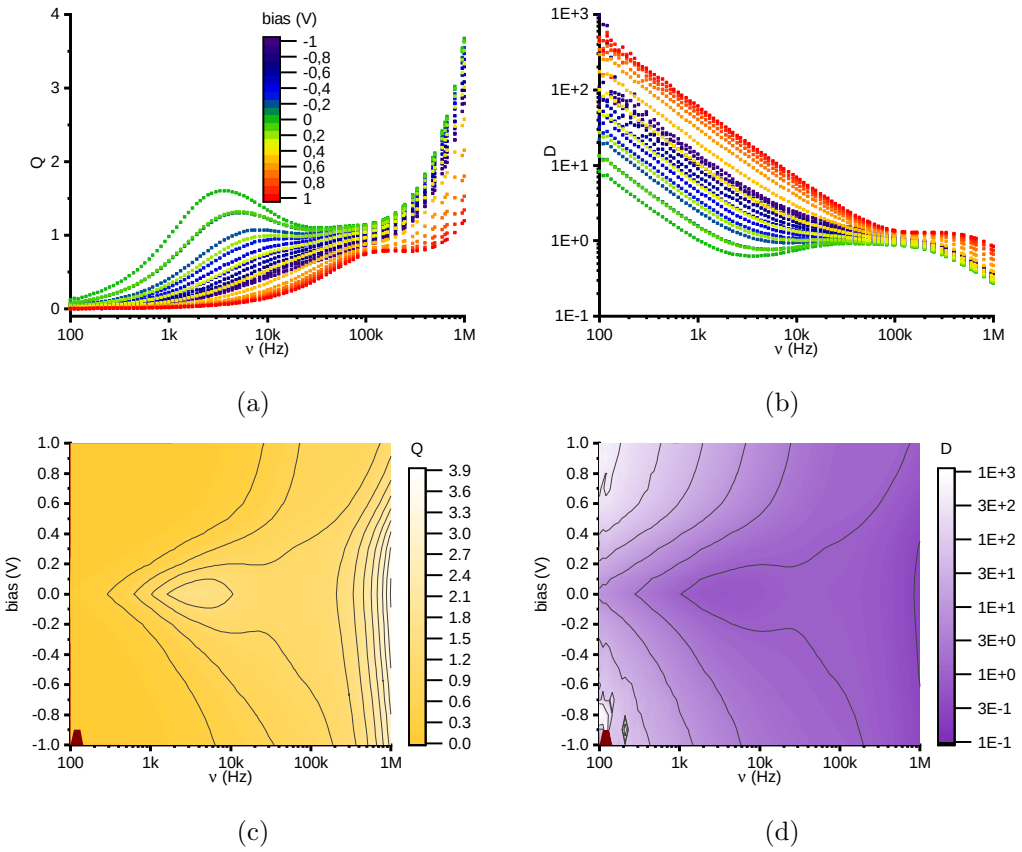

Figure 6.6: (a) Quality and (b) dissipation factors calculated starting from impedance measurements collected on our samples at different bias. (c) and (d) the same data presented as contour plots.

mathematical construction to approximate distributions of the former elements (the CPE) or with chemical diffusion (Warburg and Gerisher). The latter are mainly used for characterization of dynamic samples, usually during an electrochemical process, and they will not be discussed further here.
These four elements have four way to respond to some electrical stimulus:

the resistor (symbolized with a zig-zag line, like in Figure 6.8a, or with the capital letter R) simply acts against the flow of current into a circuit but without modifying it's phase in case of an alternate signal. The formula for the impedance is:

$$Z(\nu) = R \tag{6.5}$$

the capacitor (symbolized with two parallel lines perpendicular to the circuit flow, like in Figure 6.8b, or with the capital letter C) its an element where the charge carriers can accumulate; the simplest models, although not very practically

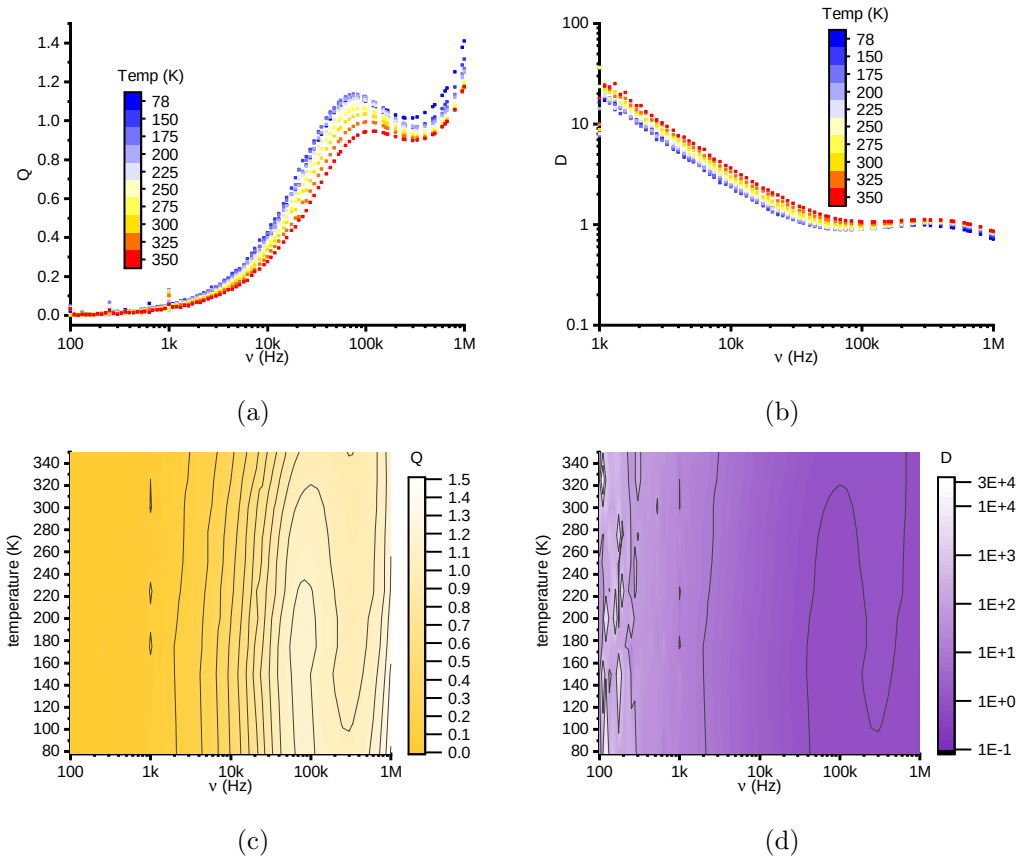

Figure 6.7: (a) Quality and (b) dissipation factors calculated starting from impedance measurements collected on our samples at different bias. (c) and (d) the same data presented as contour plots.

used due to its limits, consist indeed in two parallel plates with nothing in between. A perfect capacitor should release completely the stored charged, so if one considers long enough times, the average net energy drained by such element should be zero, but the release happens obviously after the accumulation, so the effect of such element is to delay the current response respect to the voltage signal by a quarter of the signal period. The formula for the impedance is:

$$Z(\nu) = \frac{1}{\imath \cdot 2 \cdot \pi \cdot \nu \cdot C} \tag{6.6}$$

the inductor (symbolized with a cylindrical spiral with it's axis along the circuit flow, like in Figure 6.8c, or with the capital letter L) is an electric element were the magnetic field plays an important role on generating self-induced currents that result in an enhancement of the effect of a voltage change in the current passing through it, giving the impression that the current precedes the voltage by a quarter of period. To achieve this, the best way is to use a conducting

wire coated with some insulator (i.e. a polymer) and then turned many times so to form an elongated shape with a tunnel inside; to enhance it's property, the cavity can be filled with a magnetic medium, so to increase the magnetic field inside. Since its effect relies on the change of the voltage, and supposing to consider a large enough time span, the net energy stored by this element equal zero. The formula for the impedance is:

$$Z(\nu) = \imath \cdot 2 \cdot \pi \cdot \nu \cdot L \tag{6.7}$$

the CPE (often symbolized as two closing angular brackets displaced each other a bit, like in Figure 6.8d, or with the capital letter Q) it is a mathematical model that approximate a distribution of the former elements with slightly different intensities. Since it should account for this distribution, it depend on two different parameters: the intensity Q and the coefficient n. This coefficient is limited between $[-1, +1]$ and tell about both what kind of element it approximates (close to -1 if the CPE acts like an inductor, 0 if it seems a resistor or +1 if it resembles a capacitor) and how broad the distribution of the values is (how far n is from the expected value). The formula for the impedance is:

$$Z(\nu) = \frac{1}{(2 \cdot \pi \cdot \nu)^n \cdot Q} \cdot \exp\left(-\frac{\pi}{2} \cdot n \cdot \imath\right) = \frac{1}{(\imath \cdot 2 \cdot \pi \cdot \nu)^n \cdot Q} \tag{6.8}$$

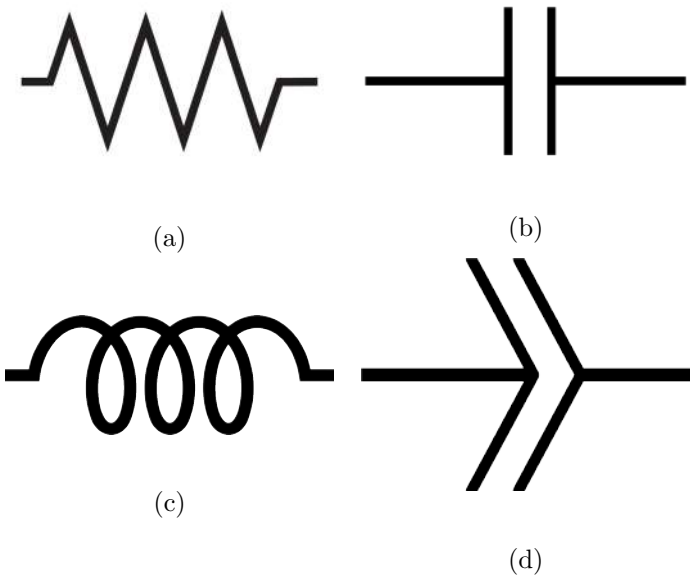

Figure 6.8: The symbols commonly used to indicate (a) a resistor, (b) a capacitor, (c) an inductor and (d) a constant phase element.

where, ν denote the frequency of the signal that can be converted to the angular frequency $\omega = 2 \cdot \pi \cdot \nu$. The total impedance for the system can then be calculated iterating the formula for serial elements

$$Z_{TOT,serial} = \sum_i Z_i \tag{6.9}$$

and the one for parallel elements

$$Z_{TOT,parallel} = \left(\sum_i \frac{1}{Z_i} \right)^{-1} \tag{6.10}$$

starting from the inner elements and moving to the outer ones. However, since the explicit calculation rapidly results in bulky and not easily readable formulas, it's often omitted in the works and replaced by just the electric schematic.
This modellization is used to simplify any real complex electrical system into it's components, either for studying the whole conduction mechanism (as in my case) or to monitor one of their components (i.e. in commercialized detectors). However, choosing which model present in literature to use, or how to shape a new one is not a trivial task: for such purpose, the most theoretical way to draw a circuit is to start thinking about the path that the charge carriers should follow to move from one electrode of the Device Under Test (DUT) to the opposite one. Every time such carrier passes by a boundary and/or it travels inside a phase, a new effect on the impedance response function should appear. This effect usually consists in both a resistance and a capacitance and possibly also an inductance (if the given phase has magnetic properties) in parallel since the 2/3 different effect happens in same place. This should happen for every subsequent (serial) step. In the case that the charge carrier can follow two different paths to reach their destination, both path should be considered in principle, giving rise to two (or more) parallel branches in the EC.
This model quickly escalate to something impossible to deal with, both because the parameters that account for the electric elements (all the Rs, Cs, Ls, Qs and ns involved) become more than the available data points and the computational power required to fit it. Anyway, some pathway will be way more favourable than others (i.e. when measuring the resistance of a metal plate, in principle the current could also flow through the air next to it, but the resistivity of the two medium make this latter case negligible) and some step in the conduction path will add so little impedance that they could be omitted. Moreover, is often convenient to group contributions from similar sources (i.e. the two terminals in the previous metal plate example) together (and since serial elements simply sum together, this is not a problem thanks to the

commutative property of the sum), so to reduce the number of fitting parameters.
In practice, when designing the EC to use, one starts from looking at the data, counting how many time some features repeat in them and then assigning a contribution (usually a capacitance/resistance pair) to each feature. In the views described in Figure 6.3 this feature is the presence of something similar to a semi-circle (it can be deformed or degenerate into a point or in a line), while in other representation, for example quality/dissipating factors, they are peaks/valleys. Usually one can expect that such contributions happen one after the other (serial model), but sometime, they can happen inside each other (nested model). Distinguish between this two possibility is often impossible since both can explain the same measured dataset (although with slightly different values for the same elements placed in a different position in the EC).

6.3.2 Stressless behaviour

In figure Figure 6.9 I'm including some spectra collected on one of my sample (AD film with top Chromium electrode) collected in the same conditions (AC field of 100mV, no DC bias applied, no special illumination and at room temperature). As it can be seen, the impedance varies a lot, also in measurements taken in the same day. What we have observed is that the measured impedance strongly depends on the quality of the electrodes contact, and they are hardly reproducible. Moreover, we also observed an electrical curing effect, especially when the wire was (re-)applied to the metal: it doesn't matter how long we let the silver paint dry, but as soon as we were measuring the impedance, it was a couple of order of magnitude higher than normal (i.e. 10^4-1^5 Ω), but after few seconds at $\pm$10V, it drops to just thousand of Ω.
For such reason it is very important to keep the discussion on any effect limited to measurements taken on the same day and on the same sample. For this reason, the discussion about the possible differences between AD and TT films or about the effect of the different metals used for the electrodes will be very limited.
However, at least one thing seems to remain more or less constant in the majority of the measurements collected on all the samples: the presence of at least 2 different mechanisms that clearly influence the AC electrical conductibility. These can be seen as two peaks in the Q-factors plots (Figure 6.5a) and in the Distribution of Relaxation Times (DRT) analysis (Figure 6.10a) or as 2 semi-circles in the Nyquist plot (Figure 6.10b).
Any kind of representation isn't perfect on its own, so comparing more of them is strongly recommended when designing the EC to use in the data evaluation. Another

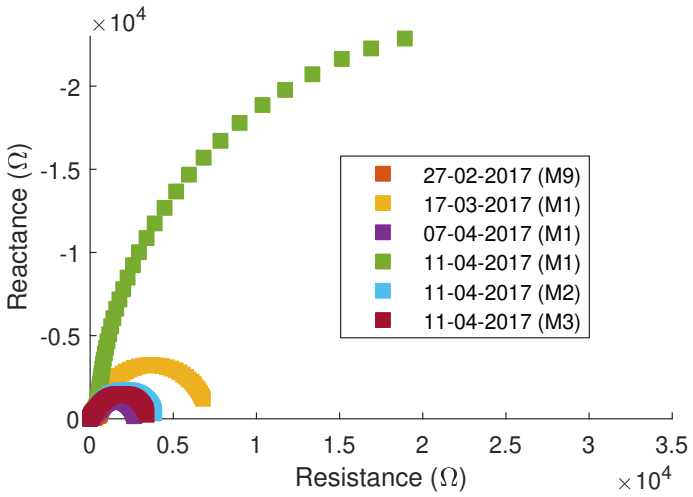

Figure 6.9: Different spectra collected on the same sample (Cr AD) in the same condition (AC field=100mV, DC field=0V, light=room, temperature=room) but at different times (in the legend there is the date in the dd-mm-yyyy format, with the parenthesis indicating the number of the same-day measurement).

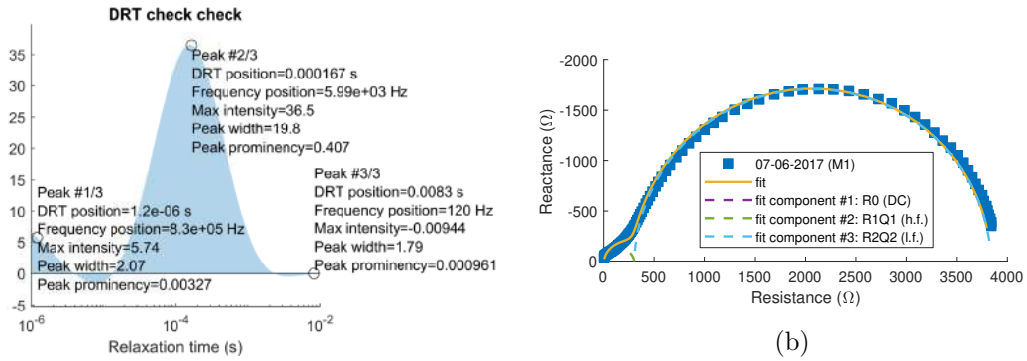

Figure 6.10: Some plots useful to identify the number and the regions in frequencies of the conductibility frequencies: (a)DRT plots each components appear as a peak, while in (b) nyquist plots they appear as semi-circles.

fact that is quite important during such design is how all the elements are linked together. For example, in Figure 6.11, the same elements (3 resistors and 2 CPEs) have been linked together in two different ways, one in which the two couples (R/CPE) have been used in series while the other where one couple is nested inside the other (in series with the outer CPE). As it can be seen, both layouts can explain the total impedance quite well (in the legend, I have also reported some sort of sum of residuals), but with completly different values for each component of the EC (a full list can be found in Table 6.1).

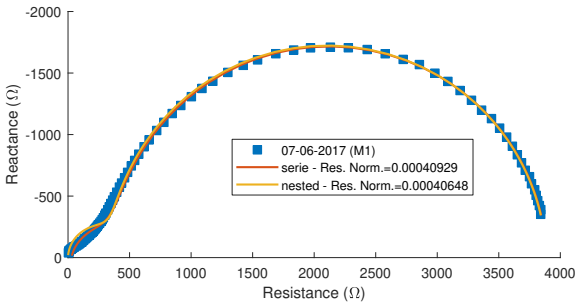

Figure 6.11: An impedance spectra collected on the AD film with the Cr electrode together with 2 fits using 2 different layouts for the EC.

Element	**Series EC**	**Nested EC**
R_0 (Ω)	27.48	0
R_{out} (Ω)	3514	3886
Q_{out} (Ω)	3.277E-8	3.681E-8
n_{out} (Ω)	0.9818	0.9803
R_{in} (Ω)	347.4	361.8
Q_{in} (Ω)	4.524E-10	1.005E-8
n_{in} (Ω)	0.8469	0.9923

Table 6.1: Values of the parameters used to obtain the two fits in Figure 6.11. R_0 is a (small) resistors in serie with the main part of the EC (very common; used to account for cables and similar things); R_{out} refer to the outer resistors in the nested circuit, while R_{in} to the inner one. In the serial circuit, "in" and "out" components can be swapped for Equation 6.9.

6.3.3 DC Bias effect

As already stated, IS is a technique to measure the response of a system while varying the frequency of the AC signal applied to it. However, many commercial systems, allow to superimpose this AC signal with a DC one. This DC signal is often called bias because it rigidly shifts the voltage up or down, without modifying its shape.
The instrument used allowed the application of up to $\pm$40 DC V, however often a so great displacement is not required and few (i.e. 1) V are enough to reach the plateau limit of the device as it can be seen in Figure 6.12.
This plateau is even more evident when looking at the values of the parameters coming from the fits (reported in Figure 6.13), that in this case included three resistor/CPE couples: for example, C_2 and C_3 components stabilize after the bias applied exceed $\pm$3V. In the same bias range, the R_1 value become similar, if not smaller, to R_2 and R_3 which shows just a weak dependency to the bias. The pulsation constant ($1/\tau_c$) stabilized a bit later, together with the linear regime of the current intensity (obtained

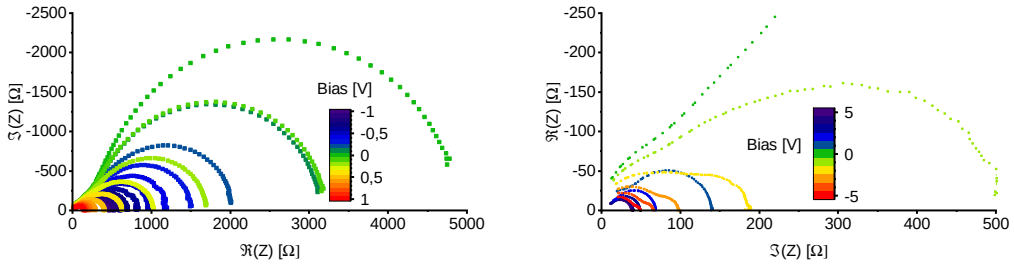

(a) (b)

Figure 6.12: Impedance spectra collected on the AD sample with Cr as top electrode and under a DC bias. (a) spectra with small ($|\text{bias}| \leq 1$V) stress applied; (b) spectra with stronger ($|\text{bias}| \leq 5$V) stress applied.

from the ratio between the applied bias and the measured resistance). The fact that the resistance and the intensity regime changes appear to be de-synchronized is just due to the fact that the two scales are different (respectively logarithmic and linear). The phases of the CPEs are always close to +1 (so the CPEs are similar to capacitors) and have a very high uncertainty, so they are not shown.

The second and the third couple are similar in shape and resistance and less than an order in magnitude different for as concern the capacity. The R_1/CPE_1 couple is instead very different: the drop in resistance is over two order of magnitude (in opposition to just a factor 3 or so of the previous discussed components) and the shape of the capacity is asymmetric. Moreover, this shape is very similar to C-V curves collected on standard MOS capacitors. As usual for these analysis, the positive electrode was attached to the metal (usually called "gate") and the negative to the silicon substrate ("body"). The used silicon substrate was p-doped, however, the accumulation region seems to be located to positive bias, like in n-type MOS capacitors. For these and other test we believe that the NPs inside our films should have an n-type behaviour. This is in accordance to the known possible doping of the beta phase of gallium oxide (no p-type conducibility have been reported on such phase) and can be due to oxygen vancies, as observed in many oxides, or due to Ge and/or Si contaminations ([63]), both of which can happen in our films.

The symmetry of the other two components let us think that they arise from local phenomena, i.e. NP/matrix interfaces or charging effects inside the NPs themselves. The higher pulsation constants (lower characteristical times) support this hypotheses suggesting faster mechanism and thus short range changes. Despite the different frequency ranges at which the effects take place, all the I-V curves have a shape corresponding to the ones observed in asymmetric back-to-back Shottky-Barrier-

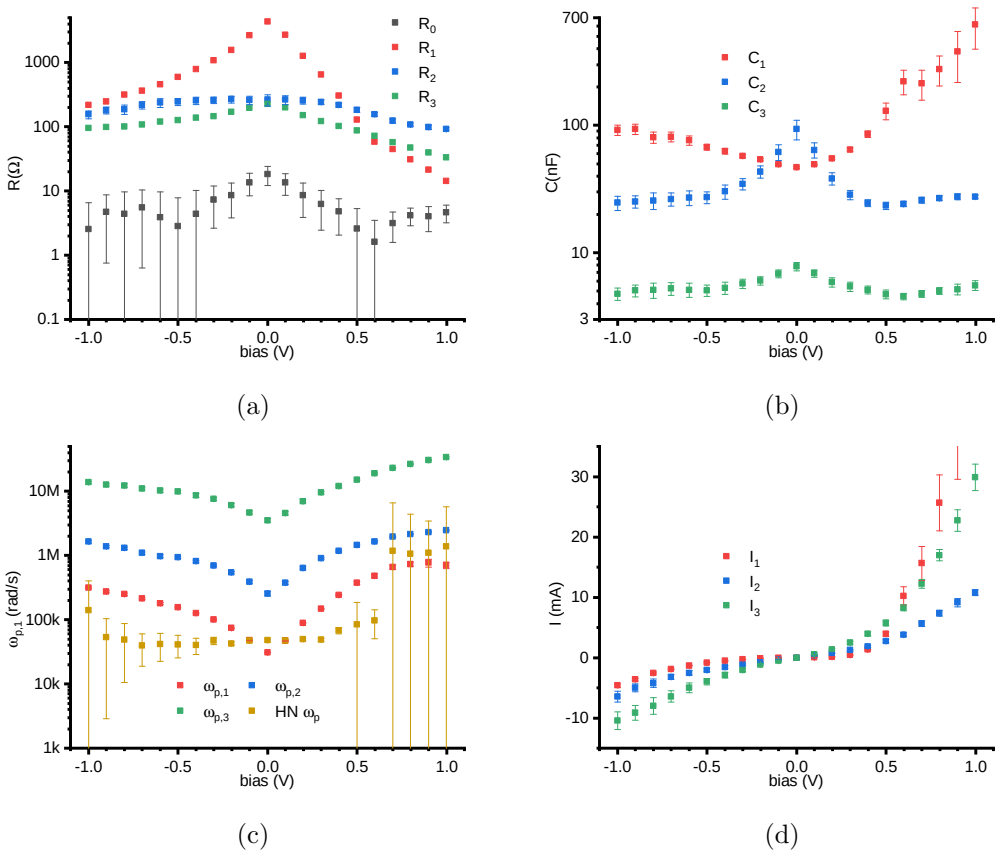

Figure 6.13: Parameters obtained by fitting the curves in Figure 6.12a with an EC made of 3 resistor-CPE couples (and an additional resistor, R_0). (a) the values of the resistances, (b) the values of the CPEs intensities, (c) the values of the pulsation constant (reciprocal of the time constant; here HN ω_p refer to the fitting method presented in section 6.4) and (d) the current intensities calculated as the ratio between the applied bias and the fitted resistances.

Diodes (SBD)[64].

6.3.4 Temperature effect

The second main electrical characterization on such devices was an investigation of the effect of the external temperature on the impedance. The devices had to be mounted inside a cryostat (in particular an Oxford Instrument MicrostatHe [65]), so new connections had to be made and thus the stressless impedance changed a lot. The characterization has been performed between the minimum temperature reachable with liquid nitrogen cooling (∼78K) up to a mild warming over room temperature (350K) and we collected a spectra every 25K on three different biases, so to confirm also the DC electric field dependency over the whole temperature range. In Figure 6.14 I'm reporting them.

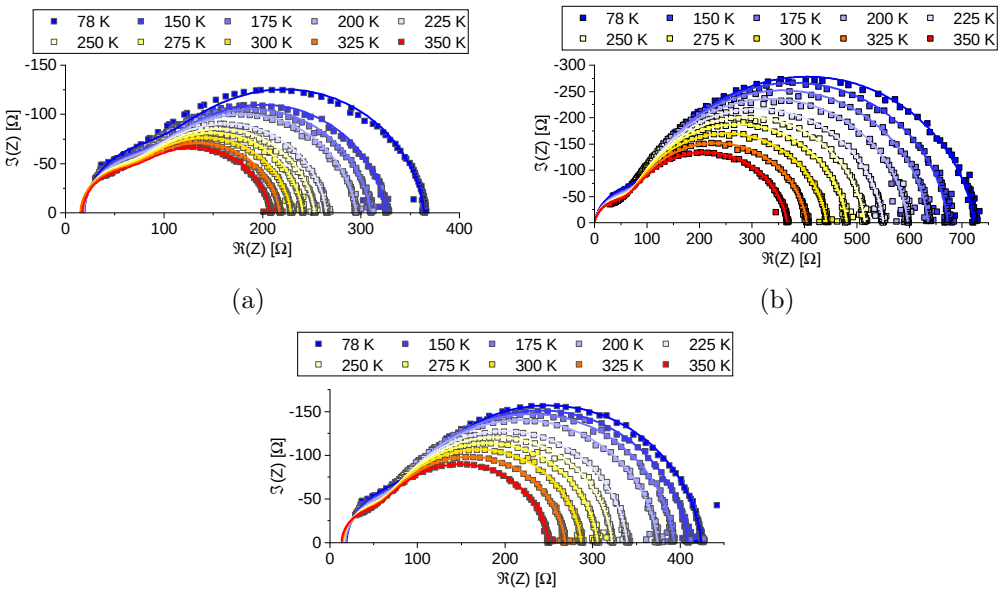

Figure 6.14: Impedance spectra collected on the AD sample with Cr as top electrode and at different temperatures and bias: (a) applied bias was -0.6V, (b) no external bias was applied and (c) at +0.6V.

In all the cases, the impedance decreases at higher temperatures, especially the one coming from the low frequency components, while the high frequency seems to be more stable. When a bias was applied, a wider gap between the spectra collected at 200K and 250K appears, while without any bias the serie of spectra is more evenly distributed.

Another important difference respect to the previous measurement is the fact that

we couldn't close the high-frequency circle, despite using the same frequency range (100Hz-1MHz). This negatively affects the quality of the fits, so much that for the series without the DC field applied, the value of the R_0 element was set as 0Ω and kept fixed during the fit process. In this case a model with just 2 R/CPE couples was used again. The results of these fits are reported in Figure 6.15.

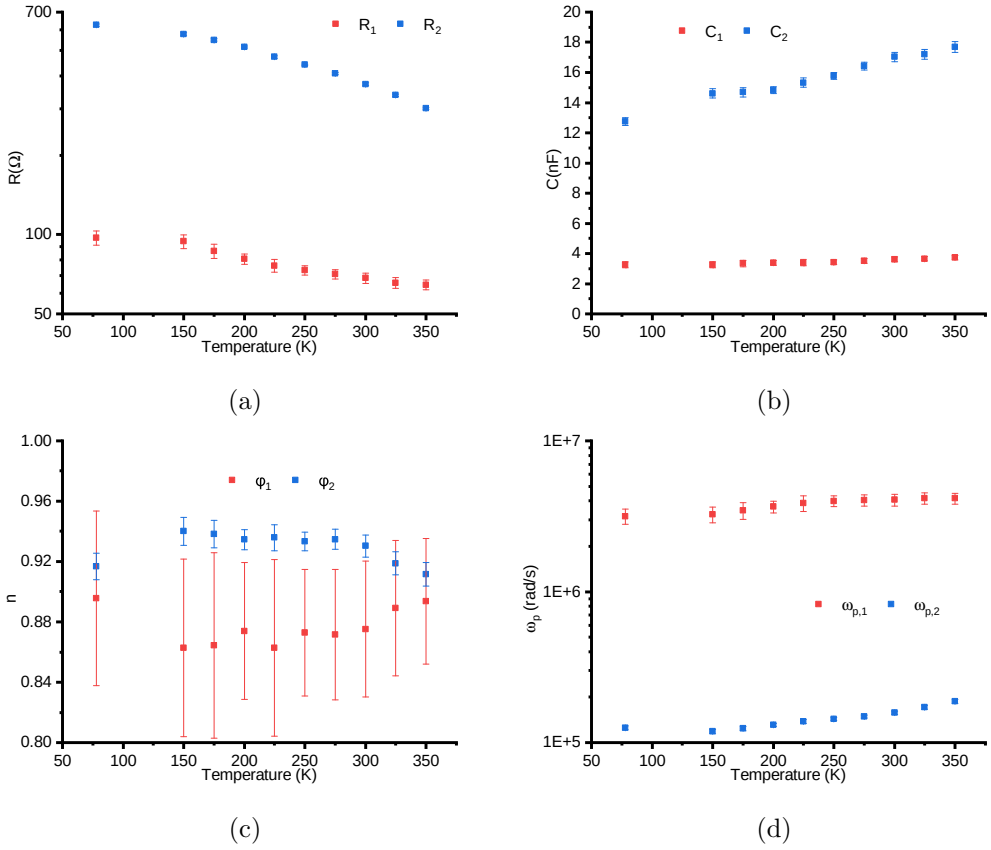

Figure 6.15: Parameters obtained by fitting the curves in Figure 6.14b with an EC made of 2 resistor-CPE couples. (a) the values of the resistances, (b) the values of the CPEs intensities, (c) the values of the CPEs phases, and (d) the values of the pulsation constant (reciprocal of the time constant)

At higher temperatures, the measured resistance (Figure 6.15a) decreased and the capacitance increased (Figure 6.15b) in a weaker way, resulting in a slightly increment of the characteristic pulsation (Figure 6.15d). The effect on the phase of the CPEs (Figure 6.15c) is not well defined, but in general they are more precise and slightly smaller than during the bias measurements. The results obtained with the bias applied are similar, but shifted according to Figure 6.13.

This temperature analysis was carried out to better understand the conduction mechanism inside the films. In particular, according to [66], in case of (fluctuation-

induced) tunnelling the Mott's law apply:

$$R = R_0 \exp\left(\frac{T_0}{T + T_1}\right) \tag{6.11}$$

while if the conduction is by (variable-range) hoping, [67] suggest:

$$R = R_0 \exp\left(\frac{T_2}{T}\right)^{1/4} \tag{6.12}$$

where R_0 are pre-exponential terms that should account for many factors (including the geometry and composition of the sample) and T_0, T_1 and T_2 are constants typical of the mechanism. In our films we found both mechanisms. In Figure 6.16 I'm showing the best fit for each parameter. In particular, the low-frequency, high-value component (R_2) of the impedance acts like a tunnelling, while the high-frequency, low-value component (R_1) is better explained using the hopping theory.

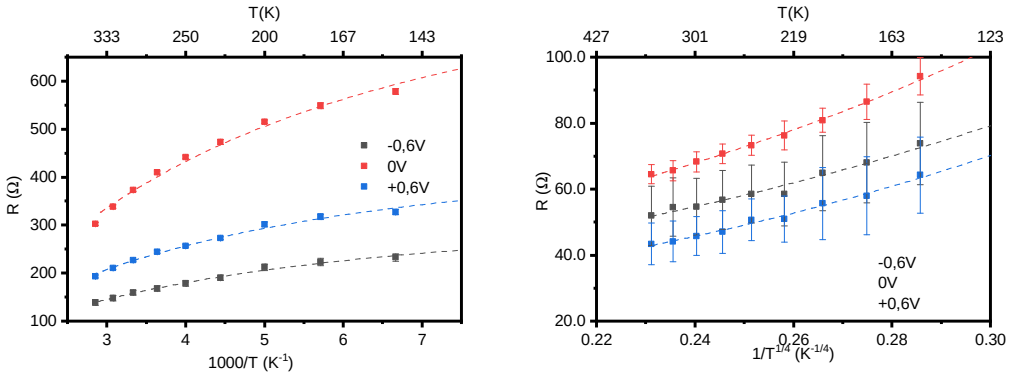

(a) (b)

Figure 6.16: The resistance values presented in Figure 6.15a (squares), but displayed and fitted (lines) according to (a) the Fluctuation-Induced Tunneling theory for the low-frequency (R_2) component and (b) the Variable Range Hoping theory for the high-frequency (R_1) one.

For this reason we hypothesized that R_1 is responsible for the conduction, by hopping, in each phase, while R_2 describe the tunnelling effect that occurs at the interfaces.

6.3.5 Other effects

Other effects investigated were the intensity of the AC field used, the illumination condition and the ageing of the contacts on the impedance spectra.
It has been found that the oscillation level has very little influence on the spectra, and it is basically due to the voltage range around which the impedance is measured

(i.e. for bias=4V and level=100mV, the impedance is measured by averaging the impedance values corresponding to a total electric field between 4.95V and 5.05V). This led to a very small error in the spectra collected without any DC bias, but is completely negligible when any bias is present.
Concerning the illumination (test were performed in room/artificial white light, dark, UV-A and UV-C conditions), the test didn't show any difference at all, probably due to the design of the devices: in fact, the metal layer adsorb almost completely the light, and the thin layer below has a very low absorption coefficient.
Finally, no ageing effect has been recorded after the initial curing effect.

6.4 H-N fitting

6.4.1 Theory

An alternative way to deal with experimental data can be to try to understand and quantify the physical nature of the effect that originates the response instead of giving the practical details of the entire device. Regarding IS in solid systems, the effect under the frequency dependency of the impedance is the way how the system, view as a ensemble of atoms, interacts to the changes in the applied electrical field. One of the milestone in this field was the Debye theory[68] of relaxation in dielectric materials in which he observed that in second approximation (here the first is the DC conduction) each atom respond to such signal by displacing its electron cloud a bit so that the center is not on the nucleus to minimize its total energy in the new condition. However, especially if the atom is between many others, this action requires some times since also the slightest changes in the electronic cloud can have huge effect on local electric field and then on neighbouring atoms. At the end, he stated that the dielectric function of a material can be approximated to

$$\varepsilon(\omega) = \varepsilon_\infty + \frac{\Delta\varepsilon}{1 + \imath\frac{\omega}{\omega_p}} \tag{6.13}$$

where ω is the pulsation ($= 2\pi\nu$), ε_∞ is an high frequency value, $\Delta\varepsilon$ is the strength of such relaxation and ω_p the loss peak pulsation (the inverse of the relaxation time); all of them are typical of each material/system. This relaxation time depends on many factors, but the main is the nature of the solid itself: if the signal is too slow, the energy required to maintain a displaced electron cloud is too high, and so the system prefers to stay in its ground state; if the signal is too fast, the system doesn't have the time to follow it, and in such case the displacement between the actual electron

cloud and the best one would be so high, that it would require more energy than the one gained.

After few years Cole developed two extensions: the Cole-Cole model[69] that accounts for symmetrical stretching thanks to its parameter α and the Cole-Davidson[70] that accounts for asymmetrical stretching thanks to a second parameter called β. Finally, a couple of years later, Havriliak and Negami developed their model[71] by using these two extensions. The final law is:

$$\varepsilon(\omega) = \varepsilon_\infty + \frac{\Delta\varepsilon}{\left[1 + \left(\imath\frac{\omega}{\omega_p}\right)^{1-\alpha}\right]^\beta} = \varepsilon_\infty + \frac{\Delta\varepsilon}{\left[1 + \left(\imath\frac{\omega}{\omega_p}\right)^{m}\right]^{\frac{1-n}{m}}} \tag{6.14}$$

where the right formula is the notation used by Jonscher whom replaced (1-α) with m and (β) with $(1-n)$ and correct this factor by $1/m$.

All the former parameters can vary in the range [0:1] with the extreme denoting particular cases: $\alpha > 0 \rightarrow m < 1$ denote relaxation peaks that are symmetrically larger than predicted from Debye law, usually due to a distribution of elements; $\beta < 1 \rightarrow n > 0$ describes instead peaks not symmetric, often associated to more not resolved contributions.

After the formulation of this law, other advancement/theory have been developed, but they tend to move further away from the Debye law (i.e. Jonsher "universal relaxation law"[62]), losing, from my point of view, the strong link with the underlying physic and their main advantages over the EC study.

One of the best feature about the Debye-based models is that they directly return an important parameter, the relaxation time, that is strongly connected with the oscillating object, so, just by looking at its order of magnitude, accurate hypothesis on the main conduction mechanism of a system can be formulated. However, for a better insight of it, characterization at varying temperature has been performed.

When fitting complex impedance data, is useful to add to these formula the contribution of the low frequency/DC conductibility [72]:

$$\varepsilon_{DC}(\omega) = \frac{\imath \cdot \sigma_{DC}}{\varepsilon_0 \cdot \omega^s} \tag{6.15}$$

with σ_{DC} being exactly the conductibility measurable in DC regime and s a parameter that should account for not ideal behaviour (if ideal it's value is 1). Except for the s parameter, this is exactly the formula used to convert conductibility to permittivity, and according to my fits, s is always very close (if not exactly) 1.

6.4.2 Stressless behaviour

After converting the impedance data to the capacitance space, as in Figure 6.3d, we further process the data so to obtain the intrinsic quantity ε_R (dielectric permittivity) by considering the film dimensions. This, of course, is still a complex number and an example of how its components should look is reported in Figure 6.17.

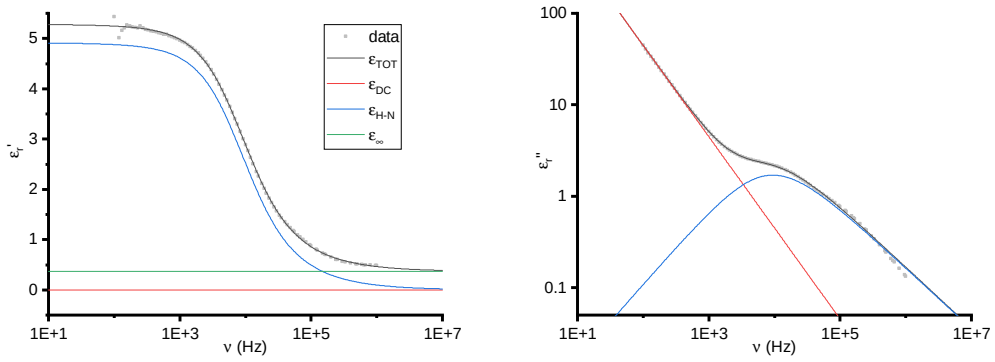

(a) (b)

Figure 6.17: IS data (grey marks), expressed as the (a) real and the (b) imaginary part of the relative dielectric permittivity as function of probed frequency, from the AD film with Cr electrode together with the fit (black line) and its components (coloured lines).

The real component (Figure 6.17a) has a very smooth variation and present two plateau: one, at high frequencies, that is defined as ε_∞ (usually called inappropriately "dielectric constant", while at low frequencies the plateau value is strongly influenced by the Havriliak-Negami (HN) component.
The imaginary part is basically a straight line in the log-log plots ($\propto 1/\nu$) with a deviation due to the dielectric relaxation.

6.4.3 DC Bias effect

The effect of a not-null DC bias can be seen in Figure 6.18.
In these graph the key features of the system are very clear: the different contributions to the conduction/permittivity appear as drops in Figure 6.18a and peaks in Figure 6.18b at different frequencies. The first one, which mainly influences the spectra collected at negative or neutral bias, is centred around 10 KHz while a second one, more defined when positive bias were applied, happen at around one order of magnitude higher frequencies. This dualism is the effect that led to the asymmetric behaviour already commented and that in these graph also influences the low frequencies values.

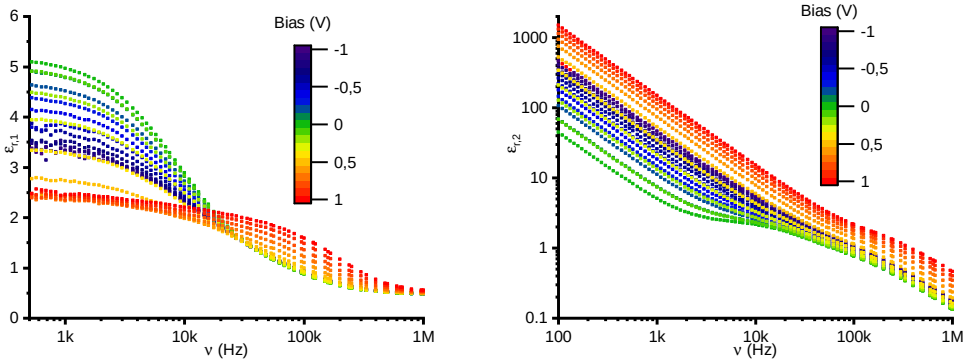

(a) (b)

Figure 6.18: Permittivity data (converted from Figure 6.12a) from the AD film with Cr electrode collected with an applied DC bias between -1V and +1V. (a) real part; (b) imaginary part.

On these graphs, fits similar to that depicted in Figure 6.17 (using just one dielectric relaxation) were performed. The fact that only one contribution was accounted for, could be a limit behind the poor agreement between the experimental data and the model that we found at high frequencies, especially regarding the imaginary part. Despite this limitation, we didn't try to use a 2 peak model because this hypothesis would add other 4 parameters ($\Delta\epsilon_2$, $\omega_{p,2}$, m_2 and n_2) to an already complex equation, with the risk of following some noise instead of the main data.
The results of these fits are reported in Figure 6.19. The shift between the two regimes of the dielectric peak is visible mainly in the peak frequencies (Figure 6.19b), but it also influences all the other peak parameters: the dielectric strength (Figure 6.19a) drops and the broadening parameters (Figure 6.19c and Figure 6.19d) seem to decrease a bit. The permeability at high frequencies (Figure 6.19e) and the parameter s (Figure 6.19g) are almost insensible to the applied bias, while the conductibility (Figure 6.19f) shows two asymmetric linear behaviour, probably due to the fact that we are operating a diode-like device in direct and reverse mode (or two different back-to back SBD).
The observed low value of ε_∞ (down to about 0.3) is due to the fact that the used metal electrode (Cr) is easily oxidized, introducing additional capacitive components to the system but they haven't been accounted for during the conversion from the extrinsic capacity to the intrinsic relative permittivity.

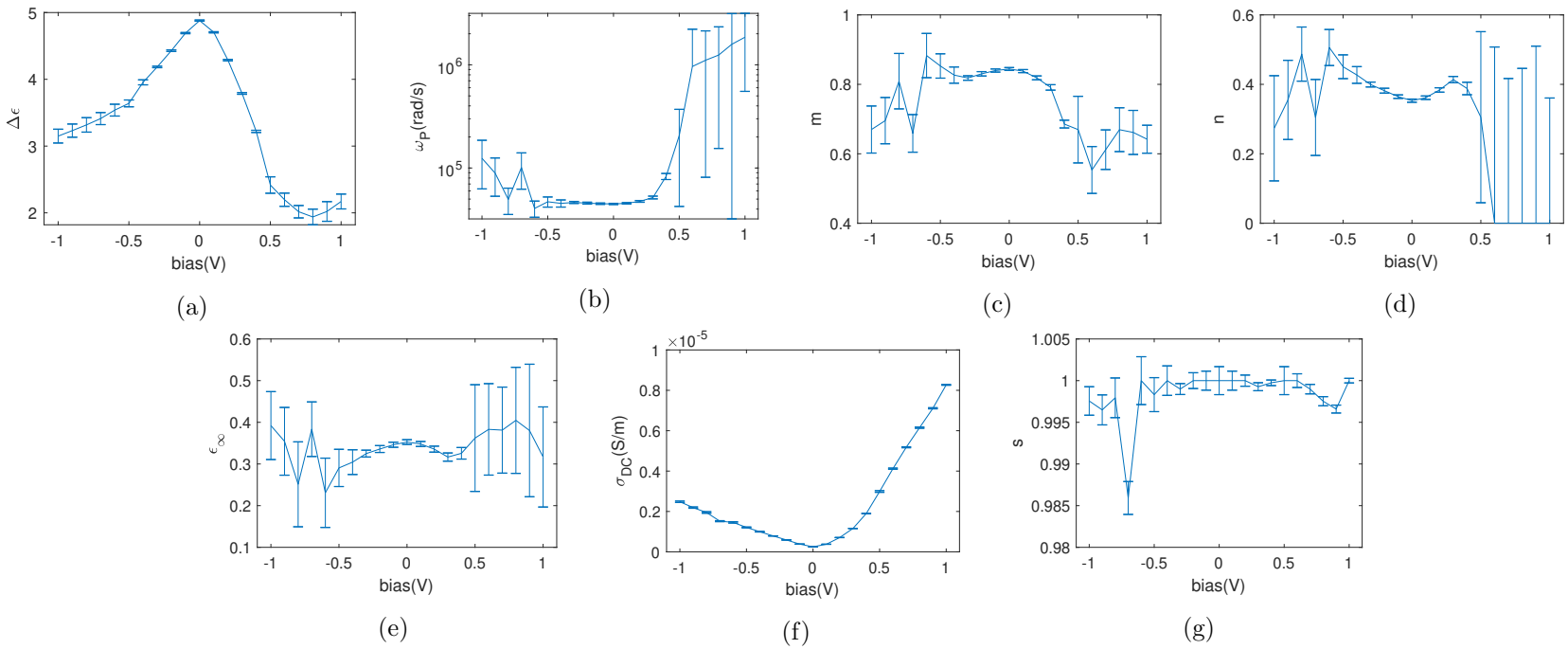

Figure 6.19: Parameters resulting from the Havriliak-Negami fit (together with a DC component) of the spectra shown in Figure 6.18. (a) the ε_r associated with the dielectric peak, (b) the frequency where such peak is centred, (c) and (d) the parameters that define the non ideality of such contribution (in particular they represent respectively the symmetric and asymmetric broadening of the peak), (e) the high frequency relative value of the permittivity (often refereed as relative dielectric constant), (f) the electrical conductivity that the system should show at null frequency and (g) its deviation from ideality.

6.4.4 Temperature effect

We also analysed trough the HN model the data taken at different temperatures presented in subsection 6.3.4. They are reported (as dielectric permeability) in Figure 6.20. In this representation, the gap in temperatures between 78 and 150K is more visible, especially in the real plot at low frequencies.

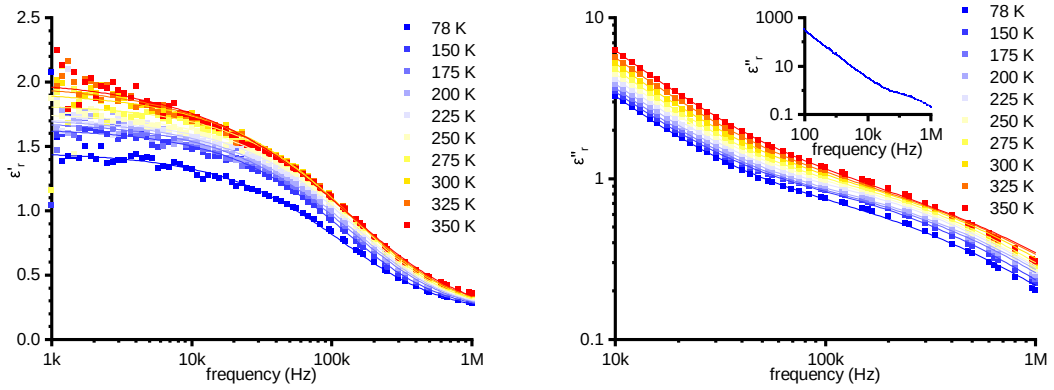

(a) (b)

Figure 6.20: Permittivity data (converted from Figure 6.14b) from the AD film with Cr electrode collected at different temperature. (a) real part; (b) imaginary part.

The fits results are reported in Figure 6.21. Of the many parameters involved, the high frequency permeability (ε_∞, Figure 6.21e) is not influenced neither by the temperature (together with the already discussed stability in DC fields). The same apply to the exponents n (Figure 6.21d, this time stable to always exactly 0) and s (Figure 6.21g), with maybe the last one being slightly smaller than measured in air and having some deviation at very low temperatures (but with just one data point we cannot be sure). The HN permeability (Figure 6.21a) and DC conducibility (Figure 6.21f) both depend on the measured conditions, but they increase at high temperatures (instead of having opposite behaviour as seen when monitoring the bias).
The peak pulsation ω_p (Figure 6.21b) remain stable at around $1.3 \cdot 10^6$ rad/s, quite different from the $5 \cdot 10^4$rad/s observed in the bias scan for the neutral field, but similar to the noisy fits at very high bias ($\Delta V \geq 0.6V$) where the peak resonates at over $1 \cdot 10^6$ rad/s. Finally, the m exponent (Figure 6.21c) shows clearly two regimes with the separation temperatures at around 250-275 K, corresponding to about 21-24 meV, energy compatible with point defects observed in the bulk[7]. Once that the presence of these two regimes is known, hints of them can be found also in other parameters, like the HN permeability and the DC conductibility.

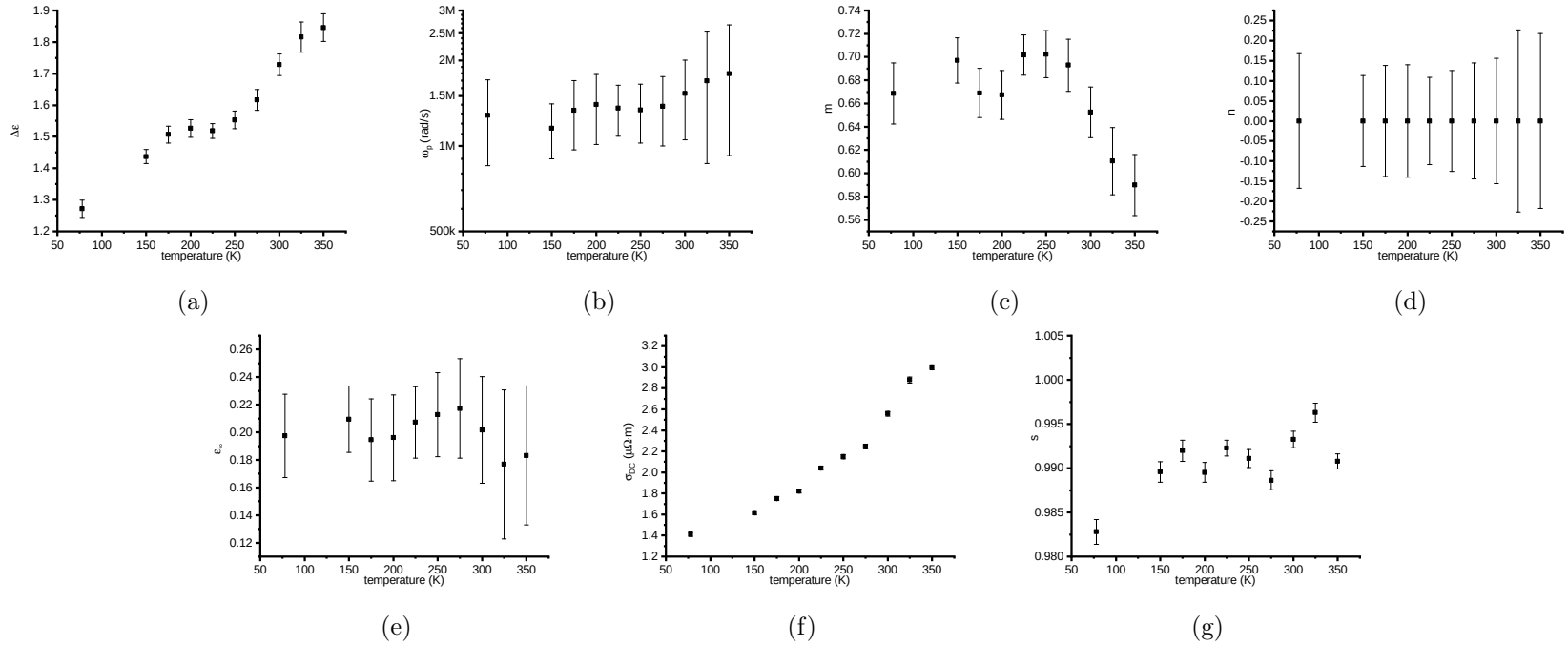

Figure 6.21: Parameters resulting from the Havriliak-Negami fit (together with a DC component) of the spectra shown in Figure 6.20. (a) the ε_r associated with the dielectric peak, (b) the frequency where such peak is centred, (c) and (d) the parameters that define the non ideality of such contribution (in particular they represent respectively the symmetric and asymmetric broadening of the peak), (e) the high frequency relative value of the permittivity (often refereed as relative dielectric constant), (f) the electrical conductivity that the system should show at null frequency and (g) its deviation from ideality.

6.5 Electrical plasticity

6.5.1 Theory

One of the possible application of these nanostructured materials consists in advanced memories with peculiar properties. For example, it has been found out that the devices described in this work change their resistivity according to previous electrical stimuli, but just for a given time, and they return to their standard state. This behaviour is similar to the memresistivity found on other materials, but it differentiates from it since the change in resistivity is only momentary and it doesn't last until another "write" operation.

This intermediate behaviour is often called electrical plasticity since, like in elastomers, the system recovers its state in a given amount of time, but in the meanwhile it's slightly different. This property can be used to implement hardware-based artificial synapses that work simulating the Spike-Timing Dependent Plasticity (STDP) process which biological neurons are based on[73].

Thanks to the fact that in our equipment the DC bias signal can be precisely adjusted also by sending proper commands via a PC, we can test what is the response of the system when a signal as the one depicted in Figure 6.22[74] is applied. This kind of signal simulates the transmission of informations across a neural synapse: the first spike represents the electric field due to the change in the pre-synaptic neuron, while the second the effect such change will generate in the post-synaptic one. Usually, in a biological environment, these two signal arise from two opposite side of the synapses and have the same sign, but since in the artificial equivalent, this signal must be sent by an instrument on which one electrode potential is constant, when simulating it the second spike should be opposite in sign and equal in the charge moved (area under the curve itself).

This signal can be defined by 3 quantities: the pulse period/width (T), the pulse intensity (I) and the delay between the two pulses (D), that is negative when the optional pulse arrives before the other. The impedance has been measured (as parallel capacitance, C_p, and resistance, R_p) just before the first cronological pulse and just after the second, where the orange arrows are pointing at. Other (not investigated) options are to shift the whole signal up or down by imposing a flat bias, or measure the impedance by changing the AC field level.

According to the model, the system modifies its state after that two complementary spikes interact with it. The system should be then different than before, and this difference depends on the delay between the two spikes (or their order).

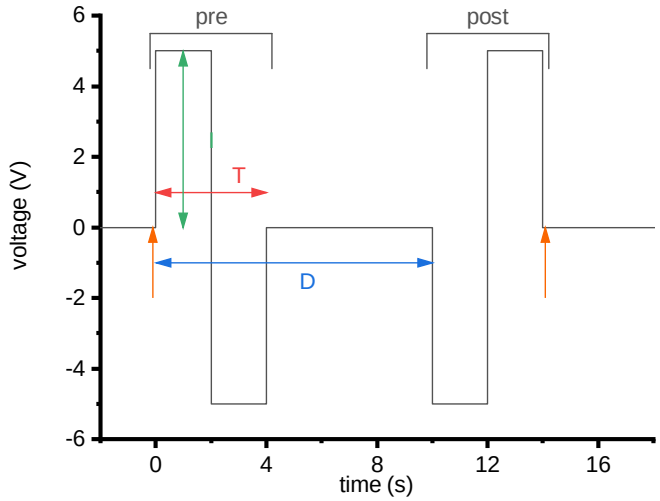

Figure 6.22: The signal seen by synapses-like system during the transmission of an information after square-waves approximation.

6.5.2 Results

The main pre-requisite for having any electrical plasticity is the presence of some electrical hysteresis inside the device. More-over, this hysteresis has to depend on what had happen before to the device itself. To test for the presence of both phenomena, multiple subsequent C-V curves (alternating rising and falling bias signals) have been acquired on the films, both by repeating the positive (in Figure 6.23b), the negative (Figure 6.23a) and the alternated bias scans.
When the scan was limited to either the positive or the negative region, some hysteresis cycles appear, indicating that some charges accumulated during the increasing bias sweep cannot be removed by simply removing the electrical stress. This means that at least part of the charge carriers remain trapped somewhere. The amount of these trapped carriers can be estimated through the formula:

$$n(V) = V\frac{C_{down}(V) - C_{up}(V)}{|e|} \tag{6.16}$$

with $C_{down}(V)$ and $C_{up}(V)$ representing the capacity values at a given voltage for respectively decreasing and increasing steps. The results of these conversions are visible in Figure 6.23d when a positive voltage was applied to the metal and in Figure 6.23c when at the metal there was a negative charge.
The second prerequisite condition was confirmed by the fact that subsequent scans show a decreasing capacity. This is obvious regarding the second raise (for already discussed reasons: trapped charges), but the fact that also the subsequent scans are

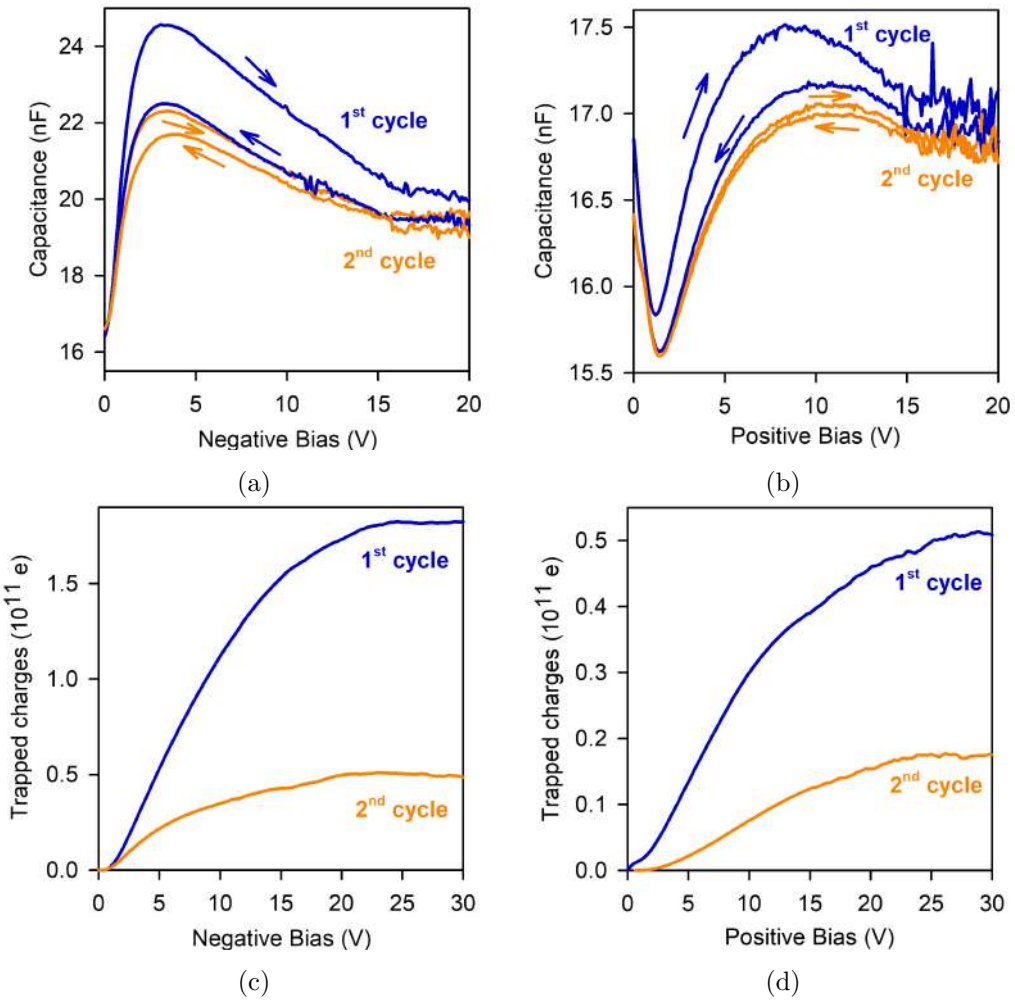

Figure 6.23: The effects of performing multiple C-V cycles on the films: C-V curves measured at (a) negative and (b) positive bias (applied to the metal electrode) show some hysteresis that have been explained as trapped charges during (c) negative and (d) positive cycles.

affected suggest that the trapping process is not completed during the first scan but that it can continue. It has also being found out that changing the sign of the applied voltage has the effect to "clear" the memory, restoring the initial value of the capacitance.

According to [75], the same effect can be expected also on the resistance/current intensity, but we didn't found any appreciable effect in such direction.

Nevertheless we prosecuted the test in the artificial synapses direction, applying signals according to the scheme in Figure 6.22. The results, expressed as the ratio of the values measured before sending the pulses train divided by the same values measured just after it (X_{before}/X_{after}), have been analysed in graphs like Figure 6.24 where

different conditions can be compared (the details of the measurement conditions are reported in the figure caption; i.e. in Figure 6.22 we can follow the effects of changing the number of pulses, the delay between them and their period).

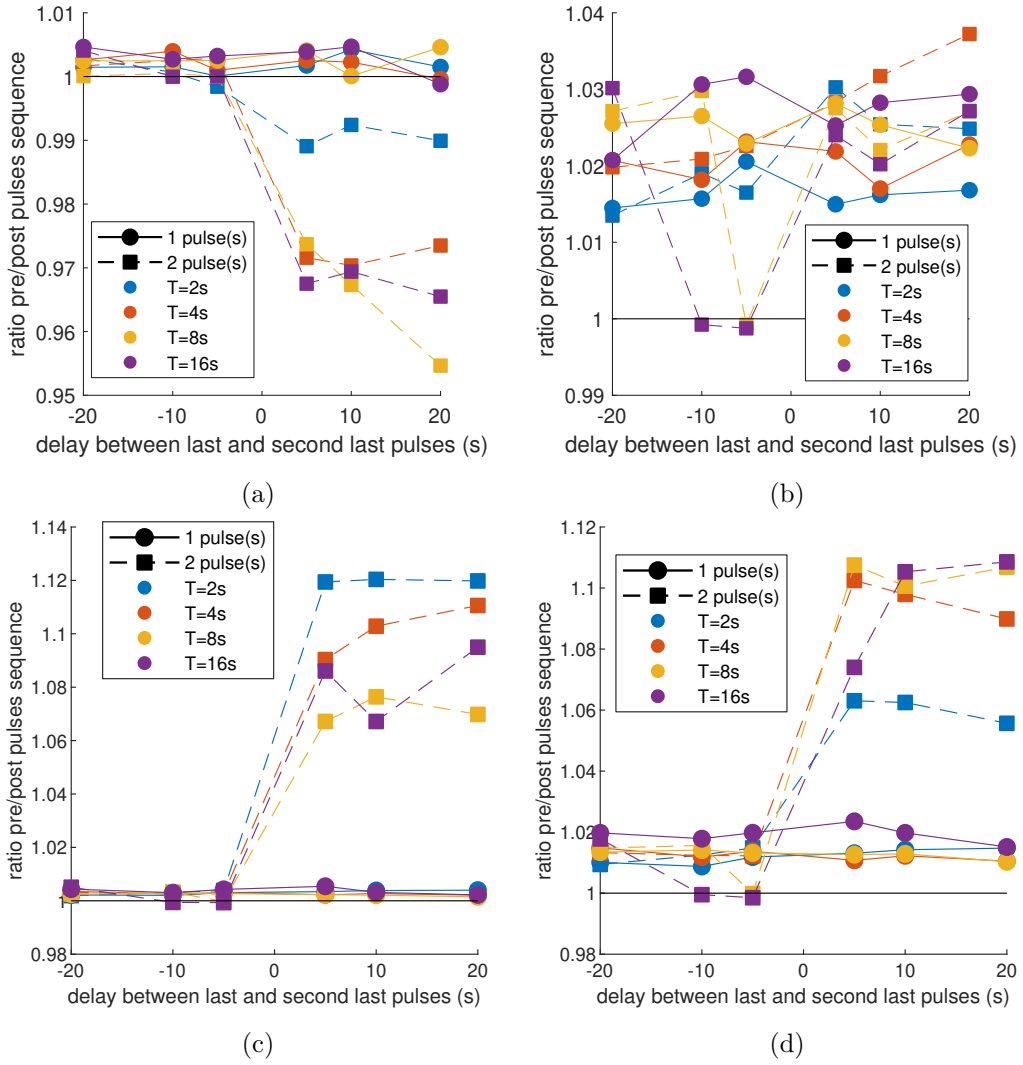

Figure 6.24: STDP data collected on the AD film with Au electrode. Every point consist in an averaging of up to 10 single measurements (few resulted in errors so they were ignored). Every measurements consisted in a train of pulses according to Figure 6.22 where the voltage of first half of the always present pulse was 5V and each pulse had a period according to the legend. To measure the impedance, an AC signal of 100mV was used. Two frequencies have been measured: (a) and (b) 6kHz and (c) and (d) 600kHz (corresponding to the characteristical times of the two contributions seen in IS). On these, the impedance was collected as (a) and (c) parallel capacitance and (b) and (d) parallel resistance.

Our capability to differentiate between the two contributions allowed us to attribute the STDP effects to a specific process: when probed at low frequency (6kHz), the devices show a decrease in their capacitance (Figure 6.24a) and nothing at all in

the resistance (Figure 6.24b). At opposite, when probing the impedance at higher (600kHz) frequencies, both the capacitance(Figure 6.24c) and the resistance (Figure 6.24d) are greatly influenced by the presence of the two pulses. This let us think that, according to what discussed in section 6.3.4, the memory effect is ascribable to polarization effects inside the NPs.

According to [74], STDP devices should behave symmetrical respect to the delay between pulses (that mean if pulse A arrive before or after pulse B), but as it can be seen in Figure 6.24, we observe changes only in one direction. We justify this difference since our device is not symmetric (we use a MOS geometry while the cited authors have a MOM device) and due to the fact that our NPs support only the n-type doping.

Another important fact, is that we need a minimum duration for each pulse to observe the effects described: Figure 6.24a and Figure 6.24d clearly shows that when the pulses had a period of 2 seconds, they could not completely "write" the devices, while the differences between periods of 4 and 16 seconds are minimal. Togheter with a study of the "writing time" we also studied the time for which the written information will be available in the devices. To do so, we wait an additional time after the second pulse [2] and then we collected the impedance as before. In Figure 6.25a I'm reporting the results of these tests, together with an exponential decay fit.

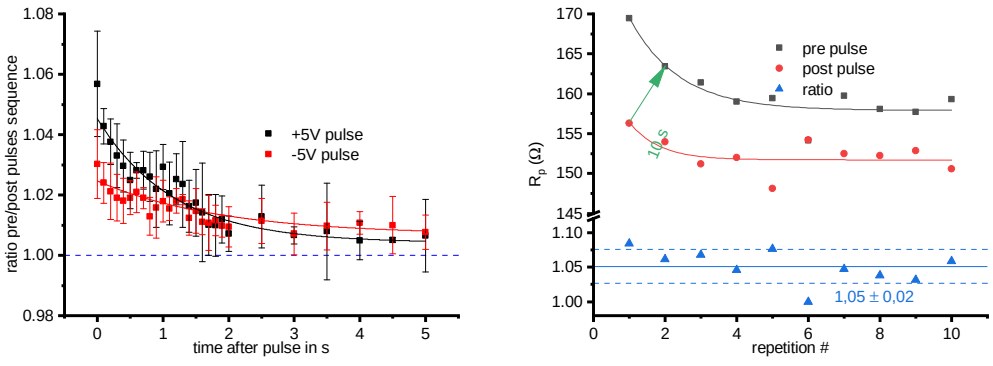

(a) (b)

Figure 6.25: Study of the STDP values evolution in time: (a) the life time of the STDP information (how much time do we have to read the information after it has been written) and (b) the effect that multiple write operations have on such signal.

These fits returned a decay time of 1.15 ± 0.12s for the pulse train that was characterized by the first half of the first pulse of +5V and 1.9 ± 0.8s for the inverted pulse train

[2] In practice, this was achieved by adding a third fake pulse with intensity of 0V just after the second one.

(-5V). This time is indeed something related to the STDP effect since the natural decay of R_p signal, calculated from Figure 6.25b, resulted in about 10 times longer times (14±5 s for the values before the pulses and 8±9 s for the values collected after them).

6.6 Software development

6.6.1 Data acquisition software

All the electrical data presented in this chapter, together with many more (> 5000 IS spectra and hundreds of pulses for what concern the electrical plasticity characterization) have been acquired using a custom software developed in LabView® for such purpose. The objective of this software was to acquire lots of data (i.e. tens or hundreds of spectra) by performing the same measurement (i.e. the same frequency scan) at slightly different conditions (bias, level,...).
More in the specific, the software have the function to prepare the instrument for each measurement (by setting all the conditions decided by the user), coordinate the data acquisition (tell the instrument to move to a new scan point, start the acquisition, wait for the correct time, retrieve the data from the instrument) and save the data in some ordered format (i.e. a table in plain text). All of these while offering a Graphical User Interface (GUI), some feedback of the measurement (both as the single data point values and as real time updating graphs), some easily way to allow the user to customize the measurement (the measurement parameters could be set starting from an external file or from the software itself) and other minor functions (i.e. data correctness check, error report and end of measurement notification).
The software just described is now used by different groups inside the department for their work.

6.6.2 Data analyses software

As described in section 6.2, the analysis of IS data through the use of an EC is not trivial and often is not interesting to know the explicit formula for the circuit in interest (or perhaps, if its some routine analyses, the operator don't know how to derive it). For this reason, there are nowadays many dedicated software available for dealing with it. Unfortunately, the majority of them are either:

1. developed by private companies that sell their licenses for a quite high cost (often not sustainable by research group not focused in the IS field) and/or allow only the user of their equipment the access to them [76, 77, 78];

2. quite old software, very accurate and precise with the results, but also very user unfriendly [79, 80];

3. recent free-to-use (at least for research purposes) softwares with limited functionality and/or poor accuracy [81];

4. softwares that come with weird licenses/way to obtain them.

In particular, what was lacking, was the capability to fit a series of dataset taken in similar but slightly different conditions without manually resetting all the parameters every time and the Debye/HN analysis.
For these reasons I started to move from using (a selection of) the specific softwares listed before to the MATLAB® environment where I can code and use all these features. Later on, when I realized that these were not just my problems, I decided to improve the code and publish it.
What Easy IS[3] (will) feature is

- compatibility with different data file formats (both as input and output);
- a complete set of tool to visualize the IS data in the different spaces show in Figure 6.3;
- the ability to use just a subset of data point for the other operations, without changing the original file;
- quality and dissipation factors spectra;
- data quality check via Kramers-Kronig relations;
- evaluation of the Distribution of Relaxation Times (DRT);
- EC and HN fit routines;
- a survey tool to look for different local minima in the fit parameter space before starting the fit process itself;
- exporting the spectra from fit results or from simulating completely new system;

[3]Provisional name.

- batch process to deal with large series of file;
- analyses of variation in the condition (including fit results) over such series;
- the possibility for the final user to define their own ECs or file formats (this last part only via coding) and eventually to share them in future releases of the software;
- a (somehow) user-friendly Graphical Use Interface (GUI) and the possibility to do all the operations also from the command-line (source files only);
- all the required help files (including a wiki, a manual, comments and documentations for the code).

All of this would be available both as MATLAB® source code and as executable for various platforms.

Chapter 7

Final remarks

7.1 Conclusion

7.1.1 Film preparation

In this work we used successfully the RF-sputtering to obtain thin films with thickness of up to about 130 nm (for 60 minutes long depositions) that can be controlled thanks to a constant yield of about 2.2 nm/min over a large range of deposition durations and hence thicknesses.
It has been found that these films are dense, in the sense that they do not have any pores in them, and thus have an high optical quality as it has been shown both in term of macroscopical effects (high transmission and reflection, low scattering and adsorption) and microscopic aspect. This high quality is also kept during the thermal treatment, step that is necessary for obtaining controlled regions rich in gallium oxide, the active element of our material.
However, we also reported that this technique has some problem, in particular when thicker samples are needed: in that case, the film must be grown with multiple depositions and this process introduce some regions between a layer and the next one where pores of µm can form during the thermal treatment, lowering the density of the films (increasing thickness) and the optical quality (scatter effect). A partial solution can be to anneal the films at mild (600°C) temperatures for one night between each deposition.

7.1.2 Film morphology

The morphology of the films have been investigated using different techniques, including microscopy imaging (optical, electronic and atomic force), x-ray reflectivity, small angle scattering and diffraction.

The results confirm that the films consist in two different phases: an amorphous matrix and crystalline nanoparticles rich in gallium. The crystals have been identified as a cubic F d$\overline{3}$m phase, however a distinction between $LiGa_5O_8$ and γ-Ga_2O_3 cannot be performed due to many spurious contributions. This is true for the TT samples, similar to what was observed in the bulk, but also for the AD ones (however, in this case, the crystal fraction and the crystal domains are lots smaller). The later occurs even in AD samples, by variance with the bulk, and this is likely related to the fact that, during the deposition, the clusters of atoms impact the substrate with kinetic energy high enough to allow the diffusion of atoms, that are then able to induce the nano-phase/matrix segregation. Another difference from the bulk that emerged during SAXS is the fact that the shape of the NPs appear to be lenticular instead of being spherical.

Analysis of XRR data somehow agree with this theory, telling us that these NPs are concentrated near the film surface (where the atoms can diffuse a bit also after the finish of the sputtering process) and in smaller measure also near the interface with the substrate. The second preferred location can be explained trough AFM height and phase mapping on very thin films (1 nm): on this sample we found some terraces of about 3 nm with a phase different from the background, indicating that the growth of the film is initiated by the formation of some islands.

XRD data let us monitor the effect of the thermal treatment, and of its two parameters (temperature and duration) on the NCs: in general, the longer and the hotter the treatment is, the more and larger the NCs are. Thanks to Grazing-Incidence measurement we can say that these crystals should be more or less spherical.

Last but not least, confronting the size obtained with the different techniques, we believe that each NP is composed of many crystals fused together. There exist two possibilities that explain this finding: the first is that the NCs group together incorporating some matrix (maybe richer in γ-Ga_2O_3) between them, while the second possibility is that we form a single crystalline entity, but with many small crystal domains. In both case, at the interfaces between phases, an amorphous region still rich in gallium is probable.

7.1.3 Electrical response

Starting from the films, some Metal-Oxide-Semiconductor capacitor-like devices have been built and characterized. In this work I showed the effect of an external static electrical field and of the measurement temperature on them. The raw data have been studied according to different theories, in particular the study of the dielectric

relaxations and the modellization through an equivalent circuit have been shown. These analysis allowed us to understand that, other than the DC effect, several processes contribute to the conduction. Moreover, each of these processes show a distributed response, suggesting a distribution of structural features, interpreted as the size of the NPs and the distances between them. According to this interpretation, the knowledge obtained from the morphology studies and eventually complemented with additional informations (i.e. average number of NPs stacked vertically in the film), can help to characterize deeply the prototypes, eventually leading to improved performances in next generation devices. The other results discussed in 7.1.2 can also lead to minor effects on the electrical properties. For example, the fact that the film is not homogeneous on the large scale in the out-of-plane direction imply the fact that the voltage drop rate should also change, and thus that eventual breakdowns will form prevalently in some regions instead of others. Finally, also the anisotropy of the NPs can play a role in the conduction: in fact, for the reasons already mentioned, the in-plane and the out-of-plane conductibility are expected to be slightly different. The resistances associated with these components behave like asymmetric back-to-back Schottky Barrier Diodes (SBD). The presence of the diodes-like behaviour is due to the fact that we are probing semiconductor barriers (matrix-matrix, matrix-NP and NP-NP). However, our film, which likely sustain electric conduction by electrons (either originated from oxygen vacancies or Si/Ge incorporation), is built on a p-silicon substrate leading to an overall asymmetric device and thus an asymmetric response. According to the temperature behaviour we could attribute the low frequency contribution of the conductivity to tunnelling mechanisms at the matrix-NP interfaces, while the high frequency one to hopping processes inside each phase. As a final part of the investigation on the electric response of these systems, we have analysed our films as potential candidates for artificial bio-inspired memories trough the STDP mechanism and the test confirms this possible application.

7.2 Future perspectives

7.2.1 Film preparation

As already stated in subsection 7.1.1, we solved the problem regarding quite thick films, but at the expense of the actual daily yield. According to some literature[82], the same effect could be obtained also trough an in-situ annealing during the deposition, so from my point of view, this could be the first step to improve. Alternatively, other way to obtain films could be investigated (i.e. dip coating from

the melt).
For what concern the composition, instead, it would be interesting to study if all the effects here attributed to the presence of the gallium are indeed due to it. For so, analysis of gallium-free samples would be great. Another test could be to test lithium-free samples (so to definitely discriminate between the γ-Ga_2O_3 and the $LiGa_5O_8$ possible crystalline phases). However for doing so one should remove the starting oxide from the bulk recipe, changing drastically the already critical viscosity of the melt and hence the feasibility of quite big bulk slabs.
On the opposite, adding new dopant elements or changing the concentration of the already present one, could change the energy levels of the films and thus the possible applications of the final devices. This could be done by either producing different targets or by thinking to some co-deposition methods starting from a dopant-free and a dopant-pure precursors (this way should be cheaper and faster, but adequate equipments are needed).

7.2.2 Film morphology

In this work we concentrated on the possible electrical application of our film, but the presence of numerous pores can also be an added value for some applications, in particular, if they are "open"[83], they greatly enhance the sample surface and thus they can be use as catalysts. In particular, thanks to the wide band-gap of the gallium oxide, possible application in the water splitting technology[84] can be interesting to test.

7.2.3 Device fabrication and electrical characterization

As the title of this section suggest, one of the key aspect to improve is the quality of the devices. In particular, the tested generation of devices lacks in reproducibility due to the poor contacts: these were made using products intended for digital prototyping objects, while more reliable analogue connections (starting from proper bonding on specific holders and then dedicated acquisition boards to connect them to the instruments) are strongly suggested.
Once this requirements are met, better optimization of the injection mechanism can be performed. According to the literature[85], a good starting candidate could be the Ti/Au electrode, eventually with also layers of aluminium and/or nichel.
Another aspect that can be improved is the geometry of the device: artificial synapses

require the symmetry of the interfaces, so symmetric systems, i.e. metal/oxide/metal (MOM) should be designed.

Bibliography

[1] Harini Sosiati SUDARMINTO et al. "Segregation of Tin Oxide in Oxide Layer of Zircaloy-type Alloys". In: *Journal of Nuclear Science and Technology* 39.2 (Feb. 2002), pp. 150–155. DOI: 10.1080/18811248.2002.9715168 (cit. on p. 1).

[2] Alberto Paleari et al. "Tunable Dielectric Function in Electric-Responsive Glass with Tree-Like Percolating Pathways of Chargeable Conductive Nanoparticles". In: *Advanced Functional Materials* 20.20 (Aug. 2010), pp. 3511–3518. DOI: 10.1002/adfm.201000449 (cit. on p. 1).

[3] Sergio Brovelli et al. "Fully inorganic oxide-in-oxide ultraviolet nanocrystal light emitting devices". In: *Nature Communications* 3.1 (Jan. 2012). DOI: 10.1038/ncomms1683 (cit. on p. 1).

[4] Sébastien Chenu et al. "Tuneable Nanostructuring of Highly Transparent Zinc Gallogermanate Glasses and Glass-Ceramics". In: *Advanced Optical Materials* 2.4 (Feb. 2014), pp. 364–372. DOI: 10.1002/adom.201400007 (cit. on p. 1).

[5] S. J. Pearton et al. "A review of Ga2O3 materials, processing, and devices". In: *Applied Physics Reviews* 5.1 (Mar. 2018), p. 011301. DOI: 10.1063/1.5006941 (cit. on p. 1).

[6] Masataka Higashiwaki et al. "Development of gallium oxide power devices". In: *physica status solidi (a)* 211.1 (Nov. 2013), pp. 21–26. DOI: 10.1002/pssa.201330197 (cit. on p. 1).

[7] Vladimir N. Sigaev et al. "Light-emitting Ga-oxide nanocrystals in glass: a new paradigm for low-cost and robust UV-to-visible solar-blind converters and UV emitters". In: *Nanoscale* 6.3 (2014), pp. 1763–1774. DOI: 10.1039/c3nr05210a (cit. on pp. 1, 3, 111).

[8] S. V. Lotarev et al. "Broadband infrared light-emitting patterns in optical glass by laser-induced nanostructuring of NiO-doped alkali-gallium germanosilicates". In: *Optics Letters* 38.4 (Feb. 2013), p. 492. DOI: 10.1364/ol.38.000492 (cit. on pp. 1, 3).

[9] M. Razeghi. "Short-wavelength solar-blind detectors-status, prospects, and markets". In: *Proceedings of the IEEE* 90.6 (June 2002), pp. 1006–1014. DOI: 10.1109/jproc.2002.1021565 (cit. on p. 1).

[10] Ming-Gang Ju et al. “Tuning the energy band-gap of crystalline gallium oxide to enhance photocatalytic water splitting: mixed-phase junctions”. In: *J. Mater. Chem. A* 2.40 (Aug. 2014), pp. 17005–17014. DOI: 10.1039/c4ta03193h (cit. on p. 1).

[11] Jürgen Schmidhuber. “Deep learning in neural networks: An overview”. In: *Neural Networks* 61 (Jan. 2015), pp. 85–117. DOI: 10.1016/j.neunet.2014.09.003 (cit. on p. 1).

[12] O. Schalm et al. “Enamels in stained glass windows: Preparation, chemical composition, microstructure and causes of deterioration”. In: *Spectrochimica Acta Part B: Atomic Spectroscopy* 64.8 (Aug. 2009), pp. 812–820. DOI: 10.1016/j.sab.2009.06.005 (cit. on p. 2).

[13] C. J. KENNEDY, K. R. MURDOCH, and S. Kirk. “CHARACTERIZATION OF ARCHAEOLOGICAL ANDIN SITUSCOTTISH WINDOW GLASS”. In: *Archaeometry* 55.3 (Aug. 2012), pp. 465–478. DOI: 10.1111/j.1475-4754.2012.00711.x (cit. on p. 2).

[14] NAKAGAWA K and IZUMITANI T. “RELATIONSHIP BETWEEN PHASE SEPARATION AND CRYSTALLISATION IN LI2O, 2.5SIO2 GLASS AND A LITHIUM SILICATE CONTAINING A LARGE AMOUNT OF TITANIUM OXIDE”. In: *Physics and Chemistry of Glasses* 10.5 (1969). Cited By :28, pp. 179–184. URL: www.scopus.com (cit. on p. 2).

[15] H. W. Safford and A. Silverman. “ALUMINA-SILICA RELATIONSHIP IN GLASS”. English. In: *Journal of the American Ceramic Society* 30.7 (1947). Cited By :18, pp. 203–211. URL: www.scopus.com (cit. on p. 2).

[16] Sumit Vyas et al. “Comparative Study of As-Deposited ZnO Thin Films by Thermal Evaporation, Pulsed Laser Deposition and RF Sputtering Methods for Electronic and Optoelectronic Applications”. In: *Journal of Electronic Materials* 44.10 (June 2015), pp. 3401–3407. DOI: 10.1007/s11664-015-3861-y (cit. on p. 2).

[17] V. N. Sigaev et al. “Nickel-assisted growth and selective doping of spinel-like gallium oxide nanocrystals in germano-silicate glasses for infrared broadband light emission”. In: *Nanotechnology* 23.1 (Dec. 2011), p. 015708. DOI: 10.1088/0957-4484/23/1/015708 (cit. on pp. 2, 20).

[18] N. V. Golubev et al. “Diffusion-driven and size-dependent phase changes of gallium oxide nanocrystals in a glassy host”. In: *Physical Chemistry Chemical Physics* 17.7 (2015), pp. 5141–5150. DOI: 10.1039/c4cp05485g (cit. on p. 3).

[19] Vladimir N. Sigaev et al. “Native amorphous nanoheterogeneity in gallium germanosilicates as a tool for driving Ga_2O_3 nanocrystal formation in glass for optical devices”. In: *Nanoscale* 5.1 (2013), pp. 299–306. DOI: 10.1039/c2nr32790b (cit. on pp. 3, 20, 53).

[20] A. Paleari et al. “Crystallization of nanoheterogeneities in Ga-containing germanosilicate glass: Dielectric and refractive response changes”. In: *Acta Materialia* 70 (May 2014), pp. 19–29. DOI: 10.1016/j.actamat.2014.02.022 (cit. on pp. 3, 8, 20, 64).

[21] Roberto Lorenzi et al. “Augmented excitation cross section of gadolinium ions in nanostructured glasses”. In: *Optics Letters* 42.13 (June 2017), p. 2419. DOI: 10.1364/ol.42.002419 (cit. on p. 3).

[22] Alberto Paleari et al. “Donor-Acceptor Control in Grown-in-Glass Gallium Oxide Nanocrystals by Crystallization-driven Heterovalent Doping”. In: *ChemPhysChem* 18.6 (Jan. 2017), pp. 662–669. DOI: 10.1002/cphc.201601247 (cit. on p. 3).

[23] N. V. Golubev et al. “Nucleation-controlled vacancy formation in light-emitting wide-band-gap oxide nanocrystals in glass”. In: *Journal of Materials Chemistry C* 3.17 (2015), pp. 4380–4387. DOI: 10.1039/c4tc02837f (cit. on p. 3).

[24] Anton Paar. *DHS 1100 homepage*. May 24, 2019. URL: https://www.anton-paar.com/corp-en/products/details/domed-hot-stage-for-four-circle-goniometers-dhs-1100/ (cit. on p. 8).

[25] Ripan K. Biswas et al. “Study of short range structure of amorphous Silica from PDF using Ag radiation in laboratory XRD system, RAMAN and NEXAFS”. In: *Journal of Non-Crystalline Solids* 488 (May 2018), pp. 1–9. DOI: 10.1016/j.jnoncrysol.2018.02.037 (cit. on p. 11).

[26] P. P. Ewald. “Introduction to the Dynamical Theory of X-Ray Diffraction”. In: *Acta Crystallographica Section A: Crystal Physics, Diffraction, Theoretical and General Crystallography* 25.1 (Jan. 1969), pp. 103–108. DOI: 10.1107/s0567739469000155 (cit. on p. 12).

[27] W. H. Bragg and W. L. Bragg. “The Reflection of X-Rays by Crystals”. In: *Proceedings of the Royal Society A: Mathematical, Physical and Engineering Sciences* 88.605 (July 1913), pp. 428–438. DOI: 10.1098/rspa.1913.0040 (cit. on p. 12).

[28] P. Scherrer. “Bestimmung der Größe und der inneren Struktur von Kolloidteilchen mittels Röntgenstrahlen”. In: *Nachrichten von der Gesellschaft der Wissenschaften zu Göttingen, Mathematisch-Physikalische Klasse* 1918 (1918), pp. 98–100. URL: http://eudml.org/doc/59018 (cit. on p. 13).

[29] Malvern Panalytical. *Panalytical Empyrean website*. URL: https://www.malvernpanalytical.com/en/products/product-range/empyrean-range/empyrean/index.html (cit. on p. 14).

[30] Malvern Panalytical. *PIXcel 3D detector webpage*. URL: https://www.malvernpanalytical.com/en/products/category/x-ray-components/detectors/pixcel3d (cit. on p. 14).

[31] Dectris. *Pilatus 2M webpage*. URL: https://www.dectris.com/products/pilatus3/pilatus3-s-for-synchrotron/details/pilatus3-s-2m (cit. on p. 17).

[32] H. J. Bunge. "Texture Analysis in Materials Science, translated by PR Morris". In: (1982) (cit. on p. 17).

[33] Benedikt Schrode et al. "GIDVis: a comprehensive software tool for geometry-independent grazing-incidence X-ray diffraction data analysis and pole-figure calculations". In: *Journal of Applied Crystallography* 52.3 (May 2019), pp. 683–689. DOI: 10.1107/s1600576719004485 (cit. on pp. 18, 54, 59).

[34] J. Joubert et al. "Etude cristallographique du gallate de lithium et de sa solution solide avec l'aluminate". In: *Comptes Rendus Hebdomadaires des Seances de l'Academie des Sciences* 256 (1963). COD file no. 1007185, pp. 5324–5326 (cit. on pp. 20, 21, 28).

[35] T. F. W. Barth. "The Cristobalite Structures. I. High-Cristobalite". In: *American Journal of Science, Serie 5(1,1921-1938)* 23 (1932). COD file no. 1010921, pp. 350–356 (cit. on pp. 21, 28).

[36] Helen Y. Playford et al. "Structures of Uncharacterised Polymorphs of Gallium Oxide from Total Neutron Diffraction". In: *Chemistry - A European Journal* 19.8 (Jan. 2013). ICSD file no. 236276, pp. 2803–2813. DOI: 10.1002/chem.201203359 (cit. on p. 20).

[37] Detlef-M. Smilgies. "Scherrer grain-size analysis adapted to grazing-incidence scattering with area detectors". In: *Journal of Applied Crystallography* 42.6 (Oct. 2009), pp. 1030–1034. DOI: 10.1107/s0021889809040126 (cit. on p. 30).

[38] E. Chason and T. M. Mayer. "Thin film and surface characterization by specular X-ray reflectivity". In: *Critical Reviews in Solid State and Materials Sciences* 22.1 (Mar. 1997), pp. 1–67. DOI: 10.1080/10408439708241258 (cit. on pp. 36, 40).

[39] Augustin Fresnel. *Oeuvres complètes d'Augustin Fresnel. Tome 1*. Ed. by Imprimerie Imperiale de Paris. Vol. 1. 1866 (cit. on p. 38).

[40] Malvern Panalytical. *AMASS webpage*. Apr. 8, 2019. URL: https://www.malvernpanalytical.com/en/products/category/software/x-ray-diffraction-software/AMASS (cit. on p. 39).

[41] Stephen M. Danauskas et al. "Stochastic fitting of specular X-ray reflectivity data using StochFit". In: *Journal of Applied Crystallography* 41.6 (Nov. 2008), pp. 1187–1193. DOI: 10.1107/s0021889808032445 (cit. on p. 39).

[42] Malvern Panalytical. *X'Pert Reflectivity software manual*. Jan. 30, 2009 (cit. on p. 39).

[43] Miho Yasaka. "X-ray thin-film measurement techniques - X-ray reflectivity measurement". In: *The Rigaku Journal* 26.2 (2010), pp. 1–9. URL: https://www.rigaku.com/downloads/journal/RJ26-2/RJ26-2.pdf (cit. on p. 40).

[44] Glatter Otto and Kratky Otto. *Small Angle X-ray Scattering*. Ed. by Academic Press. 1982 (cit. on p. 51).

[45] Dectris. *Pilatus 1M webpage*. URL: https://www.dectris.com/products/pilatus3/pilatus3-s-for-synchrotron/details/pilatus3-s-1m (cit. on p. 53).

[46] Dectris. *Pilatus 100k webpage*. URL: https://www.dectris.com/products/pilatus3/pilatus3-x-for-synchrotron/details/pilatus3-x-100k-a (cit. on p. 53).

[47] David Babonneau. "FitGISAXS: software package for modelling and analysis of GISAXS data using IGOR Pro". In: *Journal of Applied Crystallography* 43.4 (July 2010), pp. 929–936. DOI: 10.1107/s0021889810020352 (cit. on p. 54).

[48] Rémi Lazzari. "IsGISAXS: a program for grazing-incidence small-angle X-ray scattering analysis of supported islands". In: *Journal of Applied Crystallography* 35.4 (July 2002), pp. 406–421. DOI: 10.1107/s0021889802006088 (cit. on p. 54).

[49] J. Burle et al. *BornAgain - Software for simulating and fitting X-ray and neutron small-angle scattering at grazing incidence*. 2018. URL: http://www.bornagainproject.org (cit. on p. 54).

[50] Y. Yoneda. "Anomalous Surface Reflection of X Rays". In: *Physical Review* 131.5 (Sept. 1963), pp. 2010–2013. DOI: 10.1103/physrev.131.2010 (cit. on p. 56).

[51] KLA Corporation. *Reflectance Calculator*. Oct. 11, 2019. URL: https://www.filmetrics.com/reflectance-calculator (cit. on p. 63).

[52] David Nečas and Petr Klapetek. "Gwyddion: an open-source software for SPM data analysis". In: *Central European Journal of Physics* 10.1 (1 Jan. 2012), pp. 181–188. ISSN: 1895-1082. DOI: 10.2478/s11534-011-0096-2 (cit. on p. 70).

[53] Melvin Avrami. "Kinetics of Phase Change. I General Theory". In: *The Journal of Chemical Physics* 7.12 (Dec. 1939), pp. 1103–1112. DOI: 10.1063/1.1750380 (cit. on p. 72).

[54] Melvin Avrami. "Kinetics of Phase Change. II Transformation-Time Relations for Random Distribution of Nuclei". In: *The Journal of Chemical Physics* 8.2 (Feb. 1940), pp. 212–224. DOI: 10.1063/1.1750631 (cit. on p. 72).

[55] Melvin Avrami. "Granulation, Phase Change, and Microstructure Kinetics of Phase Change. III". In: *The Journal of Chemical Physics* 9.2 (Feb. 1941), pp. 177–184. DOI: 10.1063/1.1750872 (cit. on p. 72).

[56] H. Niedrig. "Physical background of electron backscattering". In: *Scanning* 1.1 (1978), pp. 17–34. DOI: 10.1002/sca.4950010103 (cit. on p. 78).

[57] Hannah N. Masten, Jamie D. Phillips, and Rebecca L. Peterson. "Ternary Alloy Rare-Earth Scandate as Dielectric for β-Ga_2O_3 (MOS) Structures". In: *IEEE Transactions on Electron Devices* 66.6 (June 2019), pp. 2489–2495. DOI: 10.1109/ted.2019.2911237 (cit. on p. 85).

[58] J. Remondina et al. "Responsive charge transport in wide-band-gap oxide films of nanostructured amorphous alkali-gallium-germanosilicate". In: *Journal of Materials Chemistry C* 7.25 (2019), pp. 7768–7778. DOI: 10.1039/c9tc02080b (cit. on p. 85).

[59] Keysight Technologies. *Impedance Measurement Handbook. A guide to measurement technology and techniques*. 6th ed. May 29, 2019. URL: https://literature.cdn.keysight.com/litweb/pdf/5950-3000.pdf (cit. on pp. 86, 88).

[60] Stig Ekelof. "The Genesis of the Wheatstone Bridge". In: *Engineering Science and Education Journal* 10.1 (Feb. 2001), pp. 37–40 (cit. on p. 88).

[61] J. Ross Macdonald and William R. Kenan. *Impedance Spectroscopy: Emphasizing Solid Materials and Systems*. Wiley-Interscience, 1987. ISBN: 9780471831228 (cit. on p. 89).

[62] Andrew K Jonscher. "Dielectric relaxation in solids". In: *Journal of Physics D: Applied Physics* 32.14 (Jan. 1999), R57–R70. DOI: 10.1088/0022-3727/32/14/201 (cit. on pp. 89, 107).

[63] J. B. Varley et al. "Oxygen vacancies and donor impurities in β-Ga_2O_3". In: *Applied Physics Letters* 97.14 (Oct. 2010), p. 142106. DOI: 10.1063/1.3499306 (cit. on p. 101).

[64] Wei Xu et al. "Electrical and optical characterization of individual GaSb nanowires". In: *Quantum Dots, Particles, and Nanoclusters VI*. Ed. by Kurt G. Eyink, Frank Szmulowicz, and Diana L. Huffaker. SPIE, Feb. 2009. DOI: 10.1117/12.816931 (cit. on p. 103).

[65] Oxford instrumens. *MicrostatHe*. Sept. 18, 2019. URL: https://nanoscience.oxinst.com/products/cryostats-for-microroscopy/microstathe (cit. on p. 103).

[66] Ping Sheng. "Fluctuation-induced tunneling conduction in disordered materials". In: *Physical Review B* 21.6 (Mar. 1980), pp. 2180–2195. DOI: 10.1103/physrevb.21.2180 (cit. on p. 104).

[67] M. M. Fogler, S. Teber, and B. I. Shklovskii. "Variable-range hopping in quasi-one-dimensional electron crystals". In: *Physical Review B* 69.3 (Jan. 2004). DOI: 10.1103/physrevb.69.035413 (cit. on p. 105).

[68] Peter Josef William Debye. *Polar molecules*. Chemical Catalog Company, Incorporated, 1929 (cit. on p. 106).

[69] Kenneth S. Cole and Robert H. Cole. "Dispersion and Absorption in Dielectrics I. Alternating Current Characteristics". In: *The Journal of Chemical Physics* 9.4 (Apr. 1941), pp. 341–351. DOI: 10.1063/1.1750906 (cit. on p. 107).

[70] D. W. Davidson and R. H. Cole. “Dielectric Relaxation in Glycerol, Propylene Glycol, andn-Propanol”. In: *The Journal of Chemical Physics* 19.12 (Dec. 1951), pp. 1484–1490. DOI: 10.1063/1.1748105 (cit. on p. 107).

[71] S. Havriliak and S. Negami. “A complex plane representation of dielectric and mechanical relaxation processes in some polymers”. In: *Polymer* 8 (Jan. 1967), pp. 161–210. DOI: 10.1016/0032-3861(67)90021-3 (cit. on p. 107).

[72] A. K. Jonscher. “The ‘universal’ dielectric response”. In: *Nature* 267.5613 (June 1977), pp. 673–679. DOI: 10.1038/267673a0 (cit. on p. 107).

[73] Li Qiang Zhu et al. “Artificial synapse network on inorganic proton conductor for neuromorphic systems”. In: *Nature Communications* 5.1 (Jan. 2014). DOI: 10.1038/ncomms4158 (cit. on p. 113).

[74] Fabien Alibart et al. “A Memristive Nanoparticle/Organic Hybrid Synapstor for Neuroinspired Computing”. In: *Advanced Functional Materials* 22.3 (Dec. 2011), pp. 609–616. DOI: 10.1002/adfm.201101935 (cit. on pp. 113, 117).

[75] Sung Hyun Jo et al. “Nanoscale Memristor Device as Synapse in Neuromorphic Systems”. In: *Nano Letters* 10.4 (Apr. 2010), pp. 1297–1301. DOI: 10.1021/nl904092h (cit. on p. 115).

[76] BioLogic Science Instrument. *EC-Lab*. July 12, 2019. URL: https://www.biologic.net/softwares/ec-lab-software/#1461666531286-9f792007-63fe (cit. on p. 119).

[77] Ametek scientific instrument. *ZSimpWIn*. July 12, 2019. URL: https://www.ameteksi.com/products/software/zsimpwin (visited on 07/12/2019) (cit. on p. 119).

[78] Scribner. *ZView*. July 12, 2019. URL: http://www.scribner.com/software/68-general-electrochemistr376-zview-for-windows/ (cit. on p. 119).

[79] B. A. Boukamp. *Equivalent Circuit (EQUIVCRT. PAS), Users Manual: The Computer Assisted Electrochemical Acimmittance Data Analysis System for IBM-PC Computers and Compatibles, Written in Turbo Pascal Version 3.0*. University of Twente, Department of Chemical Technology, 1989. URL: https://books.google.at/books?id=xLriPgAACAAJ (cit. on p. 119).

[80] James Ross Macdonald. *LEVM(W)*. July 12, 2019. URL: http://jrossmacdonald.com/levmlevmw/ (cit. on p. 119).

[81] Paul Johnson. “Progress in chemometrics research, A. L. Pomerantsev (ed.), Nova Science, New York, 2005, ISBN 1-59454-257-0, vii +325, pp”. In: *Journal of Chemometrics* 19.4 (2005). the program is available online at http://www.abc.chemistry.bsu.by/vi/analyser/, pp. 89–102. DOI: 10.1002/cem.939. eprint: https://onlinelibrary.wiley.com/doi/pdf/10.1002/cem.939. URL: https://onlinelibrary.wiley.com/doi/abs/10.1002/cem.939 (cit. on p. 119).

[82] Harold F. Winters and Eric Kay. “Gas Incorporation into Sputtered Films”. In: *Journal of Applied Physics* 38.10 (Sept. 1967), pp. 3928–3934. DOI: 10.1063/1.1709043 (cit. on p. 123).

[83] Borislav Zdravkov et al. “Pore classification in the characterization of porous materials: A perspective”. In: *Open Chemistry* 5.2 (Jan. 2007). DOI: 10.2478/s11532-007-0017-9 (cit. on p. 124).

[84] Meng Ni et al. “A review and recent developments in photocatalytic water-splitting using TiO2 for hydrogen production”. In: *Renewable and Sustainable Energy Reviews* 11.3 (Apr. 2007), pp. 401–425. DOI: 10.1016/j.rser.2005.01.009 (cit. on p. 124).

[85] Ya-Wei Huan et al. “Recent Advances in β-Ga2O3–Metal Contacts”. In: *Nanoscale Research Letters* 13.1 (Aug. 2018). DOI: 10.1186/s11671-018-2667-2 (cit. on p. 124).

List of Figures

List of Tables

Abbreviations

Abbr.	Description	Pages
AD	**As Deposited** The notation used to label samples used/characterized after they have been deposited, without any other treatment (if not some cleaning procedures)	8, 10, 42, 44, 45, 47–49, 53, 58, 62–64, 66, 70, 71, 73, 85, 98–101, 103, 108, 109, 111, 116, 122
AFM	**Atomic Force Microscope** Surface imaging technique that use atomic-scale forces to map the morphology of such surface at very small scale (even with a precision below of an angstrom).	29, 53, 69, 71, 72, 74–77, 79, 122
COD	**Crystallography Open Database** It's a free database for accessing Crystallographic Information Files (CIFs). It can be access trought the website `http://www.crystallography.net` and support many methods to look for crystal structures, including an numbering (which is often provided, like in this work).	128
DUT	**Device Under Test** During electrical measurement, one can test different different stuff, but usually they are devices with different complexity, ranging from a piece of metal to entire working prototypes. When describing the basics of the experiment performed, usually it's principle can be easily extended to different kind of samples, so, to maintain the genericity of the description, it's often used this acronym to refere to the object being characterized.	97

EC **Equivalent Circuit**
An E.C. is an electrical simplification/modelization of a device/sample characterized using Impedance Spectroscopy. It tell what the sample resemble in terms of simple electrical passive elements and how they should be connected to simulate its behavior (*see also* Impedance Spectroscopy) — 89, 93, 97–100, 102, 104, 107, 118–120

FFT **Fast Fourier Transform**
A Fourier transform is a mathematical operation that can convert a dataset in a given space to a second dataset that keep all the information but is displayed in the reciprocal space. This operation is often used to highlight some periodicity in the given signal (they appear as peaks in the transformed dataset). This kind of data treatment is often used for converting electrical signal recorder in time domain to their frequency space (so to better understand their components). A second quite common use is in solid state physic (and related application) where is it used to convert data between the real and reciprocal (q) space. The adjective "fast" come from the used algorithm for performing such operation that should speed up the calculation performed according to the definition. — 40–46

FWHM **Full Width at Half Maximum**
a quantity to quantify how width a peak is. It's defined starting the maximum intensity of a peak, and then taking it's width where $I=I_{max}/2$, so it can be defined also for peaks whose shape is not well know — 22, 29, 30

GISAXS **Small Angle X-ray Scattering**
SAXS experiment performed at grazing incidence (small incident angle, usually just 1° or less) (*see also* Small Angle X-ray Scattering) — 46, 48, 51, 53

GIXRD **Grazing Incidence XRD**
XRD experiment performed at grazing incidence (small incident angle, usually just 1° or less) and with information collected on a 2D area, so that they form a map of the diffracted intensity (*see also* X-Ray Diffraction) — 16, 18, 26, 28, 29, 33, 34, 54

HN **Havriliak-Negami model**
An extension of the Debye model for dipole relaxation mechanism. In particular it account for both symmetric and asymetric broadening using two new parameters (either called n and m or alpha and beta). It was developed in 1967 by S. Havriliak and S. Negami — 111, 119

ICSD **Inorganic Crystal Structure Database**
It's a crystallographic database focused on inorganic structures. It's maintained thanks to FIZ Karlsruhe - Leibniz Institute for Information Infrastructure. It can be accessed at `http://www2.fiz-karlsruhe.de/icsd_home.html`. — 128

IS **Impedance Spectroscopy**
A characterization technique in which a sample/device is probed using an alternate electrical field signal (either a current or a voltage) and its response (the other quantity) is measured, so to obtain an impedance (complex value). This operation is performed for many frequencies (depending on the available instruments/techniques they can vary from mHz to GHz or even THz; in this work I'm speaking of the range between tens or hundreds of Hz and 1MHz) and obtain a spectrum. — 88, 93, 100, 106, 108, 116, 118, 119

NC **NanoCrystal**
With the term of nanocrystal we refer to a single crystal domain we can observe. Based on our characterization, we believe that in each nanoparticle we can have more then one nanocrystal. (*see also* NanoParticle) — 28, 59, 122

NP **NanoParticle**
For nanoparticle we mean a region inside our samples that we can see using various techniques, so it cannot be better defined (i.e. it can differ from the surrounding for its composition in SEM, but when looked at using the AFM it must have a different height, and the two regions canbe different). (*see also* NanoCrystal) — 3, 26, 27, 30, 58, 59, 70–73, 76, 83, 84, 101, 117, 122, 123

RoI **Region of Interest**
When working on map/image data, often you are not interested in the whole image as a single element, but maybe you want highlight/measure/-count some portion of it. This parts of the image are called Regions of Interest. 54, 55

SAXS **Small Angle X-ray Scattering**
In scattering measurements (both using visible wavelengths or X-Ray), the average size and shape of different regions inside a material can be measured looking at the decay rate of the signal moving farther away from the direct beam spot. The "Small Angle" name comes to the fact that the most important informations lay very near the direct beam spot, usually around 1°. 44, 50, 51, 53, 54, 56–59, 122

SDD **Sample-Detector Distance**
For measurements when the detector is 2D, such as during GI, it's required to transform the acquired immagine in real space to something that is set-up independent, and this is the most important parameter to play with (*see also* Grazing Incidence XRD & Small Angle X-ray Scattering) 17, 53

SEM **Scanning Electron Microscope**
A microscope that work using a focused beam of electron accelerated by an electrical field in the range of kV to tens of kV on a tiny spot on the sample. The most common read data are the Secondary Electrons (S.E.) or the Back Scattered ones (B.S.E.) giving information about respectively the surface morphology and the electron density of the atoms at the surface (although the two contributions can't never be completely separated). Other detectors can be installed to measure, for example, the chemical composition (Energy Dispersive X-ray Analysis, EDX), the electrical conductivity (Electron Beam Induced Current), or the photon emission (Cathodoluminescence) of the sample. Since this technique rely on a focused beam to work, a system to move such beam (and so to "scan" the sample with it) is also implemented." 76, 80–82

STDP **Spike-Timing Dependent Plasticity**
This mechanism is the respinsible forbiological thinking. It's consist in a change of the stat of the synapse (both biological or artificial) due to tramission of a spike signal that arrive from a pre-synaptic neuron and will be transmitted to the post-synaptic one. The key feature of this kind of memory is that it encode the information also in the order and the delay between the two spikes. 113, 116–118, 123

TT **either Thermal Treated or Thermal Treatment**
The notation used to label samples that underwent annealing (usually at 700°C for 30 minutes) or the annealing process itself 3, 8–10, 18–20, 23, 25, 26, 28, 29, 31–36, 40, 42–45, 47–49, 53, 54, 58, 59, 61–63, 66, 70, 71, 74, 75, 77, 79, 80, 82, 83, 85, 98, 122

XPS **X-ray Photoelectron Spectroscopy**
X-ray Photoelectron Spectroscopy is a characterization technique used to detect which elements and in which quantity are present in a given sample. The main advantages over other more common techniques (i.e. ED-XRF) is its ability to also differentiate the oxidation states of the atoms. Thanks to this possibility, this technique (and similar ones) are also known as ESCA - Electron Spectroscopy for Chemical Analysis. 66, 67, 81

XRD **X-Ray Diffraction**
A characterization technique widely used to know the crystal structure of a sample thanks to the ability of the crystal planes to diffract x-ray only at specific directions defined by their distances 2, 11, 13–16, 19, 26, 32, 33, 37, 43, 53, 72, 122

XRR **X-Ray Reflectivity**
Surface technique used to investigate thin films using reflected x-rays. it can give informations about the electronic density, thickness and roughtness of various surface layers. It's best used for layers with thickness between few nm up to hundreds of nm — 14, 15, 24, 35, 39, 43–50, 59, 122

Standard definitions

in-plane direction:

The family of the directions co-planar to a film.

out-of-plane direction:

The direction perpendicular to a film surface.

Typical (TT) sample description:

The "standard" sample has been growth on bare silicon cleaned in HF (so to remove the surface oxide layer) for 60 m at a sputtering pressure of 6E-3 mbar made mainly by Argon using an RF power of 250W. The eventual thermal treatment has been performed in air, at 700°C for 30 minutes by inserting and removing the sample to and from the furnace at nominal temperature. Any change in the procedure are listed.

Acknowledgements

The data presented in this thesis were fully analysed and in the majority part collected by myself, however, all of this would not have been possible without the help (both physical, theoretical and some times also to the moral) of many people. In particular I would like to thanks my three supervisors: Prof. Paleari and Dr. Lorenzi from University of Milano - Bicocca and Prof. Ressel from Technische Universität Graz for the theoretical discussion we had that were fundamental to correctly interpret and label all the effects observed.
On the opposite side there are the colleagues from the offices: Michele Caccia, Francesca Cova, Roberta Crapanzano, Gianfranco Fraccaro, Andrea Maurizio Monti, Stefano Paleari and Irene Villa (from unimib) and Benedikt Schrode (who merit a special thanks for his patience with me and my strange x-ray data), Andreas Hofer, Sebastian Hofer, Clemens Tschernay, Johanna Unterkofler and Wolfgang Bodlos (from TUG) that were always ready to explain me how to operate the instruments and to lend me an hand when two or more people were needed to do so.
One of the most fundamental institution when doing science are the collaborations with different laboratories and professors, since (with few exceptions), nobody has the facilities to do everything. During these three years, I was involved in many of these collaborations, starting with Prof. Acciarri from unimib for what concern the deposition, to Prof. Sassella and Dr. Trabattoni (both from unimib too) for the AFM images, from Prof. Koller (from Karl-Franzens Universität in Graz) for his precious XPS investigations to the Elettra - Sincrotrone Trieste personnel, especially Dr. Luisa Barba from XRD1 and Heinz Wilfried Amenitsch from the SAXS beamlines for all the grazing incidence data they help me to collect and treat.
And finally, I would like to thanks all the other people, too many, that in some way, maybe minimal with just a word or a suggestion, contributed to this work.